T2R2 東京科学大学 リサーチリポジトリ
Science Tokyo Research Repository

論文 / 著書情報
Article / Book Information

題目(和文)	境界層～上部対流圏／下部成層圏における二酸化窒素とアセトニトリルの衛星観測
Title(English)	Satellite observation of nitrogen dioxide and acetonitrile from boundary layer to upper troposphere and lower stratosphere
著者(和文)	藤縄環
Author(English)	Tamaki Fujinawa
出典(和文)	学位:博士(理学), 学位授与機関:東京工業大学, 報告番号:甲第11219号, 授与年月日:2019年6月30日, 学位の種別:課程博士, 審査員:吉田 尚弘,本倉 健,山田 桂太,神田 学,豊田 栄,笠井 康子
Citation(English)	Degree:Doctor (Science), Conferring organization: Tokyo Institute of Technology, Report number:甲第11219号, Conferred date:2019/6/30, Degree Type:Course doctor, Examiner:,,,,,
学位種別(和文)	博士論文
Type(English)	Doctoral Thesis

Powered by T2R2 (Science Tokyo Research Repository)

TOKYO INSTITUTE OF TECHNOLOGY

DOCTORAL THESIS

Satellite observation of nitrogen dioxide and acetonitrile from boundary layer to upper troposphere and lower stratosphere

A thesis submitted in fulfillment of the requirements
for the degree of Doctor of science

in the

Yoshida laboratory
Department of Emvironmental Chemistry and Engineering

Tamaki FUJINAWA

May 24, 2019

Abstract

Tamaki FUJINAWA

Satellite observation of nitrogen dioxide and acetonitrile from boundary layer to upper troposphere and lower stratosphere

This thesis consists of following parts; (1) an overview of an air pollution problem in the whole world, (2) a feasibility study for the tropospheric NO_2 satellite observations with 1-km order spatial resolution, (3) validation analysis of stratospheric CH_3CN satellite observation of SMILES, and (4) conclusions and future perspectives.

Based on a comprehensive analysis considering realistic atmospheric scenarios, a combination of a fit window of 425–497 nm and a satellite altitude of 300 km is likely to be the optimal combination for the satellite instrument considered in this study. The error estimation analysis considering the error propagation, including the AMF uncertainty, implied that the overall error for the tropospheric NO_2 retrieval was expected to be 0.88×10^{15} molec cm^{-2}, which is consistent with the scientific requirements (5% for the tropospheric NO_2 column).

The systematic error and the relative difference to MLS were 3.78–5.09% and 24.7–35.5% in the altitude range between 8.6 and 4.8 hPa (32–36km). Therefore, SMILES CH_3CN profile had the reliability in the altitude range between 8.6 and 4.8 hPa (32–36km). Above 36 km, SMILES CH_3CN precision was good value but relative difference to MLS is over 100%. From a comprehensive analysis using GFED v4 data, I qualitatively linked the CH_3CN observation with the biomass burning strength.

I concluded necessity of an advanced super low satellite altitude to switch to $\sim$1 km horizontal resolution for future satellite observation and validity of SMILES CH_3CN as a tracer of biomass burning.

Acknowledgements

The JEM/SMILES mission is a joint project of the Japan Aerospace Exploration Agency (JAXA) and th e National Institute of Information and Communications Technology (NICT). The SMILES L2r data are available to users from the website via http://smiles.nict.go.jp/pub/data/index.html.

I am deeply grateful to Prof. Dr. Naohiro Yoshida and Dr. Yasuko Kasai for supervising and encouraging me. I would like to thank Dr. Kazuyuki Miyazaki for providing results of the CHASER model simulation and Dr. Akihiko Kuze of JAXA for providing the plausible instrumental parameters and discussing SNR calculation.

I am grateful to Dr. Vladimir and Dr. Alexei Rozanov of IUP/University of Bremen for providing access to the SCIATRAN model and Dr. Andreas C. Meier, Dr. Andreas Richter and Prof. Dr. John P. Burrows of IUP/University of Bremen for providing the nlin to perform DOAS analysis and for giving me a lot of valuable comments and suggestions about my study. And I spent really good time in IUP/University of Bremen and had good experiences during my short stay thanks to all DOAS group members in IUP/University of Bremen including persons mentioned above. Also, I am really grateful to Prof. Dr. Katsuyuki Noguchi, Dr. Takayoshi Yamada, Dr. Tomohiro Sato and Dr. Takeshi Kuroda for encouraging me and providing valuable comments and suggestions.

I also would like to thank all of the members of Yoshida group and NICT, especially Mr. Yuki Uchiyama, Mr. Atsushi Hirakawa, Mr. Hironori Seki, Mr. Seidai Nara and also undergraduate/graduated colleagues.

Finally, I would like to appreciate my parents and all friends for supporting and encouraging me.

Contents

1 General introduction

Atmospheric chemistry from the planetary boundary layer (PBL) to upper troposphere is of importance with regard to life, climate change, atmospheric transport, and air quality. In the PBL, some trace gas species have key roles for human health, vegetation, and crops. From the upper part of troposphere to tropopause where is a boundary between troposphere and stratosphere, or the free troposphere, meteorological phenomena such as transport and convection are occurring. On the other hand, the stratosphere, where is well-known as the ozone layer, is stratified in temperature and less vertical transport. The stratosphere-troposphere exchange (STE) occurs at the tropopause varying its altitude with latitude and season, which is significant for the radiative balance and atmospheric composition. The study of the STE provides new understanding of atmospheric science such as atmospheric composition, chemical distribution, and dynamical processes of gas species in the upper troposphere and lower stratosphere (UTLS). Figure 1.1 shows that the relationships associated with convectional dynamical processes in the tropopause; the breaking of Rossby waves; the growth and decay of synoptic-scale waves; tropopause folds; warm conveyor belts; the initiation and breaking of gravity waves, and deep convection. These meteorological phenomena significantly affect the chemical transport and therefore transport at the UTLS is an important link in chemistry-climate interactions. For example, the chemical gradients across the tropopause, especially those of water vapor and ozone, are important components of Earth's radiative balance (e.g., Forster and Shine, 1997; Shepherd, 2007).

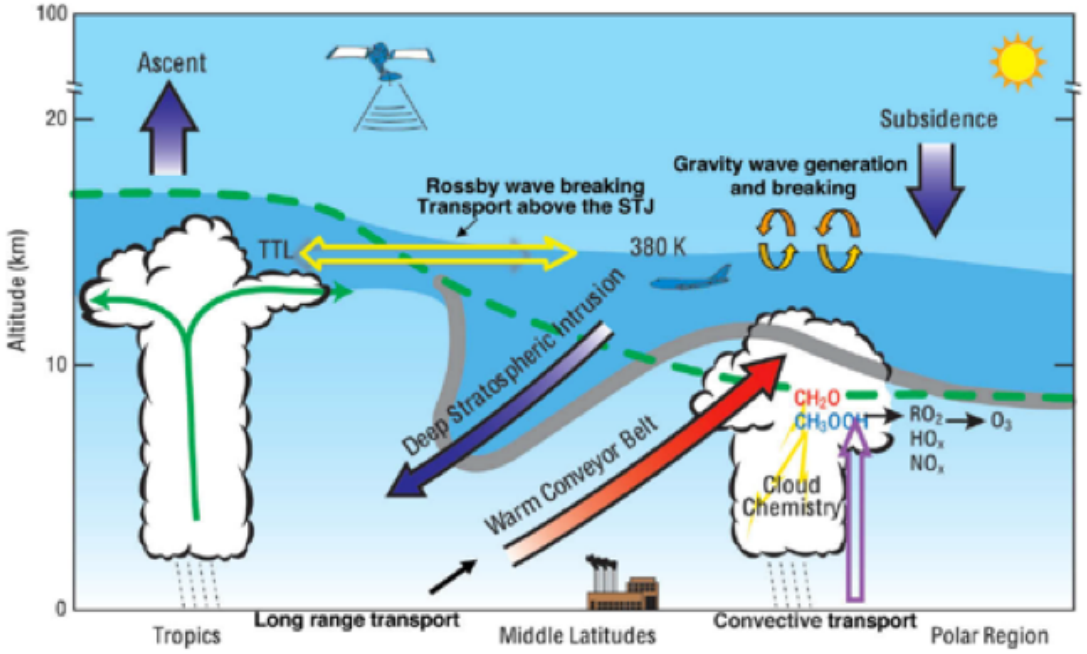

FIGURE 1.1: An illustration of processes of dynamics, chemistry, and cloud microphysics in the UTLS region. Source: Fig. 1 in Pan et al. (2010) which is based on a concept described in Stohl et al. (2003).

1.1 Global air quality

Global air quality is a societal concern in the whole world. According to the World Health Organization's (WHO) report in 2018, ambient (outdoor) air pollution is estimated to have caused 4.2 million premature deaths worldwide per year in 2016, in both cities and rural areas, especially in South-East Asia and the Western Pacific region (World Health Organization, 2016). Subsequently, International Council on Clean Transportation (ICCT) reported in 2019 that the global transportation sector is a major source of this health burden through its contribution to elevated fine particulate matter (PM2.5), ozone (O_3), and nitrogen dioxide (NO_2) concentrations, resulting in stroke, ischemic heart disease, chronic obstructive pulmonary disease, and lung cancer. Figure 1.2 shows the number of transportation-attributable PM2.5 and ozone deaths in 2015 in urbanized area all over the world and the transportation-attributable fraction (TAF). This was epidemiologically estimated using bottom-up emission inventories. The TAF is relatively higher in the developed countries such as Europe, United states of America, and Japan (red color area in Figure 1.2) while in developing counties such as Southeast Asia and India they have low fractions except a part of Indonesia (dark blue and green color area in Figure 1.2). This fact indicates that premature deaths in such developing countries are mainly due to inefficient manner of combustion of agricultural waste and cook-fire as indoor pollution and also biomass burning as ambient pollution although in developed countries it is due to transport. This figure also shows that most of premature deaths occur in East and South-east Asia (size of circle).

FIGURE 1.2: Total number of transportation-attributable PM2.5 and ozone deaths in 2015. A symbol size indicates total number of transportation-attributable PM2.5 and ozone deaths. A color indicates transportation-attributable fraction of total PM2.5 and ozone deaths. Source: Fig. 14 in ICCT report (2019).

Moreover, air pollutants affect not only human health but also atmospheric composition and radiative forcing (Dentener et al., 2005; Unger et al., 2008; Fry et al., 2014). Such pollutants are referred to as SLCPs (Short-Lived Climate Pollutants) including tropospheric ozone (O_3), black carbon, methane, and hydrofluorocarbons. WHO also reported policy-relevant summary

of potential benefits to health from reducing emissions of SLCPs, in which they said that exposure to ozone is responsible for roughly 150 thousand deaths annually from respiratory conditions. The tropospheric O_3 is a major air pollutant and greenhouse gas produced/destructed by some significant photochemical reactions including Non-Methane Volatile Organic Compounds (NMVOC), NO_x (=NO+NO_2) and HO_x (=OH+HO_2) cycle (See section 1.2 in detail). These precursors also play a key role in the tropospheric photochemistry associating with not only O_3 production/destruction but also production of aerosols and environmental burden such as eutrophication and acid rain. Furthermore, PAN (peroxyacetyl nitrate; RO_2NO_2), which is formed via the reaction of NO_2 with peroxyacetyl radicals (RO_2), can be transported to the site from distant pollution sources due to its relatively long lifetime (50 h at 273 K) (Phillips et al., 2013) and re-release NO_2 far from their source regions resulting in nitrogen deposition in rural area and the transboundary pollution.

Nitrogen dioxide (NO_2) is emitted from various sources such as combustion processes of biomass and fossil fuels, microbial activity and lightning. In the PBL, NO_2 emission from combustion of fossil fuel, which is anthropogenic and emitted from power plant and vehicle exhaust, is the dominant source followed by natural sources of biomass burning and biogenic soil emission while in the free troposphere contribution from lightning to NO_2 form is dominant followed by stratospheric injection and aircraft exhaust. van der A. et al. (2008) investigated dominant NO_2 sources all over the world using satellite data by introducing a month of maximum NO_2. Fiugre 1.3 shows the distribution of the dominant NO_2 source. A large part of India and Southeast Asia is undefined because several sources of NO_2 (biomass burning and vehicle exhaust) are existing while meteorological conditions (notably the Asian monsoon) play an important role in the removal of NO_2. Identification of NO_2 sources in such undefined areas even including defined areas where have components of several sources, such as East Japan and East China with anthropogenic emission and biomass burning, is important to assess the effects of NO_2 on human health because these regions have large amount of premature deaths as mentioned above. A chemical transport model is a good tool to estimate the current and future NO_2 conditions. However, bottom-up emission inventories as input data into the model have large uncertainties (-13%–37%) (Zhao et al., 2011). Therefore, a top-down observation for example using satellite instrument is required in combination with in-situ measurement to constrain emission inventories.

NO_2 is a useful tracer for air pollution from anthropogenic emission. On the other hand, acetonitrile (CH_3CN), which is one of NMVOCs, is also a good tracer for the natural source, i.e., biomass burning, and not emitted from anthoropogenic sources. Therefore comprehensive observation and analysis including NO_x and acetonitrile is important to identify NO_2 sources, to estimate the amounts of NO_2 emission, and to understand the interaction between natural and antropogenic emissions of pollutants. The interactive reactions associated with tropospheric ozone and NO_x cycle including acetonitrile (as VOC) are shown in Figure 1.4.

1.2 Key reactions associated with air pollutants

As mentioned above, NO_x and HO_x cycles including the VOC have a important role in production and destruction process of tropospheric ozone.

Tropospheric ozone is photolyzed as following reactions,

$$O_3 + h\nu \rightarrow O_2 + O(^3P), \tag{R1}$$

$$O_3 + h\nu \rightarrow O_2 + O(^1D), \tag{R2}$$

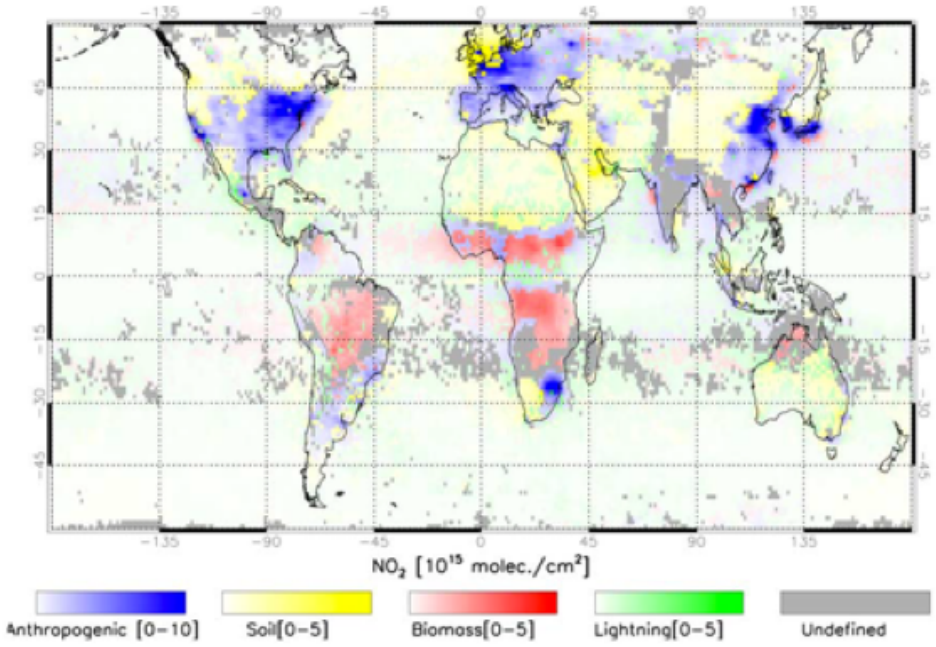

FIGURE 1.3: Dominant NO_2 source identification based on anayses of the time series of measured tropospheric NO_2 at 10:00 am. Source: Figure 7 in van der A. et al. (2008).

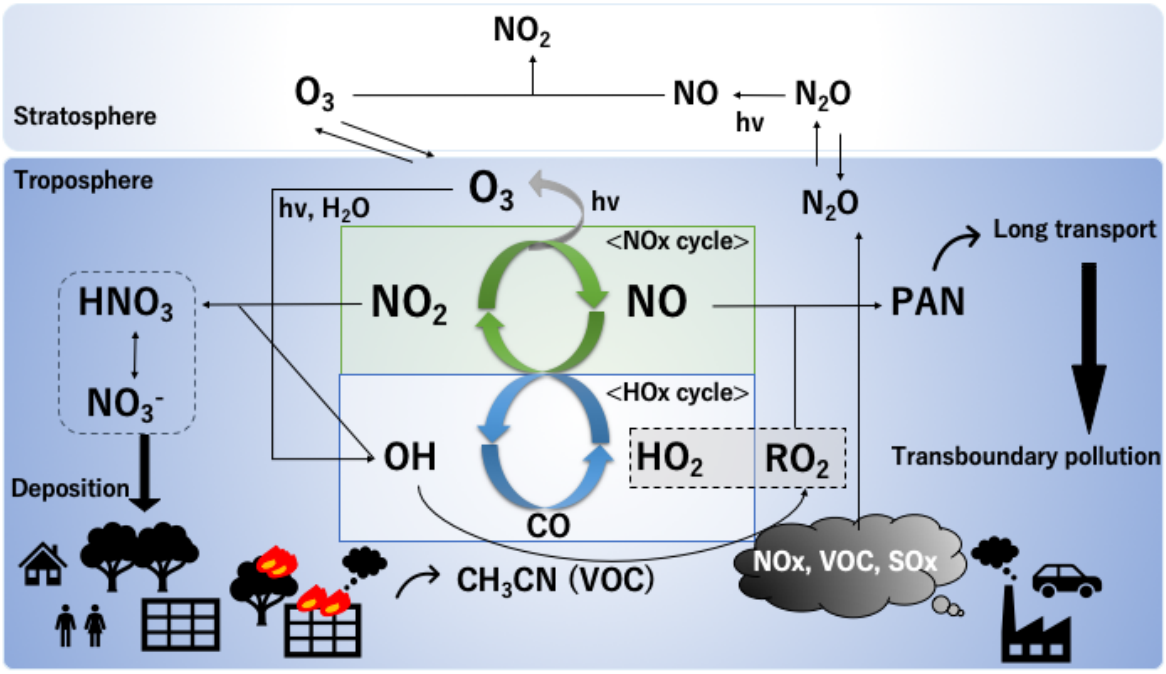

FIGURE 1.4: An illustration of NO_x/HO_x cycle including VOC in troposphere and lower stratosphere.

in the Chappuis band (visible–NIR region; 650–1100 nm) and the Hartley-Huggins band (UV region; 200–340 nm), for example during summertime in mid-latitude by day, with the photolysis rates of about 3×10^{-4} and 1.5×10^{-5} s^{-1} corresponding to the lifetime of around 1 hour and 18 hours, respectively. On the other hand, generated $O(^3P)$ reproduce ozone to recombine with atmospheric O_2 by a three body reaction as,

$$O(^3P) + O_2 + M \rightarrow O_3 + M. \tag{R3}$$

Then, ozone is also destructed by the following reactions,

$$O(^1D) + H_2O \rightarrow 2OH, \tag{R4}$$

$$O_3 + OH \rightarrow HO_2 + O_2, \tag{R5}$$

$$O_3 + HO_2 \rightarrow OH + 2O_2, \tag{R6}$$

$$2O_3 \rightarrow 3O_2 \quad (net). \tag{R7}$$

On the other hand, the tropospheric photochemistry sometimes works on the ozone formation because OH derived from R4 reacts with CO, CH_4, and NMHC in a chain reaction under an existence of NO_x,

$$CO + OH \rightarrow CO_2 + H. \tag{R8}$$

$$H + O_2 + M \rightarrow HO_2 + M, \tag{R9}$$

$$HO_2 + NO \rightarrow OH + NO_2, \tag{R10}$$

$$NO_2 + h\nu \rightarrow NO + O(^3P), \tag{R11}$$

$$O(^3P) + O_2 + M \rightarrow O_3 + M, \tag{R3}$$

$$CO + 2O_2 + h\nu \rightarrow CO_2 + O_3 \quad (net). \tag{R12}$$

Furthermore, reactions of NMHC with OH as below is well-known as the 'photochemical smog reaction',

$$NMVOC + OH + O_2 \rightarrow RO_2, \tag{R13}$$

$$RO_2 + NO + O_2 \rightarrow NO_2 + HO_2 + CARB, \tag{R14}$$

$$HO_2 + NO \rightarrow OH + NO_2, \tag{R15}$$

$$2(NO_2 + h\nu + O_2 \rightarrow NO + O_3), \tag{R16}$$

$$\mathrm{NMVOC} + 4\mathrm{O_2} + h\nu \rightarrow \mathrm{CARB} + 2\mathrm{O_3} \quad (net), \tag{R17}$$

where CARB indicates carbonyl compounds. In a polluted region where NO concentration is high, one molecule of VOC can produce 2 molecules of ozone as above.

Equations above show that NO_x and VOC is mainly associated with the production of the tropospheric ozone while HO_x is associated with the destruction of tropospheric ozone. Especially in a polluted case, concentration and distribution of NO_x are significant for the determination of HO_x concentration and production (destruction) rate of ozone.

In the stratosphere, ozone is formed as below which is so-called the Chapman cycle (Chapman, 1930),

$$\mathrm{O_2} + h\nu \rightarrow \mathrm{O} + \mathrm{O}, \tag{R18}$$

$$\mathrm{O} + \mathrm{O_2} + \mathrm{M} \rightarrow \mathrm{O_3} + \mathrm{M}, \tag{R19}$$

$$\mathrm{O} + \mathrm{O_3} \rightarrow \mathrm{O_2} + \mathrm{O_2}, \tag{R20}$$

$$\mathrm{O_3} + h\nu \rightarrow \mathrm{O_2} + \mathrm{O}, \tag{R21}$$

The stratospheric ozone is well-known as the ozone layer protecting life on Earth from hazardous ultraviolet (UV) radiation from the sun.

1.3 Satellite observation of air quality

Satellite instruments are good tool for global air quality monitoring from space and observe atmospheric trace gases using a remote sensing technique in specified frequency bands. To improve air quality, it is important to know what contributes to polluting the air. Satellite images help identify large areas of pollution caused by fires, dust or sand storms, volcanic eruptions, large industrial sources, or the transport of man-made pollution from other regions. Global observations of air pollutants having spectral features in UV/visible region (e.g., NO_2 and O_3) from space, employing instruments such as the Global Ozone Monitoring Experiment (GOME; (Burrows et al., 1999)), the Scanning Imaging Absorption Spectrometer for Atmospheric Cartography (SCIAMACHY; (Bovensmann et al., 1999)), the Ozone Monitoring Instrument (OMI; (Levelt et al., 2006)), and GOME-2 (Callies et al., 2000), all operating on low earth orbit (LEO) satellites orbiting at an altitude of around 800 km, have provided us with a better understanding of the emissions, spatiotemporal distributions, and long term trends since the mid-1990s, on the basis of the differential optical absorption spectroscopy (DOAS) technique (Richter and Burrows, 2002; Beirle et al., 2003; Richter et al., 2005; Kim et al., 2006; van der A et al., 2006; van der A. et al., 2008; Stavrakou et al., 2008; Boersma et al., 2011; Lamsal et al., 2011; Hilboll et al., 2013; Duncan et al., 2016).

1.4 Purpose of this thesis

The final goal of this study is to identify NO_2 emission sources in the region where several sources are mixed, and to detect the NO_2 hotspot. In this thesis, I provide a concept of future satellite air quality observation of NO_2 with high spatial resolution and validate the availability of CH_3CN as an indicator for biomass burning focusing on the satellite observations. This thesis has two purposes as follows;

- to investigate a feasibility of advance concept for air quality observation of the tropospheric NO_2 using satellite instrument with a high spatial resolution of 1×1 km^2,
- to perform an error analysis for Superconducting Submillimeter-Wave Limb-Emission Sounder (SMILES) observation and validation analysis comparing with Aura/MLS (Microwave Limb Sounder) observation, and to discuss a traceability of CH_3CN for biomass burning comparing with GFED (Global Fire Emissions Database) version 4.

Chapter 2 gives the concept of satellite observation of NO_2 with 1×1 km^2 horizontal resolution. In the chapter 3, the validation analysis of SMILES CH_3CN observation are given. Chapter 4 summarizes and concludes this thesis.

2 Feasibility study for km spatial resolved NO_2 observations

2.1 Introduction

Nitrogen dioxide (NO_2) is one of the most important trace gases in the troposphere, participating in catalytic cycles that result in the production of ozone (O_3), and its oxidation to nitric acid, HNO_3, results in the acidification of aerosols. As is well known, the anthropogenic production of NO_x (the sum of NO and NO_2) from fossil fuel combustion leads to smog and poor air quality episodes. This in turn affects human health, especially through the entry of aerosol particles of extremely small diameter (less than 2.5 microns) and O_3 into the cardiovascular system. NO_2 itself is also toxic. The main sources of NO_2 are anthropogenic, especially fossil fuel combustion (e.g., power plants and vehicles) at urbanized sites. Since the Industrial Revolution, fossil fuel combustion has emerged as the major source of NO and NO_2 owing to the rapid increase in its use as a source of energy for domestic heating, power generation, industry, and transport. Over polluted regions, 50%–90% of the NO_2 exists in the troposphere depending on the degree of pollution, where it has a typical photochemical lifetime of several hours (Beirle et al., 2011).

Recently, the Sentinel-5 Precursor (TROPOMI; TROPOspheric Monitoring Instrument), which was launched in October 2017 at an orbit of 824 km, began to observe atmospheric trace gases including NO_2 with a high spatial resolution of 3.5×7 km^2 (Ingmann et al., 2012). As existing LEO instruments mentioned in Section 1.3 prioritize observations with global coverage rather than diurnal variations of atmospheric gas species, they use sun-synchronous orbits that pass the measurement location at a fixed local time. Satellite instruments in geostationary earth orbit (GEO), which are at an altitude of around 36000 km, enable us to conduct optimal temporal sampling of a specific region and obtain information on the diurnal variations. In addition to such LEO satellite missions, advanced air quality monitoring missions using a GEO satellite constellation, namely GEO-AQ, are being developed for launch in the 2018–2026 time frame, as are complementary LEO satellite missions, including Sentinel-5 (S5) on the MetOp-SG series, which is the successor to GOME-2 and has a better match with the spectral observations of SCIAMACHY, Ozone Mapping Profiler Suite (OMPS) (Flynn et al., 2004) on the Suomi National Polar orbiting Partnership (Suomi-NPP) and Joint Polar Satellite System (JPSS), and Environment Monitoring Instrument (EMI) on the GaoFen-5 satellite. The GEO-AQ constellation comprises the Geostationary Environment Monitoring Spectrometer (GEMS, Korea) (Kim, 2012), Sentinel-4 (ESA) (Ingmann et al., 2012), and Tropospheric Emissions: Monitoring of Pollution (TEMPO, NASA) (Zoogman et al., 2017). The nominal spatial resolution for observations is 2–8 km at the middle latitudes, which is extremely high compared to existing LEO satellites, e.g., 13×24 km^2 for OMI nadir. The GEO-AQ and potential LEO satellite missions (e.g., Spectrolite (de Goeij et al., 2017) for NO_2), together with ship- or ground-based observations (Wang et al., 2017; Hong et al., 2018) and aircraft measurements (Meier et al., 2017), are expected to facilitate synergistic analyses for the study of air pollution. Although the spatial resolution of the GEO-AQ and TROPOMI instruments is very high, it remains inadequate for maximizing the number of cloud-free observations and effectively separating large point sources that are clustered together in urban regions. To obtain the best information about local sources, an observation with a kilometer-order horizontal resolution, e.g., 1×1 km^2, is required. A spatial resolution of 1×1 km^2 enables us to detect local emission plumes of NO_2, although there is a trade-off

between spatial resolution and observation frequency. Switching to a spatial resolution of 1 km coupled with global and adequate diurnal sampling by a future constellation would address issues such as understanding the turbulent mixing of emissions into the air mass and its effects on transport and transformation, as well as the short-term evolution of pollution plumes.

I investigated the observation capability and proposed the optimal setup for the observational wavelength domain (425–450 nm, 405–465 nm and 425–497 nm), altitude of the satellite (300 km and 600 km), and sensor specifications by performing simulations for NO_2 measurements under the assumption of a LEO satellite. In this study, the instrument is supposed to be aboard on a small satellite and to specialize for NO_2 observation with a narrow observational wavelength domain from 400–500 nm. In case of Spectrolite, which is a nano satellite mission developed in Netherlands, the observational wavelength domain and instrumental size are set to be 320–500 nm and $10 \times 20 \times 20$ cm^3 (mass < 25 kg). The instrumental concept discussed in the present study is inherited from the SCIAMACHY project and studies for potential Japanese air quality monitoring missions, such as Air POLLution Observation (APOLLO), Geostationary mission for Meteorology and Air pollution (GMAP-Asia) (Akimoto et al., 2009; Kasai et al., 2011), the SCIA-ISS concept, and the uvSCOPE mission, which have been candidates for the Earth observation section of the International Space Station (ISS). In the uvSCOPE technical document (private communication with Dr. Y. Kanaya of JAMSTEC), two observational wavelength domains were considered, i.e., (a) 320–450 nm which observes with a relatively-wide range in UV/vis, and (b) 460–490 nm which specializes for NO_2 observation, respectively. The size of these instruments were expected to be $80 \times 45 \times 39$ cm^3 for instrument (a) and $56 \times 35 \times 35$ cm^3 for instrument (b), indicating that an extension of wavelength domain from 30 nm to 130 nm is expected to results in increasing the instrumental size (i.e. instrumental mass) in a factor of 2. Thus, based on the Spectrolite's specification, the instrumental size and mass considered in this study could be optimized in the further steps although it is out of focus in this thesis. Our objectives for the instrument considered in this thesis are as follows: (i) to observe the entire globe with a high spatial resolution of 1×1 km^2; and (ii) to specialize in NO_2 observations using an optimal fit window for NO_2 retrieval. To test the feasibility of such an instrument, I estimated the signal-to-noise ratios (SNRs) of the proposed sensor and the measurement errors of the tropospheric NO_2 slant column densities (SCDs) with a horizontal resolution of 1×1 km^2.

The remainder of this chapter is organized as follows. Section 2.2 describes the setup used in the sensitivity study, i.e., the setup for the radiative transfer calculation, the setup for the given sensor specification and derivation of the SNR of the sensor, and the setup for the error analysis method. Section 2.3 discusses the observation capability on the basis of comparison results of measurement errors of the retrieved NO_2 SCDs for each geometry and the relationships between the SNRs and the measurement errors. The final section summarizes our findings and concludes this chapter.

2.2 Setup for the sensitivity study

To determine the optimal space-based resolution for the estimation of NO_x emissions using the total tropospheric NO_2 column amount from urban sources, I adopt a pragmatic approach. This is because the size of NO_2 plumes depends on several factors, namely the size and distribution of urban sources, the wind speed and direction, the processes that mix the air from the source into the wind flow, which are in part turbulent, etc. Consequently, to determine the optimal spatial resolution, I used NO_2 observations from aircraft remote sensing measurements obtained by the University of Bremen instrument, namely AirMAP (Schönhardt et al., 2015; Meier et al., 2017). AirMAP was flown on an FU-Berlin Cessna aircraft with an altitude of

3.1 km in a variety of campaigns to investigate NO_2 plumes from urban sources, power plants, and shipping (Meier et al., 2017; Seyler et al., 2018; Merlaud et al., 2018).

As an example, Figure 2.1 shows the NO_2 VCD below the aircraft, measured by AirMAP in the morning ($\sim$ 07:30–09:30 UTC) of April 21, 2016, i.e., a weekday (Thursday), above the city of Berlin. The city borders and major roads are shown by pink and black lines, respectively. Flights were performed within the AROMAPEX campaign with the objective of comparing airborne imaging DOAS instruments (Tack et al., 2018). Details of the instrument and the analysis of the data shown here can be found in Meier et al. (2017). The wind conditions on this day were close to a good approximation constant during the 2 hours required to obtain the aircraft measurements.

Figure 2.1 shows the tropospheric NO_2 VCD data averaged to (a) 0.1 km $\times$ 0.1 km, (b) 0.5 km $\times$ 0.5 km, (c) 1 km $\times$ 1 km, and (d) the nominal S5P resolution of 3.5 km $\times$ 7 km. As can be seen, the two large but different urban plumes are readily discerned in panels (a)–(c) but not in panel (d). I note that winds are generally relatively strong at the middle latitudes compared to the sub-tropical and tropical latitudes. Even the much improved spatial resolution of the highest currently available space-based remote sensing data will thus not be able to separate patterns such as those observed in Berlin. Therefore, I pragmatically conclude that a spatial resolution of $\sim$ 1 km $\times$ $\sim$ 1 km is required to effectively identify and separate such urban emissions sources.

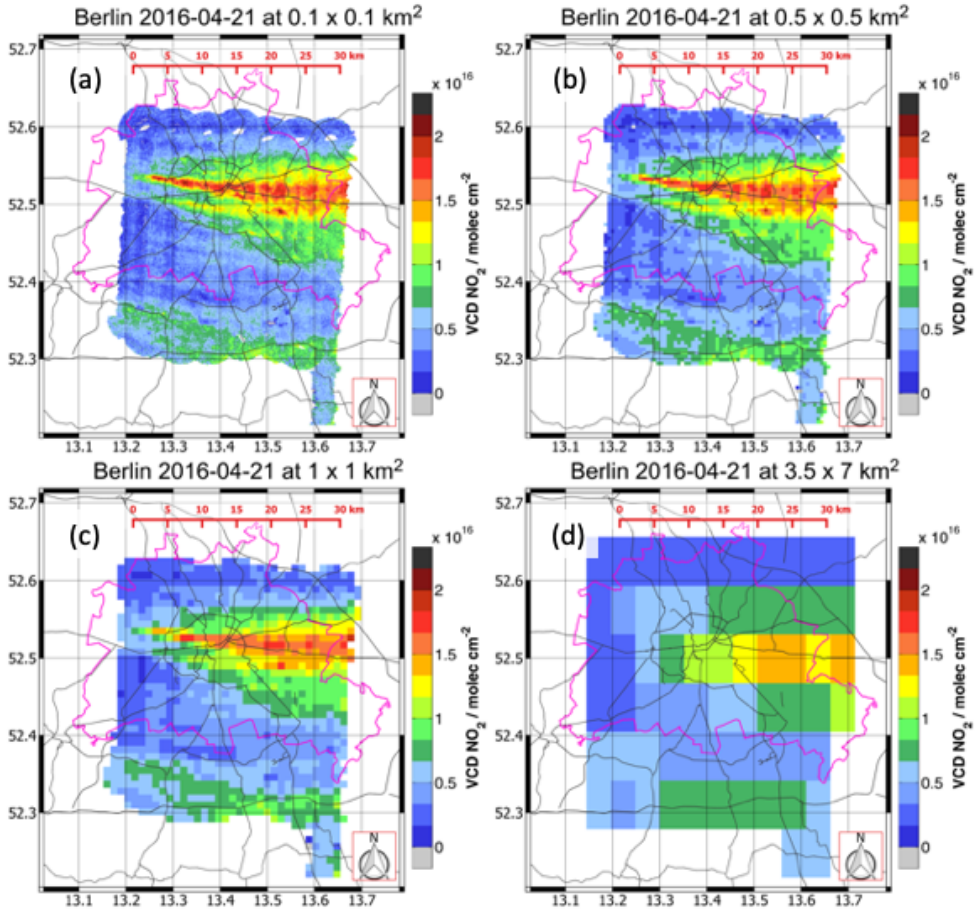

FIGURE 2.1: NO_2 VCD measured by AirMAP in the morning ($\sim$ 07:30–09:30 UTC) of April 21, 2018, averaged to a horizontal resolution of **(a)** 0.1 $\times$ 0.1 km^2, **(b)** 0.5 $\times$ 0.5 km^2, **(c)** 1 $\times$ 1 km^2, and **(d)** 3.5 $\times$ 7 km^2.

In general, the instantaneous field of view (IFOV) of an instrument determines the spatial

resolution of its measurements; thus, a low IFOV leads to a higher spatial resolution. However, a low IFOV degrades the SNR, as IFOV and SNR are trade-off parameters. The optical throughput, or etendue, which is related to SNR, is limited by the IFOV. Therefore, a super-low-altitude satellite is expected to be an important breakthrough for improving the spatial resolution of air quality monitoring, because it is easy to manage the trade-off parameters at low altitudes. In 2017, the Super Low Altitude Test Satellite (SLATS) was successfully launched by the Japan Aerospace Exploration Agency (JAXA) for use as a next-generation Earth observation satellite, at an orbit height of around 200 km, which provides a high spatial resolution and greater cost reduction in terms of compact and lightweight satellite sensors and launch services (Nagano et al., 2010; Kawasaki et al., 2018). Satellite stability is challenging at low altitudes (less than 300 km), where the air drag is 1000 times greater than that at 600 km. After the demonstration, the stabilization technique could contribute a satellite constellation at a super-low altitude to facilitate frequent and global observations for chemical weather forecasting, hazard management, and emission source identification over short and long time scales. In this thesis, I considered a satellite altitude of 300 km in addition to 600 km.

I performed simulations for various cases to derive SNRs for the given satellite instrument and to calculate the measurement errors of tropospheric NO_2 SCDs (ϵ) using the radiative transfer model (RTM) SCIATRAN, which has been developed to calculate atmospheric radiance spectra in any observation geometry (Rozanov et al., 2005), as well as the DOAS method. I defined the measurement errors, or ratio of standard deviation with mean value, as ϵ. The analytical method used in this simulation is based on previous studies (Irie et al., 2009, 2012; Noguchi et al., 2011). The method comprises three parts: the RTM calculation setup, the instrumentation setup and SNR calculation, and the DOAS retrieval method. The RTM calculation setup and DOAS retrieval method are described in detail in Sections 2.2.1 and 2.2.3, respectively. Section 2.2.2 describes the given instrumentation setup and the SNR derivation.

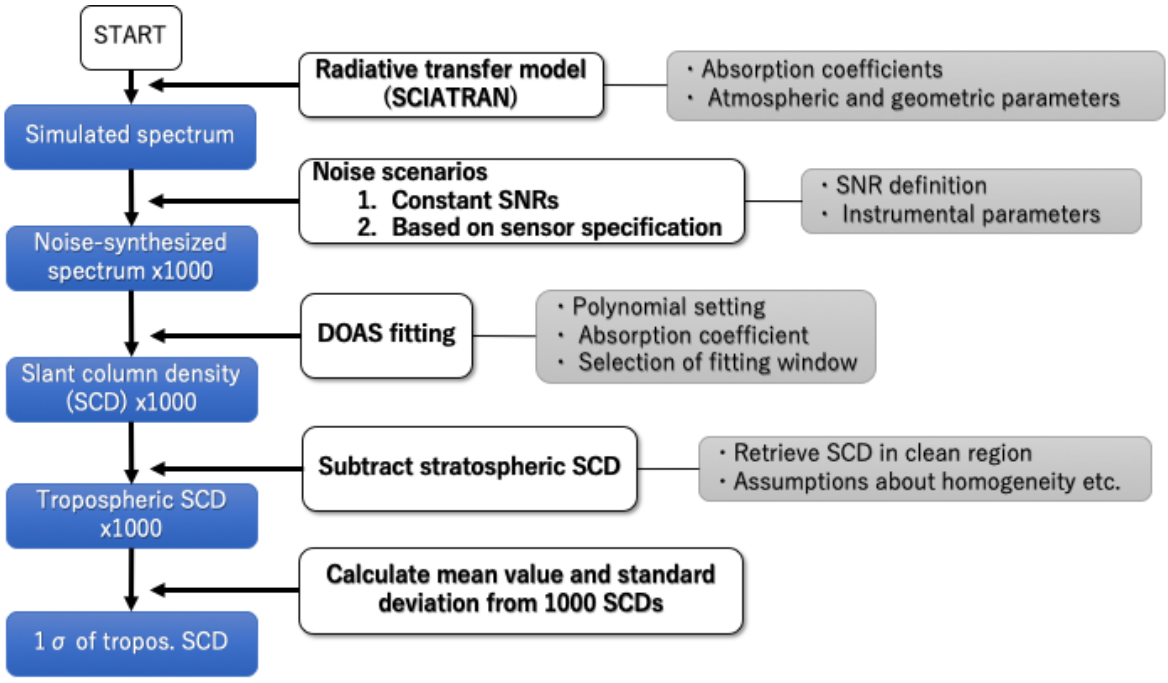

FIGURE 2.2: Flowchart of sensitivity study algorithm.

In this thesis, I determined the scientifically required measurement error to be 5% (corresponding to around 3×10^{15} molec cm^{-2} tropospheric NO_2 VCD under polluted conditions) on the basis of results obtained in previous investigations for a representative area of interest (Beijing) (Ma et al., 2013; Hendrick et al., 2014). I adopted Beijing area (40.5°N, 115.3°E) as a

representative of hotspot of NO_2 emission. Ma et al. (2013) reported that the daily mean values of the NO_2 tropospheric VCDs in the Beijing area, which is the most heavily polluted city in East Asia, ranged from 0.2 to 16.8 with an average of 5.8 in winter, and 0.5 to 13.3 with an average of 3.6 in summer from 2008 to 2011, in units of 10^{16} molec cm^{-2}. Therefore, I assumed that a scientific requirement of less than 5% would be sufficient to detect NO_2 hot-spots and to identify individual sources, although it should be noted that satellite observations over this site had negative biases of up to 50% because of the NO_2 horizontal gradients, the assumed profile shape of NO_2, and aerosols, as well as systematic differences between the two observational bases (Ma et al., 2013; Kanaya et al., 2014). For comparison, I also considered an unpolluted site (Hokkaido; 43.3°N, 143.4°E) in the present study. In addition, I simultaneously considered several realistic parameters related to the NO_2 observations.

2.2.1 Radiative transfer calculation setup

I simulated Earth's backscattered radiance spectra for several cases using SCIATRAN to obtain realistic radiance spectra by considering three different parameters, namely geometry, profile shape, and surface reflectance. To ensure that our parameters were realistic, parameters such as area, season, satellite altitude, and fit window were specifically assigned as stated in Table 2.1. In addition, I simulated radiance spectra using a vertical profile of tropospheric NO_2 concentration of nearly zero for each geometry case in order to calculate the stratospheric (from the tropopause up to the top of the atmosphere) contribution of NO_2 in the subsequent analysis. I used the incident solar irradiance spectrum obtained from the data of Chance and Kurucz Chance and Kurucz (2010). The RTM calculation was performed using the discrete ordinate method from 401.0 to 500.0 nm in wavelength steps of 0.01 nm under cloud-free conditions in order to avoid complicating the RTM calculation. The modeled atmosphere was set to 0–100 km with a vertical resolution of 200 m for altitudes of 0–10 km, 500 m for 10–12 km, and 1 km for 12–100 km. The radiance spectra calculated by SCIATRAN were convolved with a Gaussian slit function with a full width at half maximum (FWHM) of 0.2–0.5 nm (depending on the fit window). In addition, I considered aerosol effects for all cases in the RTM calculations. A detailed description of the aerosol effects is provided in Section 2.2.1.

TABLE 2.1: Parameter setup used in this simulation.

Parameters		**Characteristics**
Instrument	Wavelength range	425–450 nm
		425–497 nm
		405–465 nm
	Satellite altitude	300 km (IFOV = 0.19°)
		600 km (IFOV = 0.1°)
Situation	Area	Beijing (40.5° N, 115.3° E)
		Hokkaido (43.3° N, 143.4° E)
	Season	Winter (January 2010)
		Summer (July 2010)

Geometry

I considered the Beijing and Hokkaido (the northernmost prefecture of Japan) areas as examples of polluted and unpolluted regions, respectively. This is because Beijing is one of the most urbanized cities in East Asia and is thus a suitable representative polluted region (Richter et al., 2005; Kanaya et al., 2014). By contrast, the Hokkaido area is relatively clean and latitudinally similar to Beijing; thus, it is a suitable candidate for comparison. In addition, I considered two

seasons, winter (January) and summer (July), for both areas in order to consider different solar zenith angles (SZAs) and vertical profiles. I assumed that the satellite instrument was in a sun-synchronous orbit and orbiting at an altitude of 300 km or 600 km while looking at the nadir in each case. In other words, the satellite position was set to be constantly located at the zenith through the RTM calculation. Therefore, the relative azimuth angle (the angle between the sun and the satellite at the ground surface) and line-of-sight viewing angle were set to zero for each case. The SZA was set to the monthly mean value for each area and season as defined in Table 2.1 by assuming that the descending node is at 10:30 LT. Furthermore, I assumed that the observing swath width was as narrow as 200 km; thus, the effects of off-nadir measurements on the light path and the spatial resolution were negligible in this simulation.

Profile shape

Figure 2.3 shows the vertical profiles of trace gases as well as the pressure and temperature used in this simulation. I employed monthly mean results in the Beijing and Hokkaido areas from the CHASER model (Sudo et al., 2002) for the tropospheric vertical profiles of NO_2, SO_2, O_3, BrO, and HCHO in 2010, when there was a rapid increase in NO_x emissions in China (Itahashi et al., 2014). The CHASER model has been well evaluated (Sudo et al., 2002) and validated through comparisons with the MAX-DOAS NO_2 measurements (Kanaya et al., 2014). The vertical profile data were calculated with a horizontal spatial resolution of T42 ($2.8^\circ \times 2.8^\circ$) and 32 vertical layers from the surface up to about 3 hPa altitude. Subsequently, the profiles were directly combined with the annual mean values of the SOCRATES model (Brasseur et al., 1990), which is a two-dimensional global chemistry climate model of Earth's atmosphere, from the tropopause up to 100 km, with the same profile shape for all cases. The (thermal) tropopause altitudes were determined by the lapse rate derived from the temperature profiles of the CHASER results on the basis of the WMO 1985 definition. Finally, the vertical profiles were linearly interpolated to the grid used in SCIATRAN. As shown in Figure 2.3, the NO_2 levels in the Beijing area (red thick line) were at most ten times higher from the surface to around 2 km compared to those in the Hokkaido area.

Surface reflectance

Figure 2.4 shows the distribution of the monthly mean values of OMI/Aura Surface Reflectance Climatology Level 3 Global 0.5deg Lat/Lon Grid data (OMLER) (Kleipool et al., 2008) for the period 2005–2009 in January (upper) and July (lower). Similar surface reflectance and the seasonal trend between Beijing and Hokkaido can be seen in the rectangular region surrounded by broken lines, which represents the grid of the CHASER model. As shown in Figure 2.5, the monthly mean values of surface reflectance data extracted in the above-mentioned grid ranged from around 0.05 to 0.08 with a negative peak in summer in Beijing (red line), whereas in Hokkaido (blue line), they ranged from 0.04 to 0.07 with the same trend but were smaller by 0.01 compared to those in Beijing except in August. On the basis of these data, I employed 0.05 and 0.1 as the typical values of surface albedo in both Beijing and Hokkaido in summer and winter, respectively. Lambertian surface reflectance was assumed in the RTM calculations.

Aerosol

I considered aerosols in the RTM calculations to simulate a realistic atmosphere. Scattering or absorption by aerosols influences the NO_2 VCD calculation through the air mass factor (AMF) term (Boersma et al., 2004, 2011). Typical aerosol scenarios were considered for each area and season on the basis of mixing states described by Hess et al. (1998) (see Table 2.2). The vertical profiles of the aerosol extinction coefficients used in RTM calculations are shown in Figure 2.6.

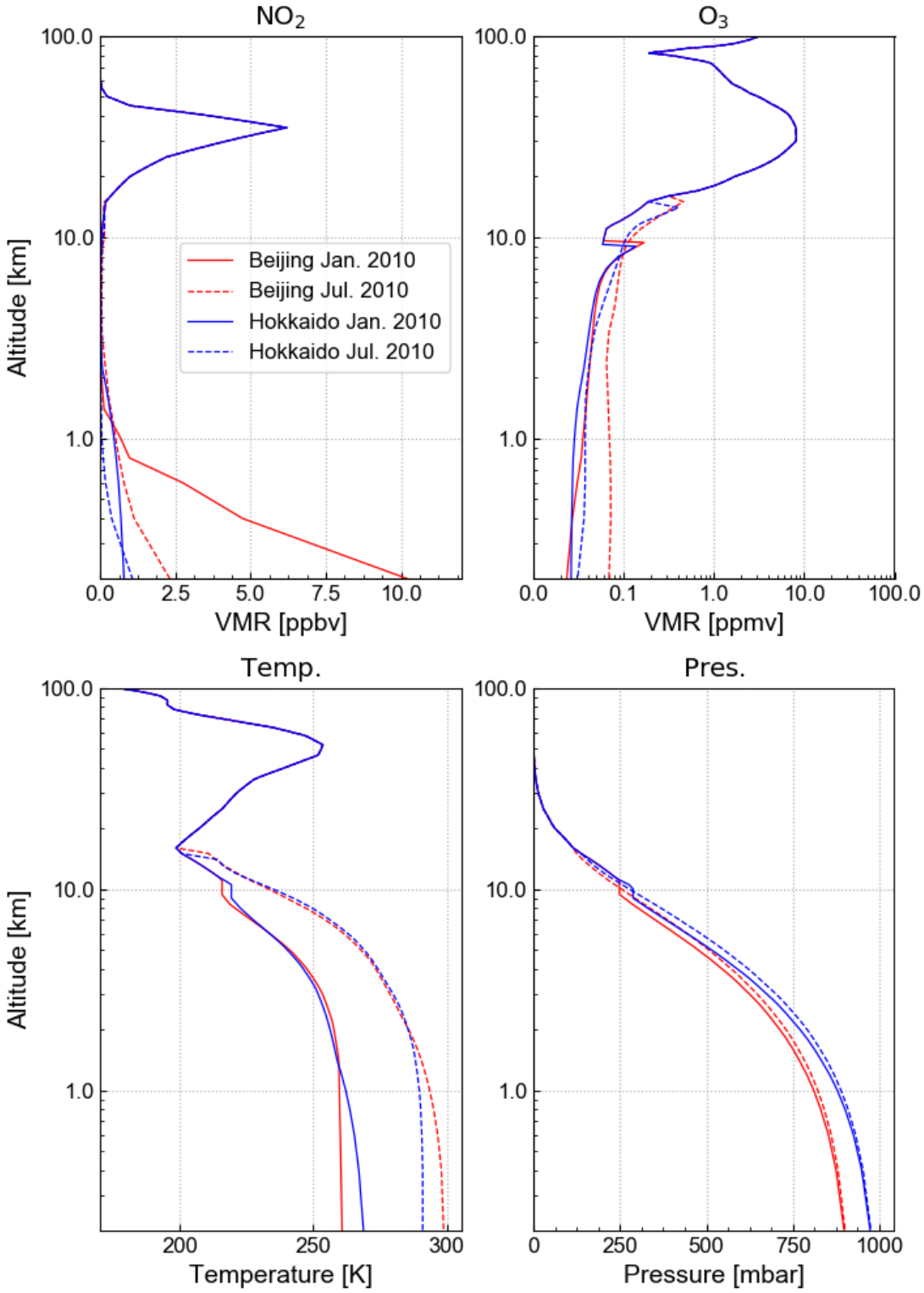

FIGURE 2.3: Vertical profiles of NO_2, ozone, pressure, and temperature used in SCIATRAN for each area and season.

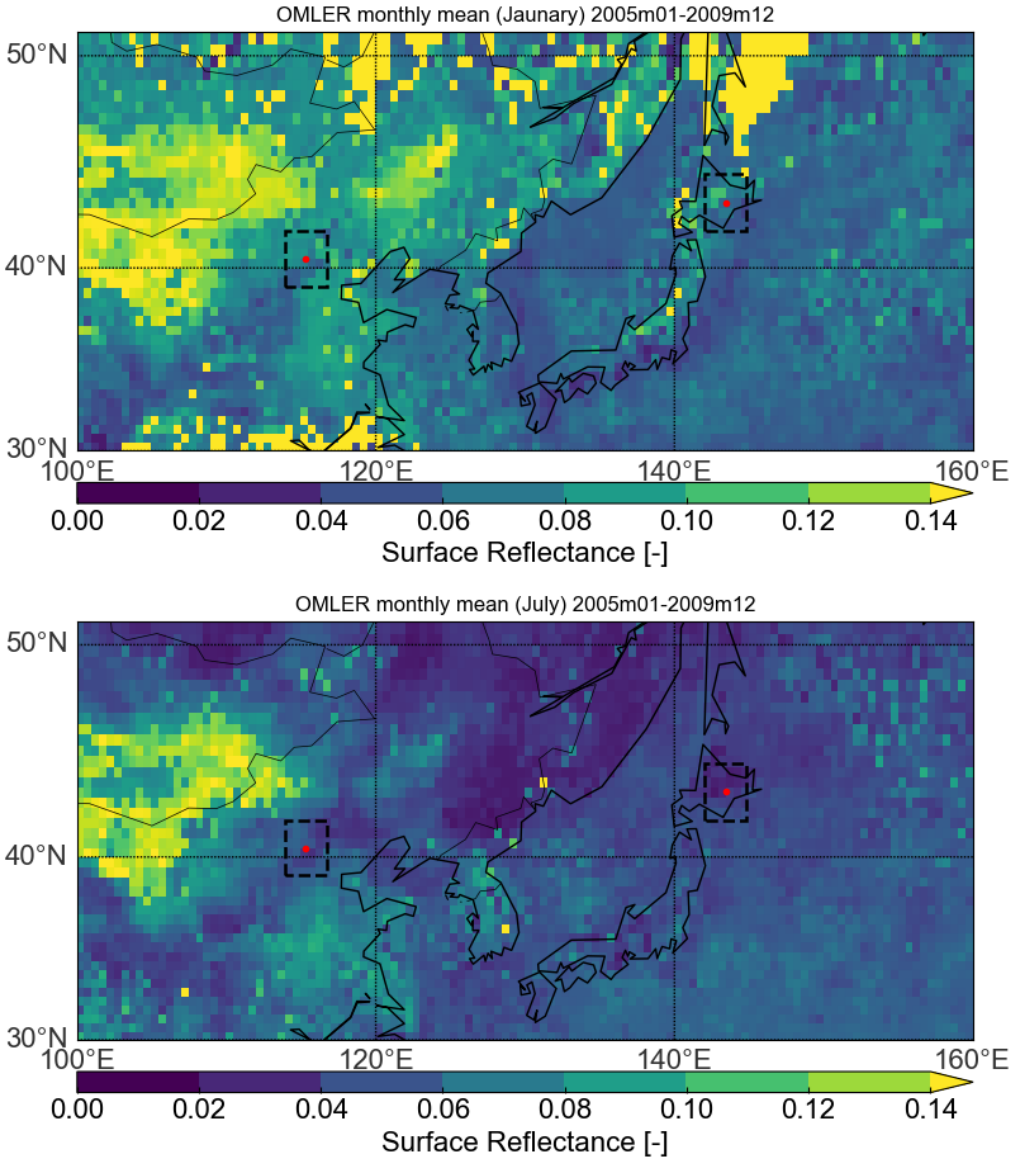

FIGURE 2.4: Monthly mean maps of surface reflectance taken from OMI/Aura Surface Reflectance Climatology L3 Global Grid data for (**top**) January and (**bottom**) July. The data were obtained from January 2005 to December 2009. The red circles in both panels represent the Beijing and Hokkaido areas, and the rectangles with broken lines represent the grids of the CHASER model.

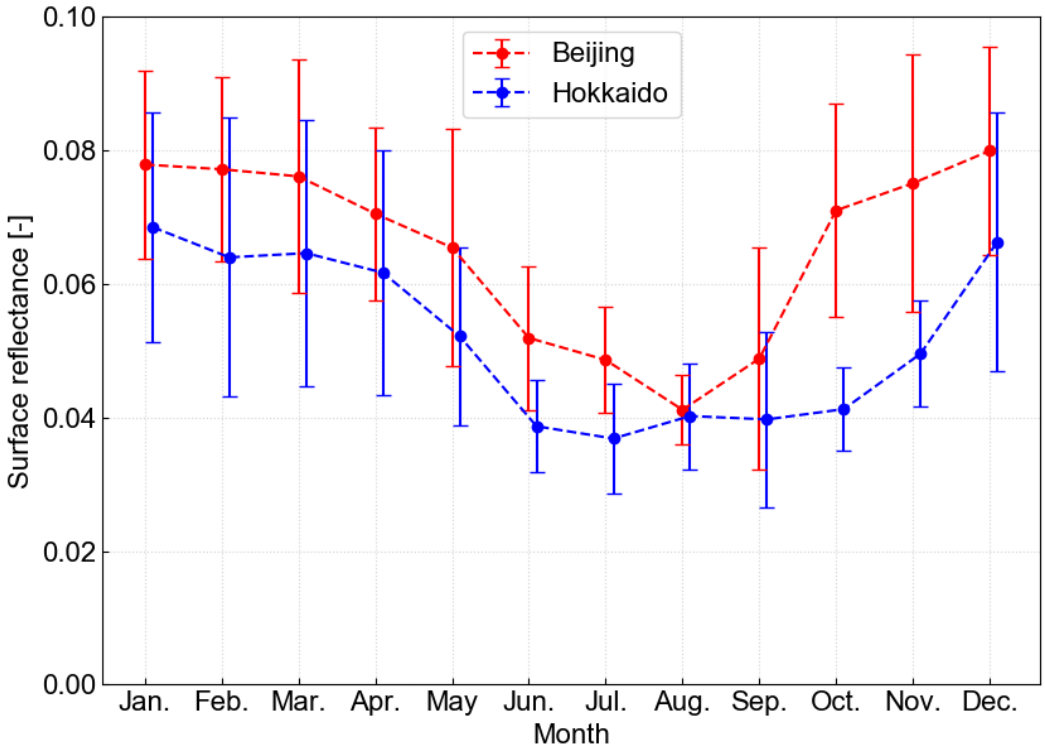

FIGURE 2.5: Seasonal trend of the OMLER surface reflectance data in the same period as Figure 2.4. The circles represent the mean values of the surface reflectance for the Beijing and Hokkaido areas, and the bars represent the one-sigma standard deviations for each month.

The aerosol extinction coefficient profiles decreased exponentially with height, with a scale height of 3 km from the surface to 2 km, 8 km from 2 km to 10 km, and 99 km from 10 km to 100 km. The detailed aerosol scenarios are summarized in Table 2.2.

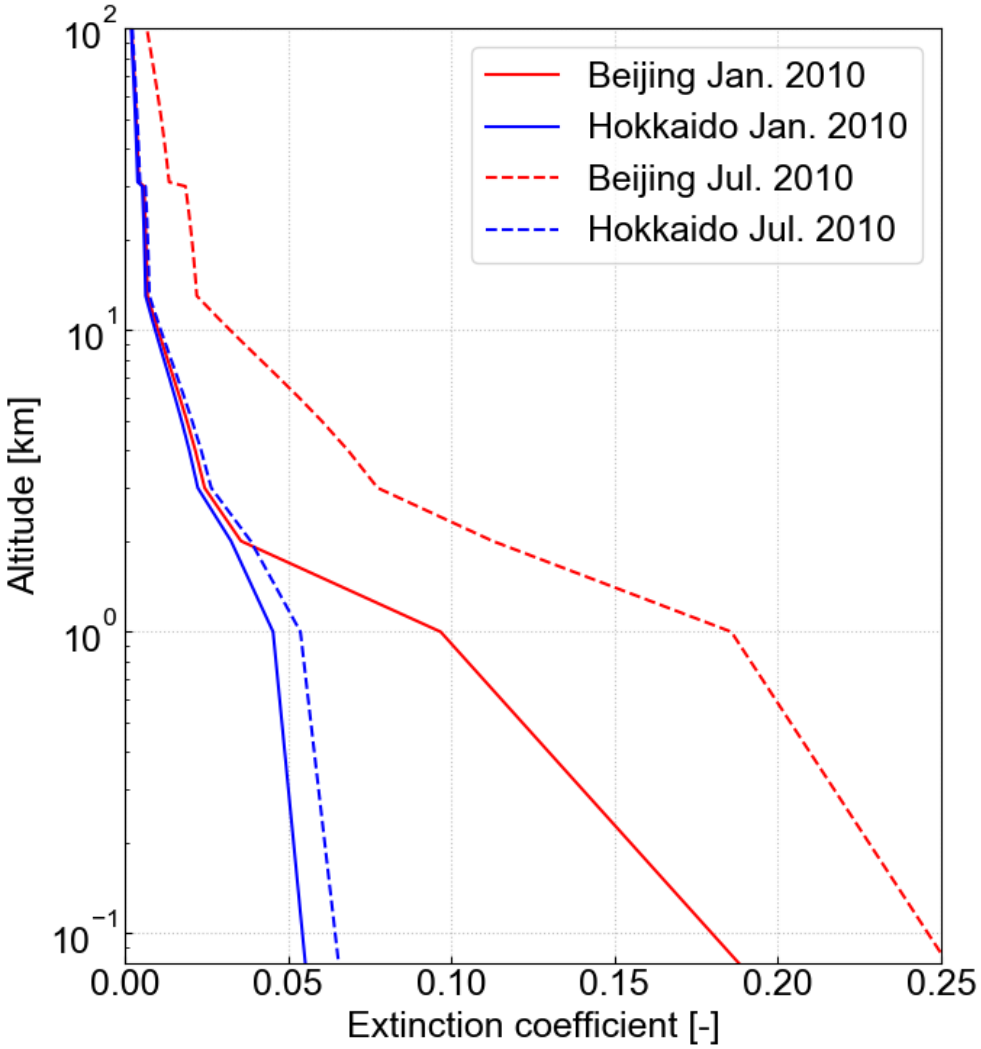

FIGURE 2.6: Vertical profiles of aerosol extinction coefficients for each area and season.

2.2.2 Instrumental setup and the SNR calculation

In this thesis, I consider a new satellite instrument employing a two-dimensional CMOS array sensor and a compact, robust, and cost-effective optical system with aberration-corrected convex gratings, suitable for use in a satellite constellation for global air quality monitoring. The grating imaging spectrometer employed In this thesis was based on the spectrometer described by Kuze et al. (2015) and Kuze et al. (2018), covering a wide swath without a moving mechanism on the basis of satellite motion to observe the entire globe. The spectrometer can easily employ a custom-designed grating and foreoptics. As mentioned above, IFOV and SNR are trade-off parameters, and they can be tuned by small foreoptics. The satellite instrument concept used In this thesis has two major features: one is a high spatial resolution of 1×1 km^2, and the other is a compact optical system covering a spectral window optimized for NO_2 retrieval.

TABLE 2.2: Aerosol scenarios for each region and season.

Area	**Layer Num.**	**Altitude range**	**Aerosol types**	**Components and number mixing ratio**	**Relative humidity**
Beijing	#1	0–2 km	Urban	Water soluble: 0.177 insoluble:0.949E-5 soot:0.823	Winter : 50% Summer: 70%
	#2	2–10 km	Continental average	Water soluble: 0.458 insoluble:0.261E-4 soot:0.542	Winter : 50% Summer : 70%
	#3	10–30 km	Sulfate	sulfate: 1	0%
	#4	30–100 km	Meteoric	meteoric dust: 1	0%
Hokkaido	#1	0–2 km	Continental average	Water soluble: 0.458 insoluble:0.261E-4 soot:0.542	Winter : 70% Summer : 80 %
	#2	2–10 km	Continental average	Water soluble: 0.458 insoluble:0.261E-4 soot:0.542	Winter : 70% Summer : 80%
	#3	10–30 km	Sulfate	sulfate: 1	0%
	#4	30–100 km	Meteoric	meteoric dust: 1	0%

Irie et al. (2009) performed sensitivity studies for the instrumentation concepts of GMAP-Asia and quantitatively showed the relationship between measurement precision and sensor specifications. Following the analytical method proposed by Irie et al. (2009), Noguchi et al. (2011) demonstrated that the diurnal variation of tropospheric NO_2 over Tokyo can be detected by the GMAP-Asia UV/visible sensor with a FWHM of 0.4 nm and a sampling ratio of 4 (number of pixels per FWHM) at SNR > 500. Noguchi et al. (2014) also investigated the effect of surface reflectance anisotropy on tropospheric NO_2 measurements assuming the GMAP-Asia UV/visible sensor specifications. The present study focused not on a GEO satellite instrument but on a LEO satellite instrument.

I introduced the following assumptions about the instrument and its performance to simulate the realistic SNR of the detector:

- a two-dimensional Si–based CMOS array sensor with a size of 13×13 mm^2 was assumed for an individual detector,
- the size of one pixel was assumed to be 6.5 μm and 10 pixels were binned,
- an empirical detectivity considering the degradation due to the array and read out electronics was introduced and assumed to be 2.0×10^{13} cm Hz$^{1/2}$ W^{-1},
- the optical efficiency including the quantum efficiency was assumed to be 0.43.

Neither the optical efficiency nor the quantum efficiency of the detector can be accurately quantified in advance; hence, the systematic errors related to the instrument were not considered In this thesis, although the optical parameters summarized in Table 2.3 are realistic on the basis of nominal proposed specifications.

I considered two types of SNRs. One is a constant SNR (500, 2000, 5000, and 10000), and the other is a more realistic type that depends on the sensor specifications and is defined as follows:

$$SNR_{det} = \frac{D^* L A_c \Omega \Delta\nu \eta}{A_d^{1/2} \Delta f^{1/2}}, \tag{2.1}$$

$$SNR_{total} = \frac{1}{\sqrt{\left(\frac{1}{SNR_{det}}\right)^2 + \left(\frac{1}{SNR_{sn}}\right)^2 + \left(\frac{1}{SNR_{dc}}\right)^2}}, \tag{2.2}$$

where

D^*: detectivity [cm Hz$^{1/2}$ W^{-1}],
L: luminance measured by the detector [W m^{-2} str^{-1} μm^{-1}],
A_c: optical system area [m^2],
Ω: targeting solid angle [str],
$\Delta\nu$: spectral resolution [nm],
η: optical efficiency [-],
A_d: detector area [m^2],
Δf: frequency [s^{-1}],
SNR_{sn}: SNR of the shot noise, and
SNR_{dc}: SNR of the dark current.

SNR_{det} in Equation 2.2 represents the SNR of the read noise of the detector. D^* is a plausible detectivity value as described previously. The term $A_c \cdot \Omega$ represents the etendue of the optical system. The SNRs of the shot noise and dark current of the CMOS detector are represented as SNR_{sn} and SNR_{dc}, respectively, and defined as follows: $SNR_{sn} = \sqrt{(L A_c \Omega \Delta\nu \eta \Delta t) \cdot \lambda / hc}$, $SNR_{dc} = SNR_{sn}\sqrt{\Delta t\, dc}$, where Δt denotes the integration time in seconds and dc dark current [e pixel^{-1} s^{-1}] (= 120), respectively. The parameters used in the equations are listed in Table 2.3. In the following section, SNR_{total} is simply referred to as SNR without a subscript.

TABLE 2.3: Characteristics of the optical system assumed in the present study.

Parameters	**Characteristics**
Detector size	0.065 mm
Aperture size	0.74 cm
Read noise	10 e
Dark current	120 e/pixel/s
Detector aspect ratio	1.0
Effective detector area	0.9
Optical efficiency	0.43
Slit width	0.065 mm
Time constant	0.14 s

2.2.3 DOAS retrieval

Corresponding to the above-mentioned SNRs, 1000 different patterns of random noise were added to one radiance spectrum convolved with a slit function. I obtained 1000 spectra for each case of areas, seasons, satellite altitudes, and surface albedo values. I derived NO_2 SCDs from these spectra using the DOAS method (Platt, 1994). The DOAS method is a well-established method for retrieving amounts of trace gases having spectral absorption features in the UV/visible range; it has been adopted in previous studies (Burrows et al., 1999; Bovensmann et al., 1999). I used three different well-validated wavelength domains for the DOAS fitting, i.e., 425–450 nm, 425–497 nm, and 405–465 nm, in order to investigate the optimal fit window for NO_2 retrieval, as our instrument is specialized for NO_2 observations. The wavelength range of 425–450 nm is a basic fit window that is frequently used for NO_2 retrieval, e.g., GOME measurements (Richter and Burrows, 2002). The improved fit window of 405–465 nm has been used for OMI measurements (Bucsela et al., 2006), while the wavelength range of 425–497 nm has been used for improved GOME-2 NO_2 retrieval by Richter et al. (2011). To exclude large-scale wavelength trends that include the effects of aerosols and other factors, a third-degree polynomial was used in the DOAS fitting. The absorption cross-sections for trace gases (NO_2, O_3, H_2O, O_4) and the Ring effect used in the DOAS fitting are shown in Figure 2.7.

The total NO_2 SCDs were separated into tropospheric and stratospheric contributions by subtracting the stratospheric NO_2 SCDs from the total SCDs in order to determine the tropospheric NO_2 SCDs. I used a method similar to the reference sector method (Velders et al., 2001; Richter and Burrows, 2002; Martin et al., 2002) to derive the tropospheric NO_2 contribution. This method regards the total NO_2 SCD over unpolluted regions (e.g., Pacific ocean) as the stratospheric NO_2 SCD through RTM calculations for each geometry. I used the results of the CHASER model in the Pacific region (180° E), where the contribution of the tropospheric NO_2 to the total NO_2 SCD is small. Finally, I calculated the mean values and one-sigma standard deviations of the tropospheric NO_2 SCD distribution fitted with a Gaussian shape to estimate ϵ of the NO_2 observations for each case.

2.3 Observation performance and capability studies

2.3.1 Determination of feasibility

Our target measurement precision is better than 5% (corresponding to 3.0×10^{15} molec cm^{-2} in a highly polluted area) for a tropospheric NO_2 VCD. This corresponds to a tropospheric NO_2 SCD of around 3.0×10^{15} molec cm^{-2} or less when using a tropospheric air mass factor (box air mass factor; b-AMF) of around 1 in the polluted region. This is based on the following general

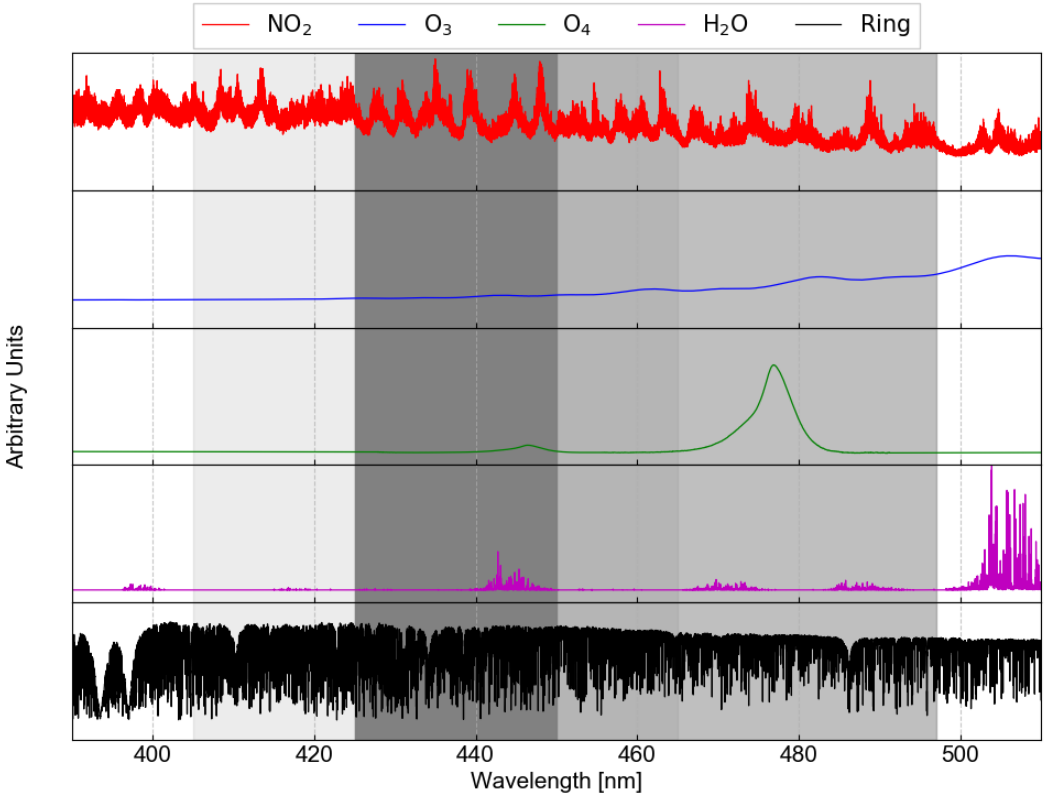

FIGURE 2.7: Absorption cross-sections of trace gases used in DOAS retrieval. The shaded areas represent each fit window; 425–450 nm (dark gray), 425–497 nm (gray), and 405–465 nm (light gray). The absorption cross-sections for NO_2 (220 K), O_3 (223 K), O_4 (293 K), H_2O, and the Ring spectrum were obtained from the work of Vandaele et al. (2002), Serdyuchenko et al. (2014), Thalman and Volkamer (2013), Rothman et al. (2009), and Vountas et al. (1998), respectively.

equation:

$$AMF = \frac{SCD}{VCD}. \tag{2.3}$$

AMF depends on cloud, aerosol, surface property, and NO_2 profile shape. To consider the contribution of these effects to the light path, AMF is calculated considering these parameters via RTM.

Figure 2.8 shows the b-AMF for each layer, calculated by SCIATRAN for each region (polluted and unpolluted), and albedo (0.05 and 0.1) in winter and summer 2010, which depends on the a priori assumed profile shape and surface albedo. The b-AMF values were mostly less than 1 from the surface to 1 km and less than 3 from 1 km to the tropopause for the wavelength domain in both seasons, indicating that the tropospheric b-AMF was as small as 1 or less owing to the presence of aerosols, although the b-AMF above 10 km was nearly always greater than 3. With a surface albedo of 0.1, the b-AMF values at longer wavelengths were higher than those at shorter ones from the surface to the tropopause in both polluted and unpolluted regions.

Comparison between different geometries

I calculated the SNRs for the given sensor specifications and then retrieved the tropospheric NO_2 SCDs using the DOAS for each considered case. Figures 2.9 and 2.10 show the retrieved

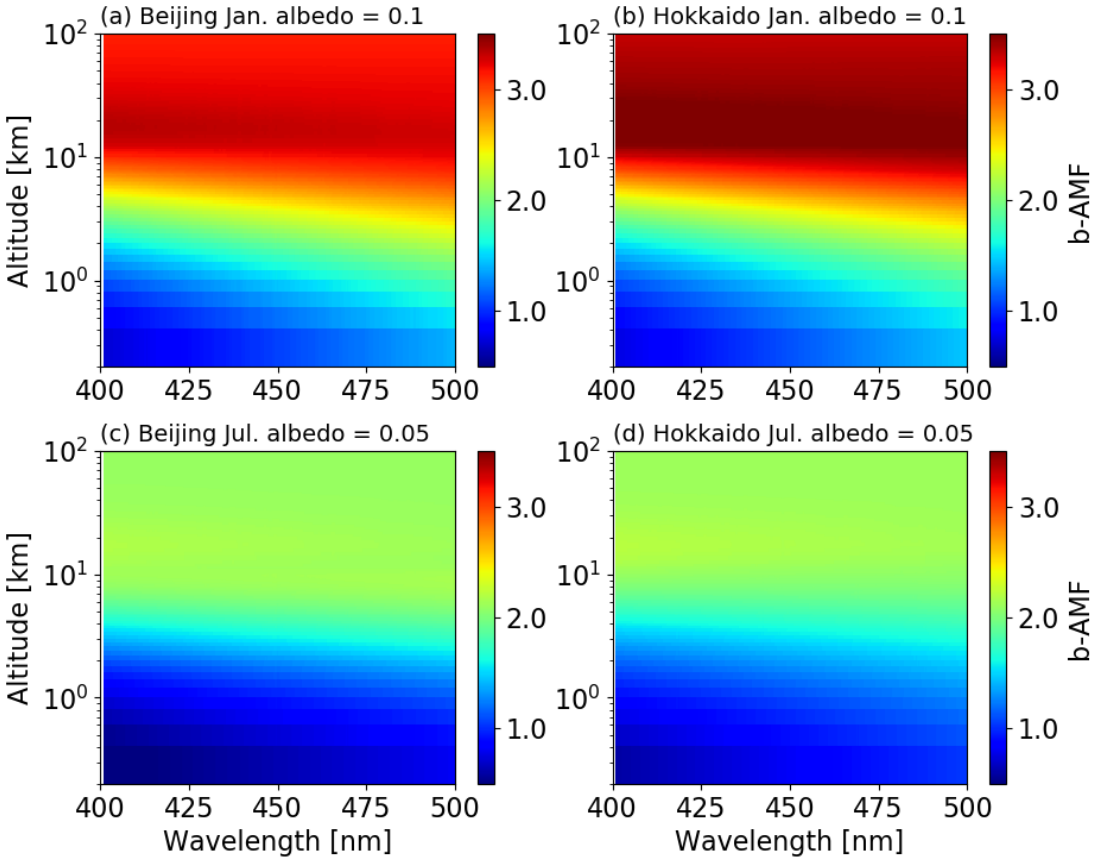

FIGURE 2.8: Box air mass factor (b-AMF) calculated by SCIATRAN for January and July 2010 for polluted (**a,c**) and unpolluted (**b,d**) regions.

tropospheric NO_2 SCDs and the relative errors calculated in the two seasons for each SNR in the Beijing and Hokkaido areas, respectively. Each SNR represented by a solid circle was calculated at 450 nm for the given sensor specification using different fit windows and then shifted at a center wavelength of each fit window, while the SNRs represented by open circles were a series of constant SNRs (i.e., 500, 2000, 5000, and 10000). Due to shifting at a center wavelength of each fit window, calculated SNRs were slightly different arising from the variation of the spectral resolution in a range of 0.12–0.35 nm. The results using 425–497 nm showed the highest SNRs of around 1000 in winter and around 1300 in summer in both areas, while the results using 405–465 nm showed the lowest SNRs. They depend on different seasons, or SZAs, although they are comparable in both areas during the same season. It is interesting that in the case of enhanced NO_2 existing at the surface level (Figure 2.9(a)), the tropospheric NO_2 SCD retrieved using 405–465 nm shows the lowest value (5.9×10^{15} molec cm^{-2} at SNR = 920), although in the other cases of lower surface NO_2 levels (Figure 2.9(b)), the SCDs retrieved using 425–497 nm were the lowest. I believe that this is due to the wavelength dependency of radiance intensity calculated by RTM because aerosol phase function assumed in each case (polluted, moderately polluted and unpolluted) cause the difference of reflectance properties. When I assume that the tropospheric b-AMF is nearly 1 in all the cases, the tropospheric NO_2 VCDs are comparable with the NO_2 SCDs; thus, the tropospheric NO_2 VCDs calculated in Beijing in winter were 3–6 times larger than those in the other cases depending on the fit windows and geometries. In the polluted region of interest, the standard deviations of the tropospheric NO_2 SCDs ranged from 0.19 to 0.27 $\times$ 10^{15} molec cm^{-2} (corresponding to 0.13–0.18 $\times$ 10^{15} molec cm^{-2} total NO_2 SCDs) in winter for all the fit windows, although in summer, they were as low as around 0.1 because higher SNRs were achieved. In winter, the ϵ calculated using all the fit windows met our requirements (3%–3.8% at SNR = 920–1000), although none of the other cases showed results that met our requirements during summer.It should be noted that in the unpolluted region (Figure 2.10), the ϵ calculated using 425–497 nm increased, indicating that under clean and moderately polluted conditions, using the fit window of 425–497 nm would yield a lower ϵ.

Comparison between different satellite altitudes

Next, I compared the results calculated at different satellite altitudes (300 km and 600 km) to verify the feasibility of NO_2 detection from super-low satellite altitudes and conventional ones. In this comparison, I considered only the case of the Beijing area in winter as a representative to simplify the comparison. As shown in Figure 2.11, the ϵ values calculated using 300 km were 3.0% with SNR = 1000 (425–497 nm), 3.2% with SNR = 920 (405–465 nm), and 3.7% with SNR = 930 (425–450 nm), all of which meet the scientific requirements. However, at a satellite altitude of 600 km, they did not meet the requirements because of lower SNRs < 500 (ϵ = 6.0%–7.8%). The ϵ values at 600 km were two times larger than those at 300 km.It is obvious that a super-low satellite altitude of 300 km enables global observations with 1 $\times$ 1 km^2, which meets the scientific requirements.

Comparison between different surface albedo values

Similar to the comparison of different satellite altitudes, I compared the results calculated using different surface albedo values (0.05 and 0.1) by assuming a constant satellite altitude of 300 km and the vertical profile of Beijing in winter. As the surface albedo values in the observed area typically range from 0.04 to 0.08 annually as discussed above, it is reasonable to compare the values of 0.05 and 0.1 as typical values. Figure 2.12 shows the relationship between ϵ and the SNRs using the two albedo values of 0.05 and 0.1. The results with an albedo of 0.1 (circles) met the scientific requirements for all the fit windows, although the results with an albedo of

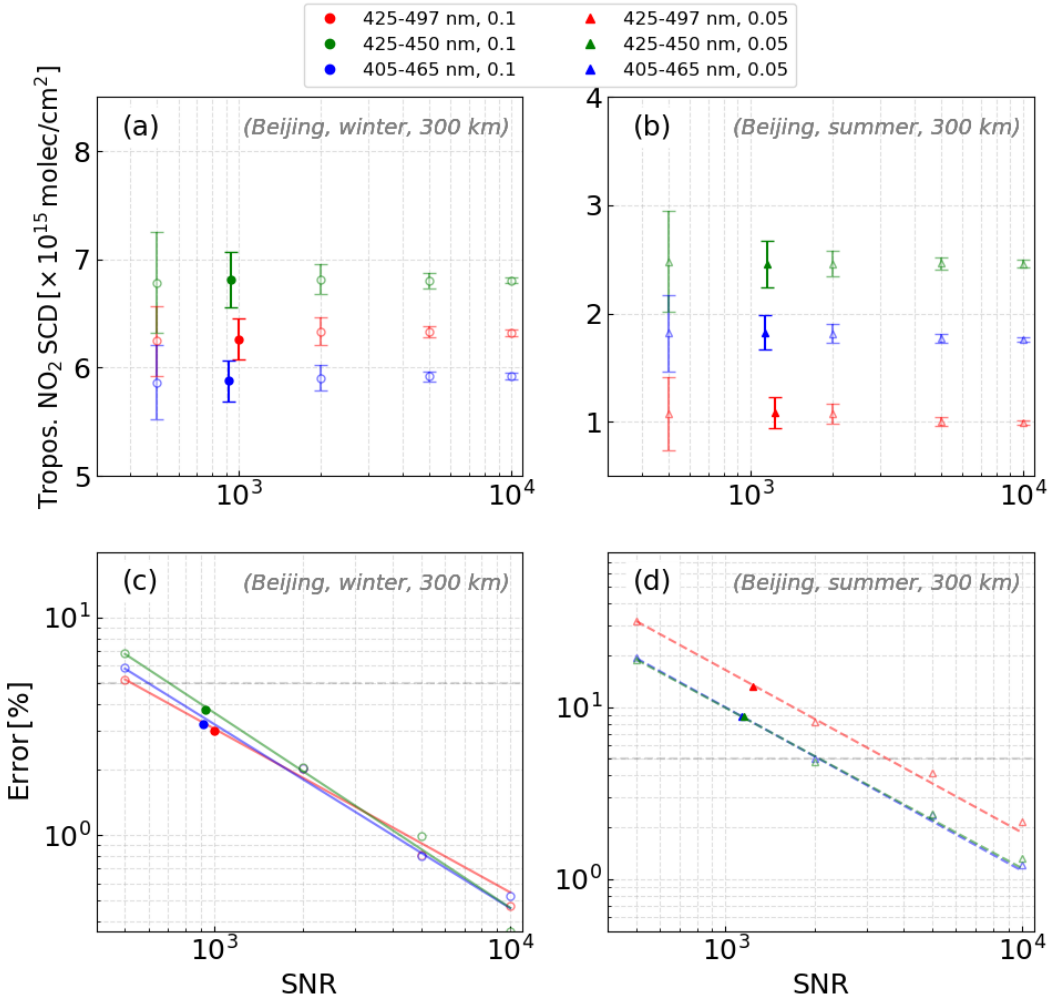

FIGURE 2.9: Tropospheric NO_2 SCDs [$\times 10^{15}$ molec. cm^{-2}] and relative error [%] calculated for (**a,c**) Beijing in winter with albedo of 0.1 and (**b,d**) Beijing in summer with albedo of 0.05 at a satellite altitude of 300 km. The different colors represent the different fit windows. Note that the y-axes in each panel have different scales and those in the lower ones have logarithmic scales. The different symbols represent different albedo values (i.e., different seasons). The solid symbols represent SNR calculated at 450 nm using the given sensor specifications, while the open symbols represent a series of constant SNRs (i.e., 500, 2000, 5000, and 10000). The error bars in the upper panels represent one-sigma standard deviations of NO_2 SCDs calculated for each SNR. The horizontal broken lines in the lower panels represent the measurement requirements of 5% NO_2 slant column uncertainty.

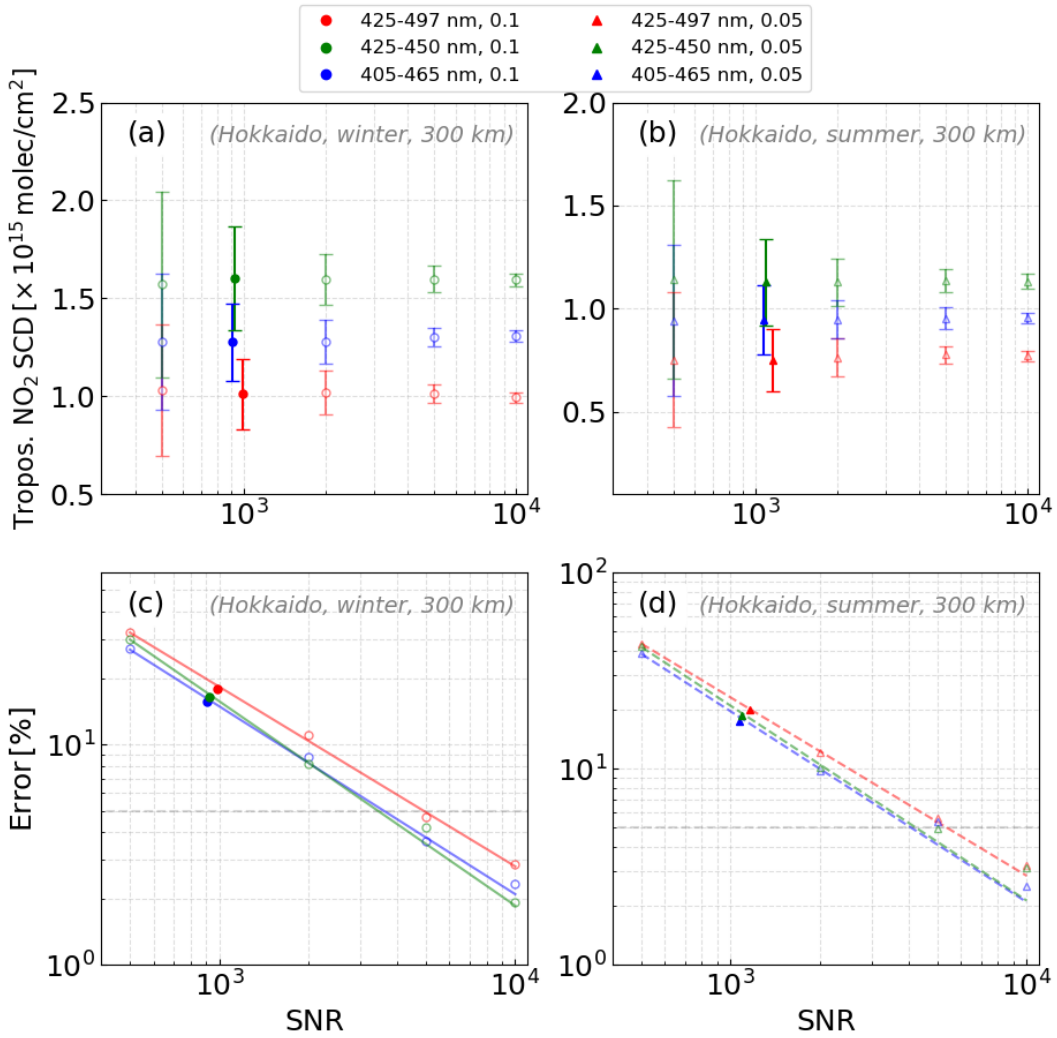

FIGURE 2.10: Same as Figure 2.9 but for Hokkaido.

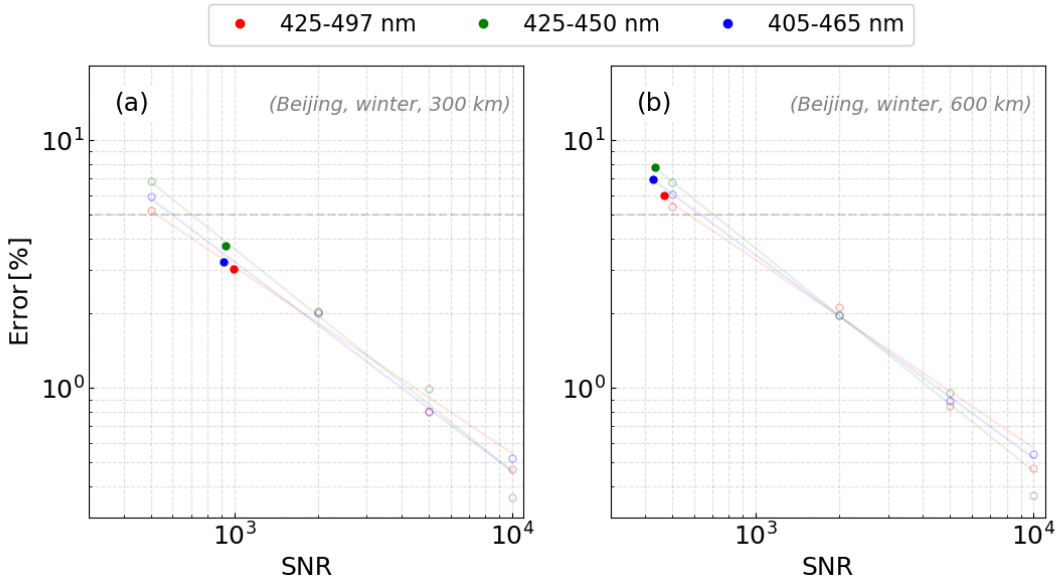

FIGURE 2.11: Measurement errors of the tropospheric NO_2 SCDs (winter) calculated with albedo of 0.1 in Beijing at different satellite altitudes: (**a**) 300 km, (**b**) 600 km. The different colors represent the results of the different fit windows.

0.05 (triangles) did not meet the requirements except for the result using 425–497 nm. The ϵ values with an albedo of 0.05 were 4.6% at SNR = 940 using 425–497 nm, 5.3% at SNR = 860 using 405–465 nm, and 5.8% at SNR = 880 using 425–450 nm.

Overall comparison

In the discussion presented above, I individually compared the results calculated using different geometric parameters, profiles, and surface albedo values. Finally, I summarized each comparison and discussed the optimal setup of the fit window and satellite altitude. The calculated SNRs depended mainly on the assumed satellite altitudes owing to the dependency of the etendue, although they were comparable at the same altitude. The other factors related to the SNRs are the surface albedo and the fit windows, which caused the SNRs to vary within 10% for the same area and satellite altitude. The site dependence contributed the least to the SNRs, with a relative error of less than 5% in the same season, although the SNRs showed much higher dependency on the difference in season (approximately 25%), which indicates that the geometry in summer (smaller SZA) results in higher SNRs than that in winter (larger SZA).

In the highly polluted case, the results using a fit window of 425–497 nm showed the fewest measurement errors, whereas in most cases, use of the 425–450 nm window resulted in the highest uncertainty. In the polluted region, from a satellite altitude of 300 km during winter, all the cases achieved measurement errors of less than 5% with SNRs of around 1000. On the other hand, at a satellite altitude of 600 km, no case met the scientific requirements even in the polluted region. In the unpolluted region, the measurement errors were as high as 15%–55% for both altitudes, although it is not necessary to strictly adhere to the scientific requirements because this region is the control region. However, it is interesting that the ϵ using 425–497 nm, which showed the lowest errors in the polluted region, resulted in high error values compared with the results derived from the other two fit windows, in spite of showing the best SNRs.

In summer, no results met the scientific requirements in the simulated cases. It should be noted that the results in summer showed fewer differences in the relative errors with regard to the fit windows than those in winter, implying that the choice of the fit window is more

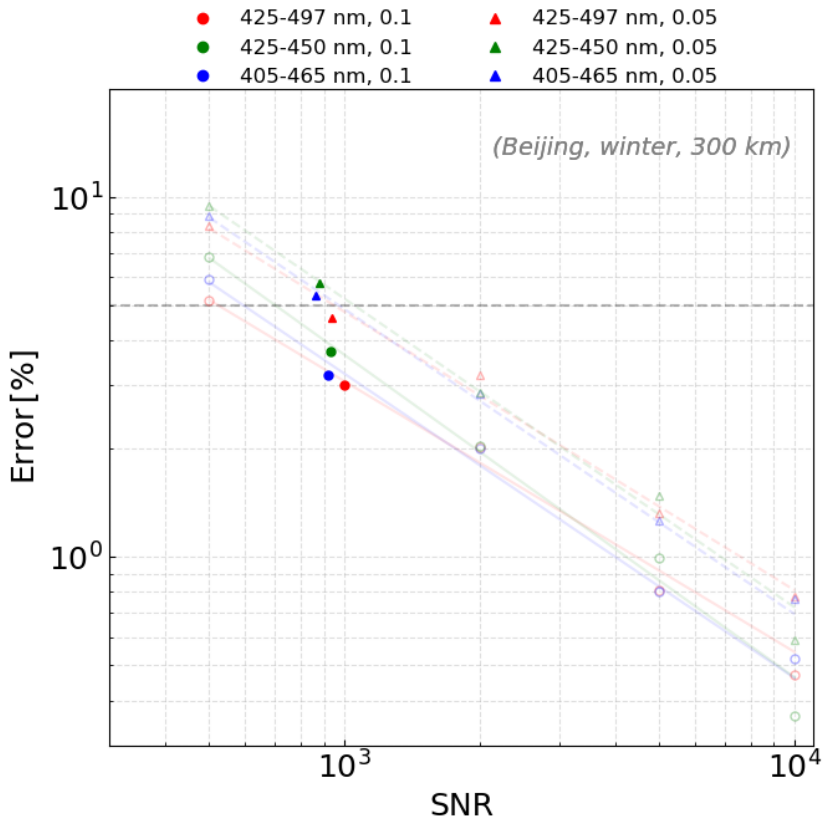

FIGURE 2.12: Measurement errors of the tropospheric NO_2 SCDs (winter) calculated at a satellite altitude of 300 km in Beijing with different surface albedos of 0.05 (circle) and 0.1 (triangle). The different colors represent the different fit windows. Note that the y-axes in each panel have different scales.

significant for NO_2 retrieval, especially in the polluted region and during winter, when the surface NO_2 tends to remain near the emission source.

Table 2.4 shows a summary of uncertainty estimates for each case calculated at a satellite altitude of 300 km. The relative differences in Beijing ranged from 3.0% to 13.3% largely depending on the season (i.e., profile shape) and fit window although those in Hokkaido ranged from 15.6% to 20.0% that were relatively high. On the basis of these results, I propose that the combination of a fit window of 425–497 nm and a satellite altitude of 300 km would be optimal for the proposed satellite instrument to achieve the scientific requirements when making observations in polluted regions. In the moderately polluted case, use of the 405–465 nm window resulted in fewer measurement errors than use of the 425–497 nm window, although it still did not satisfy the requirements. Therefore, the 405–465 nm fit window may be suitable when observing moderately polluted regions (around 3.0×10^{15} molec cm^{-2}). However, it should be noted that additional correction about aerosol should be performed in further steps because 405–465 nm (and also 425–450 nm) does not include O_4 dimer which has aerosol information and a spectral feature at 477 nm. Using the aerosol data derived from global model such as GEOS-Chem (Wang et al., 2004) should be suggested but introducing the uncertainty of 40% at maximum (Boersma et al., 2007). However excluding aerosol effect leads to changes between -40% and 90% with aerosol optical depth > 0.8 (Lin et al., 2014).

TABLE 2.4: Summary of uncertainty estimates for each case (satellite altitude of 300 km and surface albedo is fixed as 0.1 in winter and 0.05 in summer).

Area	**Season**	**Uncertainties [$\times$ 10^{15} molec. cm^{-2}] (%)**		
		425–450 nm	425–497 nm	405–465 nm
Beijing	Winter	0.26 (3.7)	0.19 (3.0)	0.19 (3.2)
	Summer	0.21 (8.9)	0.14 (13.3)	0.16 (8.8)
Hokkaido	Winter	0.26 (16.5)	0.18 (17.9)	0.20 (15.6)
	Summer	0.21 (18.7)	0.15 (20.0)	0.17 (17.6)

2.3.2 Assessment of the sources of systematic error

The total error for the retrieved tropospheric VCD is determined by three main error sources: the measurement noise and systematic SCD errors, errors from the separation of the stratospheric and tropospheric NO_2, and errors from the uncertainties of the model parameters through the AMF calculation. The measurement noise is a source of random error. The systematic SCD errors include imperfect wavelength calibration, reference spectra errors, and spectral features of an instrument. These errors were negligible in this simulation on the basis of assumptions that the reference spectra used are true spectra and that there are no spectral features of an instrument. The errors from the separation of the stratospheric and tropospheric NO_2 depend on the uncertainties in the stratospheric NO_2 SCD, which is generally estimated to be of the order of 0.1–0.2 $\times$ 10^{15} molec. cm^{-2} (Dirksen et al., 2011). The errors from the AMF calculation consist of uncertainties in the model parameters, such as clouds, aerosols, and surface albedo, as well as the a priori NO_2 profile shape, which is estimated to be as large as up to 29% (Boersma et al., 2004) on average in the region with large NO_2 emission sources, and it can have a considerable impact on the spatial distribution of NO_2 retrieved with kilometer-order resolution. Therefore, in practical retrieval of the tropospheric NO_2 VCD using a LEO satellite instrument, validation and model assimilation are required in subsequent analyses.

Boersma et al. (2004) proposed an equation for the overall error variance of the tropospheric column owing to a satellite instrument considering error propagation. Based on this equation, the overall error for the tropospheric NO_2 retrieval was approximated as 0.88 $\times$ 10^{15} molec cm^{-2} under polluted conditions, assuming that the tropospheric AMF is 1 and that the error from the tropospheric AMF is 25%. This result is in good agreement with the scientific requirements assumed In this thesis.

2.4 Summary and conclusions of this chapter

In this thesis, I determined the optimal fit window, satellite altitude, and sensor specification to meet the scientific requirements of measurement errors (5%) for tropospheric NO_2 observations using a small LEO satellite instrument with 1 $\times$ 1 km^2 horizontal resolution by simulating random instrumentation errors in the NO_2 SCDs. Specifically, I simulated backscattered radiance spectra in polluted and unpolluted regions (Beijing and Hokkaido, respectively) at two different satellite altitudes (300 km and 600 km) for two seasons (winter and summer), and I statistically analyzed the retrieved tropospheric NO_2 SCDs using the DOAS method to derive the relative SCD errors. As a result of the comprehensive analysis, the lower satellite altitude of 300 km was determined to be suitable to meet the scientific requirement of 5% for the tropospheric NO_2 SCD. The measurement error in the polluted region of interest (Beijing) met the scientific requirement of 5% at an SNR of around 1000 with a precision of 2%–4% for all the fit windows in the case of a satellite altitude of 300 km, while a satellite altitude of 600 km did not meet the requirements in the same situation. In the analysis for different surface albedo values

TABLE 2.5: Summary of specifications for existing/future satellite instruments observing NO_2 within the UV/vis range and comparison with the proposed specification used In this thesis.

Instrument (Platform)	**Footprint**	**Satellite altitude**	**Spectral coverage**	**Spectral resolution**	**Uncertainty**†
Unit	[km^2]	[km]	[nm]	[nm]	[molec cm^{-2}]
This study	1×1	300	425–497	0.35	$0.14\ (0.19) \times 10^{15}$ [a]
GOME (ERS-2)	40×320	800	240–790	0.2–0.4	$0.2–0.4 \times 10^{15}$ [b]
SCIAMACHY (ENVISAT)	30×60	800	214–812	0.2–0.5	1.4×10^{15} [c]
OMI (Aura)	13×24	705	270–500	0.45–1.0	0.67×10^{15} [d]
GOME-2 (Metop-A,B,C)	40×80	817	240–790	0.2–0.4	0.45×10^{15} [e]
TROPOMI (Sentinel-5P)	3.5×7	824	270–495	0.25–0.55	0.7×10^{15} [f]
Spectrolite	1 km [g]	600	320–495	< 0.5	$< 3 \times 10^{15}$ [h]

†Random errors of total slant columns.
[a] Uncertainties of total (tropospheric) NO_2 SCDs estimated In this thesis.
[b] Richter and Burrows (2002). Boersma et al. (2004) reported 0.55×10^{15} molec. cm^{-2}.
[c] Richter et al. (2011).
[d] Boersma et al. (2007).
[e] Valks et al. (2011). Richter et al. (2011) also reported 1.2×10^{15} molec cm^{-2} but using 425–497 nm instead of 425–450 nm.
[f] van Geffen et al.
[g] On across track. IFOV = 0.1°.
[h] de Goeij et al. (2017).

(0.05 and 0.1), only a fit window of 425–497 nm met the scientific requirements (3% at SNR = 1000 with albedo = 0.1 and 4.6% at SNR = 940 with albedo = 0.05). In the moderately polluted case, use of the 405–465 nm window may be suitable because lower measurement errors are achieved compared to use of the 425–497 nm window, although it still did not satisfy the requirements. Therefore, a combination of a fit window of 425–497 nm and a satellite altitude of 300 km is likely to be the optimal combination for the satellite instrument considered In this thesis.

Table 2.5 summarizes the proposed sensor specifications compared to existing/potential satellite sensor specifications as well as the proposed spectrometer specification. The error estimation analysis considering the error propagation, including the AMF uncertainty, implied that the overall error for the tropospheric NO_2 retrieval was expected to be 0.88×10^{15} molec cm^{-2}, which is consistent with the scientific requirements. As shown in Table 2.5, the satellite instrument proposed In this thesis showed lower uncertainties of the retrieved total and tropospheric NO_2 SCDs without deterioration of the spectral resolution, compared with those of the other satellite instruments. This can be achieved using an extremely low satellite altitude of 300 km. In addition, I proposed the spectrometer specification optimized for NO_2 observation with a resolution of 1×1 km^2 and an F number of 2.6–5.3, leading to high SNRs as well as good measurement precision. These results have demonstrated the feasibility of the proposed spectrometer design, which will not only achieve a sufficiently high spatial resolution to identify and separate urban sources of NO_2 but also facilitate the determination of their emissions.

3 Validation analysis of SMILES acetonitrile (CH_3CN) observation comparing with Aura/MLS observation

3.1 introduction

Air pollution derived from biomass burning (BB) has been serious problem with climate change and population growth. BB events are important source of various trace gases and particles in the atmosphere (Eagan et al., 1974; Crutzen et al., 1979). The study of atmospheric gas species associated with BB is of significant because early estimation of pyrogenic emission suggested that some atmospheric pollutants of BB could be comparable to fossil fuel (Crutzen and Andreae, 1990; Seiler and Crutzen, 1980) and these emissions could significantly affect global atmosphere (Andreae, 1983).

Acetonitrile (CH_3CN) is a good tracer for BB as a dominant source of CH_3CN is wildfire (90–95 %) (Li et al., 2003). A mean lifetime in the atmosphere for CH_3CN is about 6.6 months assuming ocean uptake and reaction with hydroxyl radical (OH) radicals as the major sinks (Singh et al., 2003; de Gouw, 2003). Chemical loss of CH_3CN with OH especially occurs in the stratosphere while oceanic loss is dominant in the troposphere. In these respects about sources and sinks, hydrogen cyanide (HCN) is similar to CH_3CN and thus frequently compared together as an indicator of BB (Li et al., 2000, 2003). Arnold et al. (1978) first inferred the presence of stratospheric CH_3CN from the composition of positive ions using active chemical ionization mass spectrometry. Additionally, balloon-borne and airborne measurements for CH_3CN in the lower stratosphere have also been reported by Knop and Arnold (1987); Schneider et al. (1997).

The satellite observations of CH_3CN in the lower stratosphere have been performed using several satellite instruments, for example, Microwave Limb Sounder (MLS) onboard the UARS (Upper Atmosphere Research Satellite) (Barath et al., 1993), Atmospheric Chemistry Experiment Fourier Transform Spectrometer (ACE-FTS) onboard the Scisat-1 (Bernath, 2001), MLS onboard the Aura (Waters et al., 2006), and Superconducting Submillimeter-Wave Limb-Emission Sounder (SMILES) of JEM (Japanese Experiment Module) onboard the International Space Station (ISS) (Kikuchi et al., 2010). The previous works reported the volume mixing ratio (VMR) of CH_3CN mainly in the UTLS (Livesey et al., 2001, 2004; Harrison and Bernath, 2013). However there is only a few reports about the VMR of CH_3CN for lower stratosphere to mesosphere.

In this work, I derived vertical distribution of CH_3CN between lower stratosphere and mesosphere from SMILES observation and performed error analysis and validation analysis comparing with Aura/MLS observation data. The next section give the descriptions about SMILES CH_3CN observation and the quality control criteria. The validation analysis of SMILES CH_3CN observation using Aura/MLS observation is given in Section 3.3, followed by consideration for seasonal variation of SMILES CH_3CN (Section 3.4). Finally, I summarize the results of error analysis and validation analysis with Aura/MLS observation and conclude the availability of SMILES CH_3CN observation.

3.2 SMILES CH_3CN observation

The JEM/SMILES was operated from 12 October 2009 to 21 April 2010 on ISS (Kikuchi et al., 2010). The ISS has an inclination angle of 51.6° to the equator, which enables it to observe the

TABLE 3.1: SMILES characteristics

Parameter	Characteristics
Orbit	Non sun synchronous orbit
	∼91 min orbital period
Latitude coverage	38° S–65° N (nominal)
Integration time	0.47 sec
Number of data	1630 scan per day
Frequency range	624.32–625.52 GHz (Band-A)
	625.12–626.32 GHz (Band-B)
	649.12–650.32 GHz (Band-C)
Receiver system	SIS mixers and HEMT amplifiers†
Spectrometers	Acousto Optical Spectrometers
Frequency resolution	0.8 MHz
System noise temperature	∼350 K

† SIS:Superconductor–insulator–superconductor mixer;
HEMT: High electron mobility transistor

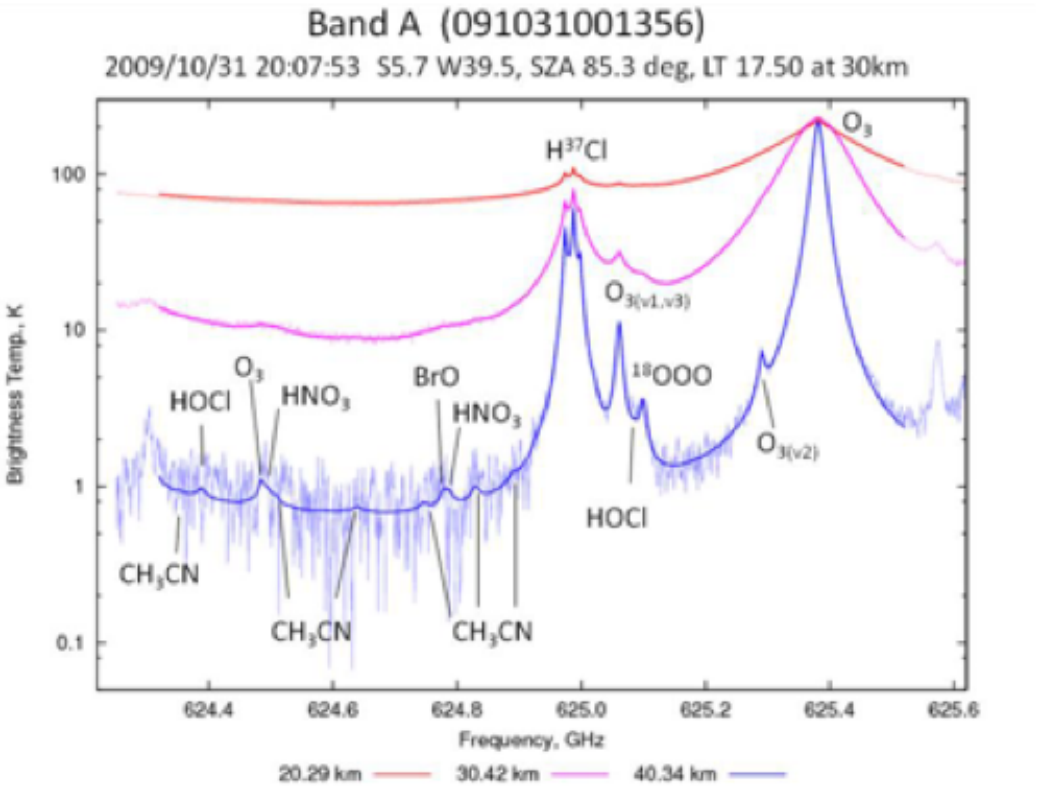

FIGURE 3.1: Samples of observed and fitted spectra (thin lines: observed, thick lines: fitted) in band A observed in 31 October 2009. This figure is referred from JEM/SMILES Level-2 Product Guide for v3.2 (118-12-0702) based on Suzuki et al. (2012).

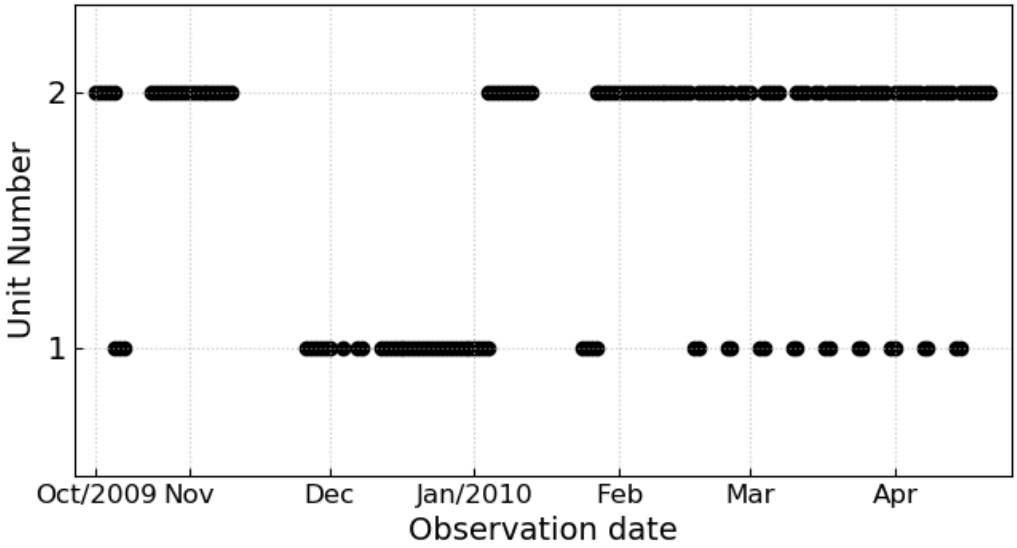

FIGURE 3.2: The distribution of AOS unit number for observation date.

atmosphere under various local solar times. The antenna field of view of SMILES instrument was set to point in a 45° direction leftward from the ISS orbital motion. Employing the four kelvin cooled submillimeter wave superconductive heterodyne receivers involved a low system noise temperature (T_{sys}) of $\sim$350 K (Ochiai et al., 2011).A summary of characteristics for SMILES observation is shown in Table 3.1.

The targeted CH_3CN transition at 624.82 GHz for (J, K) = (33, 3)–(33, 4) is allocated with a frequency region of Band-A (624.32–625.52 GHz) (See Figure 3.1). SMILES employed two Acousto Optical Spectrometers (AOSs) with a bandwidth of 1.2 GHz, which are denoted as AOS1 and AOS2 in this thesis. The date observed by AOS1 and AOS2 are shown in Figure 3.2.

The VMR profile of CH_3CN for SMILES version 3.0.0 (v3.0.0) was retrieved from measurement spectra solving inverse problem based on the least-squares method including a priori constraint (Rodgers, 2000). In this version of 3.0.0, AOS response function and a priori temperature profile used in the retrieval processing were improved. Detailed changes of this version can be found in JEM/SMILES Level 2 Research Data (L2r) Product Guide for Version 3.0.0. This version of Level-2 research (L2r) product are derived from Level-1b (L1b) version 008 calibrated spectra which employed the version 5.2 of the Goddard Earth Observing System Model (GEOS-5.2) as a priori information (e.g., O_3 VMR profile, temperature and pressure profile) (Rienecker et al., 2008). To retrieve CH_3CN VMR from SMILES measurement, inverse problem is solved using the optimal estimation method (Rodgers, 2000). The method leads to the maximum a posteriori solution, which minimizes the value of χ^2 described below. Detailed retrieval algorithm of L2r product can be found in Baron et al. (2011).

I determined the quality condition of retrieval product using two parameters, the chi-square statistics (χ^2) and measurement response ($\mathbf{m}$) defined as,

$$\chi^2 = [\mathbf{y} - \mathbf{F}(\mathbf{x}, \mathbf{b})]^T \mathbf{S}_y^{-1} [\mathbf{y} - \mathbf{F}(\mathbf{x}, \mathbf{b})] + [\mathbf{x}_a - \mathbf{x}]^T \mathbf{S}_a^{-1} [\mathbf{x}_a - \mathbf{x}] \tag{3.1}$$

$$\mathbf{m}[i] = \sum_j |\mathbf{A}[i, j]| \tag{3.2}$$

$$\mathbf{A} = \frac{\partial \hat{\mathbf{x}}}{\partial \mathbf{x}} = \mathbf{DK} \tag{3.3}$$

$$\mathbf{D} = \frac{\partial \hat{\mathbf{x}}}{\partial \mathbf{y}} = (\mathbf{K}^T \mathbf{S}_y^{-1} \mathbf{K} + \mathbf{S}_a^{-1})^{-1} \mathbf{K}^T \mathbf{S}_y^{-1} \tag{3.4}$$

$$\mathbf{K} = \frac{\partial \mathbf{y}}{\partial \mathbf{x}} \tag{3.5}$$

where $\mathbf{F}(\mathbf{x}, \mathbf{b})$ is the forward model depending on $\mathbf{x}$ state vector and on the known model parameters $\mathbf{b}$, $\mathbf{S}_y^{-1}$ the measurement covariance matrix, $\mathbf{x}_a$ the a priori state of $\mathbf{x}$, $\mathbf{S}_a$ the a priori covariance matrix, $\hat{\mathbf{x}}$ a solution of the retrieval, $\mathbf{A}$ the averaging kernel, $\mathbf{D}$ the contribution function, and $\mathbf{K}$ the weighting function. $\mathbf{m}$, $\mathbf{A}$ and $\mathbf{D}$ were derived from using $\mathbf{K}$ (Urban et al., 2004). Details on $\mathbf{m}$ are explained by Phillips et al. (2013). The χ^2 of CH_3CN for v3.0.0 was distributed almost in a range of 0.4–0.6. In case the measurement response is low values, retrieved information is contributed from the a priori state. Hence, in this thesis the data selection thresholds of χ^2 and measurement response were set to be $\chi^2 < 0.6$ and $\mathbf{m} > 0.80$, respectively. The data selection criteria was summarized in Table 3.3.

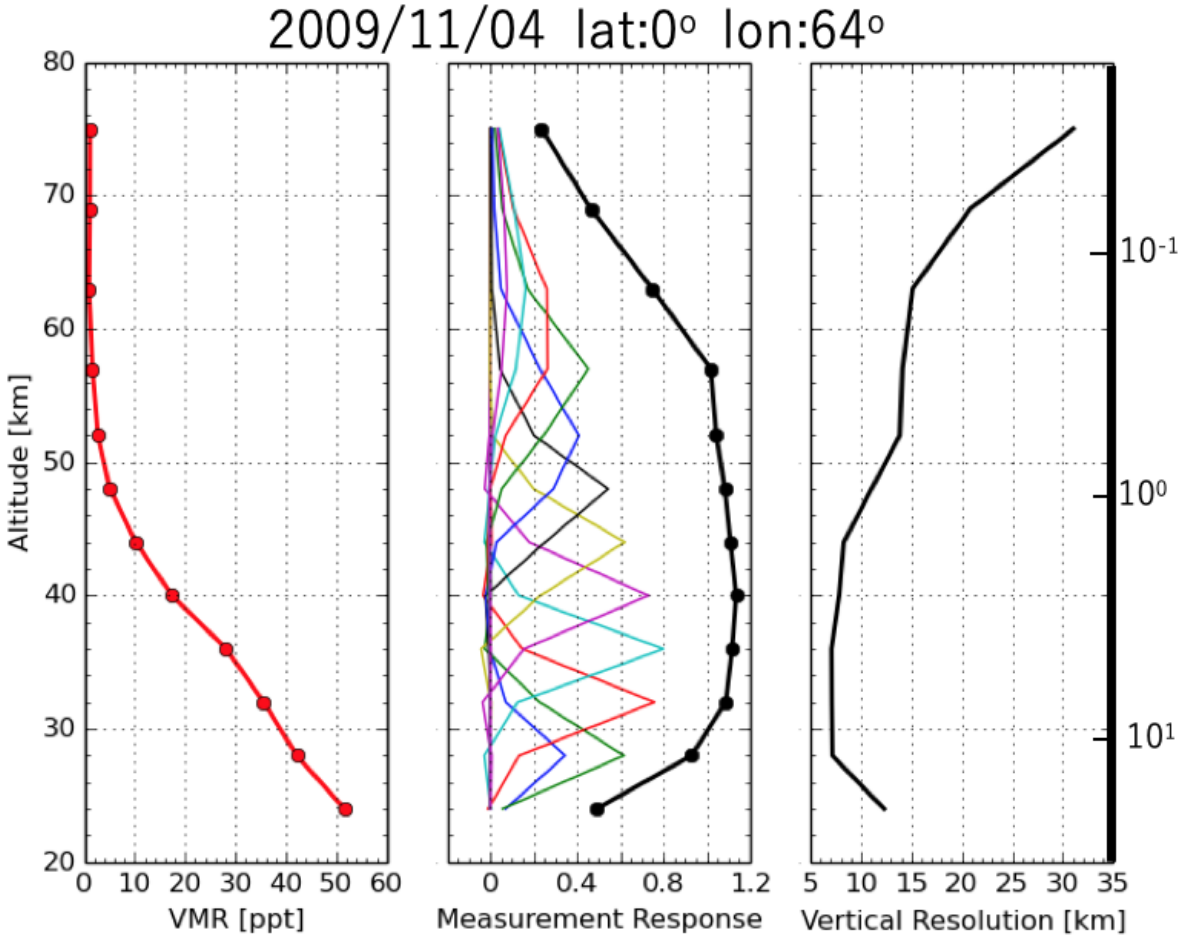

FIGURE 3.3: Left panel shows vertical profile of retrieved CH_3CN from single scan spectral from the observation of 4 November 2009 in tropic region. Middle panel shows averaging kernel of each measurement altitude (color line) and measurement response (solid black line). Right panel shows vertical resolution.

Fig. 3.3 shows an example of a retrieval result for a single scan spectrum which is from 4 November 2009 observation data in tropical region; retrieved CH_3CN vertical profile, averaging kernel and vertical resolution, respectively. The measurement response of retrieved CH_3CN, shown as black solid line in Fig.3.3 middle panel, is sum of elements of averaging kernel at each altitude. The measurement response was almost one from 30 to 55 km with a vertical

resolution being 7–15 km and decrease with altitude. The vertical resolution was defined as the full width at half maximum (FWHM) of each row of the averaging kernel matrix.

Fig. 3.4 shows (**a**) CH_3CN vertical profile observed by AOS1 and 2, (**b** and **c**) the absolute difference and the relative difference between AOS1 and AOS2 where measurement range is equatorial regions (20° S–20° N) in the period of March to April when observations by AOS1 and AOS2 were alternately conducted with a ratio of AOS1:AOS2=3:1. The errorbars shown in left panel of Fig. 3.4 indicate 1 sigma standard deviations of CH_3CN VMRs retrieved at SMILES pressure grids for AOS1 (blue) and AOS2 (green). These errorbars include measurement error (noise), smoothing error, and errors due to the uncertainties in the spectroscopic parameters. As can be seen, the relative difference between AOS1 and AOS2 is approximately 30 % at maximum at 15.7 hPa, indicating the difference between the two AOSs due to the difference of sensitivity. This difference was decreasing with altitude less than 10 % at 4.8 hPa.

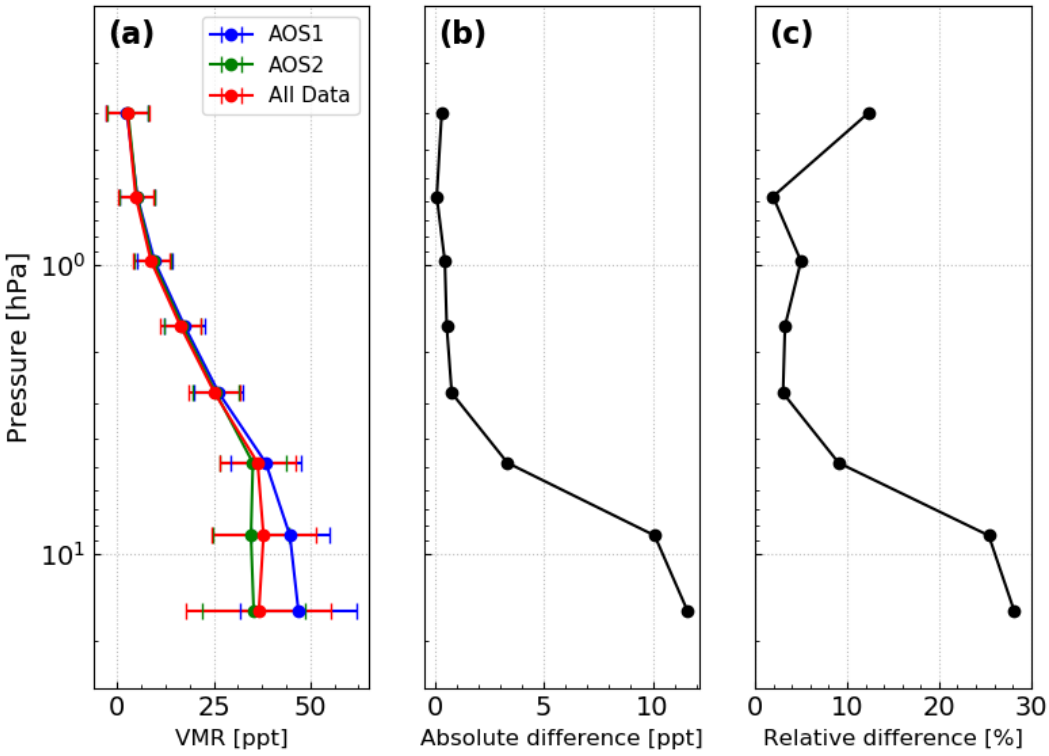

FIGURE 3.4: (**a**) Vertical profiles of CH_3CN from AOS1, AOS2 and sum of AOS1 and AOS2 in the equator region from 20°S to 20°N from March to April 2010. Each line indicates the averaged VMR from AOS1 observation (blue line), AOS2 (green line) and sum of AOS1 and AOS2 (red line). (**b**) The absolute difference between AOS1 and AOS2, i.e., $AOS1 - AOS2$. (**c**) The relative difference between AOS1 and AOS2, i.e., $(AOS1 - AOS2)/M$ when M is $(AOS1 + AOS2)/2$.

3.3 Validation of SMILES CH_3CN

3.3.1 Theoretical error analysis

Retrieval error consists of two components; (i) the spectrum statistical noise E_n and (ii) the smoothing error E_s described as follows, respectively,

$$\mathbf{S}_n = \mathbf{D}\,\mathbf{S}_y\mathbf{D}^T, \tag{3.6}$$

$$\mathbf{E}_n[i] = \sqrt{\mathbf{S}_n[i,i]}, \tag{3.7}$$

$$\mathbf{S}_s = (\mathbf{A}-\mathbf{U})\mathbf{S}_a(\mathbf{A}-\mathbf{U})^T, \tag{3.8}$$

$$\mathbf{E}_s[i] = \sqrt{\mathbf{S}_s[i,i]}, \tag{3.9}$$

where $\mathbf{S}_n$ and $\mathbf{S}_s$ are the error covariance matrices for the measurement noise and the errors from $\mathbf{S}_a$, respectively, and $\mathbf{U}$ is the unit matrix.

I estimated SMILES systematic error for VMR profile of CH_3CN by a single scan spectrum observed in 4th November 2009 in Tropic as same as Figure 3.3. I simulated the two different spectra which were derived original forward model, AMATERASU (Advanced Model for Atmospheric Terahertz Radiation Analysis and Simulation) (Baron et al., 2008), and perturbed forward model. In this thesis, I performed error analysis using the a priori of CH_3CN VMR in the equatorial region. The error sources and their perturbation parameters are summarized in Table 3.2.

Figure 3.5 shows the estimated systematic errors for the NICT v3.0.0 CH_3CN retrieval. Total systematic error, "Total" in Figure 3.5, was calculated as a root-sum-square (rss) of uncertainties of CH_3CN spectrum parameters and instrumental functions. The largest error source is air pressure broadening coefficient ("γ"), followed in order by line intensity ("Strength") and temperature dependence of air pressure broadening coefficient("n"). It is found from estimated systematic error that SMILES CH_3CN profile are influenced spectrum parameters.

TABLE 3.2: Error sources considered in this thesis. The name of the parameters and the labels used for their identification in the figures are given in the parenthesis in the first column.

Error source	Assumed uncertainty
Spectroscopic parameter of CH_3CN	
Line intensity (Strength)	1 %
Air pressure broadening (γ)	3 %
Temperature dependence of γ (n)	10 %
Impact from other species	
$H^{37}Cl$ air pressure broadening ($H^{37}Cl\gamma$)	3 %
Temperature dependence of H^{37} $Cl\gamma$ (H^{37} Cln)	10 %
O_3 air pressure broadening (O^3 γ)	3 %
O_3 temperature dependence of O^3 γ (O^3 n)	10 %
Instrumental functions	
AOS response function (AOS)	10 %
Antenna scan (Antenna)	2 %

In the Band-A, O_3 and $H^{37}Cl$ is observed in the same frequency bands as CH_3CN. The spectral shape of O_3 and $H^{37}Cl$ should influence that of CH_3CN spectrum. For this reason, I estimated impact of other species spectrum parameters perturbation as shown in Figure 3.5 **(b)**. In this work, I perturbated γ and temperature dependence of γ for each species, expressed as

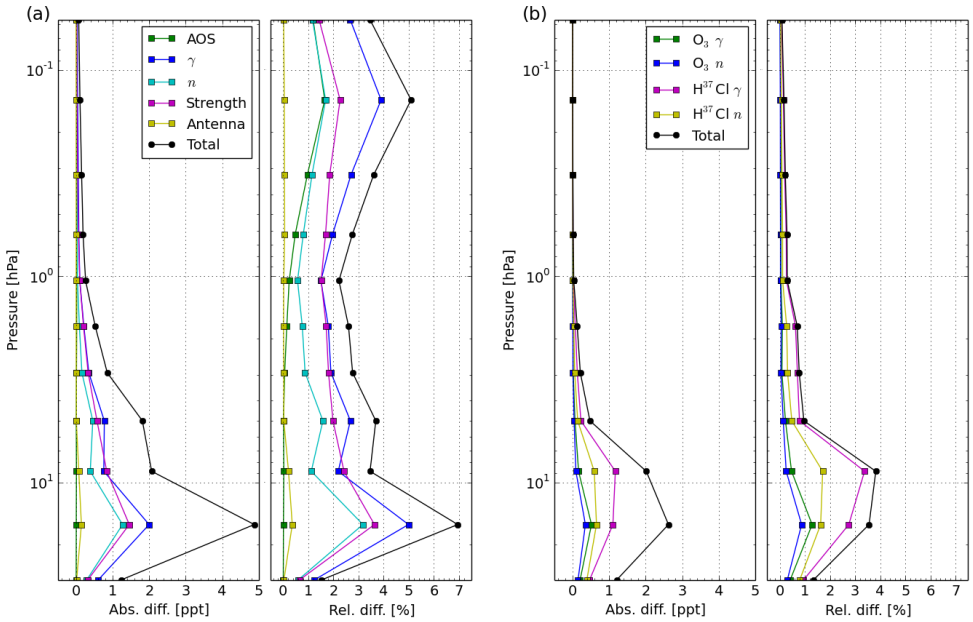

FIGURE 3.5: **(a)** Summary of absolute and relative differences derived from systematic errors of the CH_3CN retrieval due to the uncertainties of the spectrum parameters and **(b)** instrumental functions derived from single scan spectrum observed in 4 November 2009 in Tropic region as same as Figure 3.3. Black line in the middle panel indicates total error given by root-sum-square value of the assumed error sources.

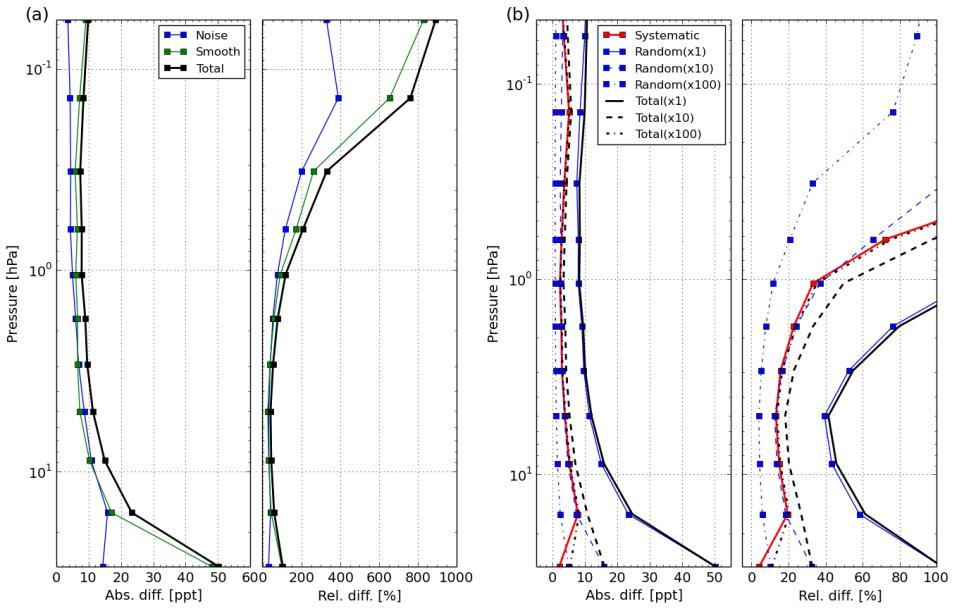

FIGURE 3.6: **(a)** Summary of absolute and relative differences derived from random errors of the retrieved CH_3CN of SMILES single scan observation as same as Figure 3.5. **(b)** Summary of absolute and relative differences derived from random (blue), systematic (red), and total (black) errors in the SMILES CH_3CN retrieval for averaging of N profiles (N = 1, 10,100). of SMILES accumulating several profiles. The number in the legend is accumulating profile number.

TABLE 3.3: Data quality criteria for SMILES and MLS

Data products	Quality threshold
SMILES v3.0.0	Measurement response > 0.80
	Goodness of fit (χ^2) < 0.6
	Field-of-view = 0
MLS v4.2	Quality > 1.40
	Convergence < 1.05
	Status = 0

"$O_3\gamma$", "O_3n", "$H^{37}Cl\gamma$" and "$H^{37}Cln$". "$H^{37}Cl\gamma$" is larger than "$O_3\gamma$" in the lower stratosphere, whose relative difference is 3.38 % and 0.47 %, respectively. Total error is 5.1–7.8 % in the lower stratosphere and 2.2–3.8 % in the upper stratosphere to lower mesosphere.

The measurement noise and smoothing error from a single scan are shown in the Figure 3.6 **(a)**. These errors can be considered as the random error of the CH_3CN profile. SMILES CH_3CN total error consists of the systematic and random error. Figure 3.6 **(b)** shows the total systematic error, the random and total error averaged by the number of profile (N = 1, 10 and 100). The random error is larger than the systematic error from a single scan although the random error averaged by 100 profiles was comparable to the systematic error except for the peak of the systematic error existing at a pressure level of about 1 hPa.

3.3.2 Comparison with Aura/MLS v4.2 data

Methodology of comparisons

I investigated the difference of CH_3CN VMR between SMILES and MLS of measurement CH_3CN VMR. Therefore, I set the data quality and the coincidence selection criteria. Table 3.3 gives the data quality selection criteria for the SMILES and MLS datasets. The MLS data quality criteria were based on MLS v4.2 Level-2 data quality and description document (2016). The geolocation and measurement time criteria were determined as follows;

- the distance of measurement location within 300 km;
- difference in the measurement time within 1 hour.

Figure 3.7 shows the distribution of coincident points satisfied these criteria at 8.6 hPa.The interpolation of VMRs was done by using a linear interpolation with respect to the logarithm of the pressure levels. There are on average 10 coincident points in one grid at this pressure level and the total coincident data number was 3257.

In the comparison between SMILES and MLS observations, the mean absolute difference, Δ_{abs} , and relative difference, Δ_{rel}, at the pressure levels, p , between coincident CH_3CN profiles of the two observations were calculated as follows,

$$\Delta_{abs} = \frac{1}{N(p)} \sum_{i=1}^{N(p)} \{x_s(p) - x_m(p)\}, \tag{3.10}$$

$$\Delta_{rel} = \frac{1}{N(p)} \sum_{i=1}^{N(p)} \frac{\{x_s(p) - x_m(p)\}}{\overline{x}_(p)} \times 100, \tag{3.11}$$

where $N(p)$ is the number of coincidences at p, $x_s(p)$ and $x_m(p)$ are the VMRs at p for SMILES and MLS observations, and the reference ($\overline{x}_p$) is $\overline{x}_p = \frac{1}{2}(x_s(p) + x_m(p))$.

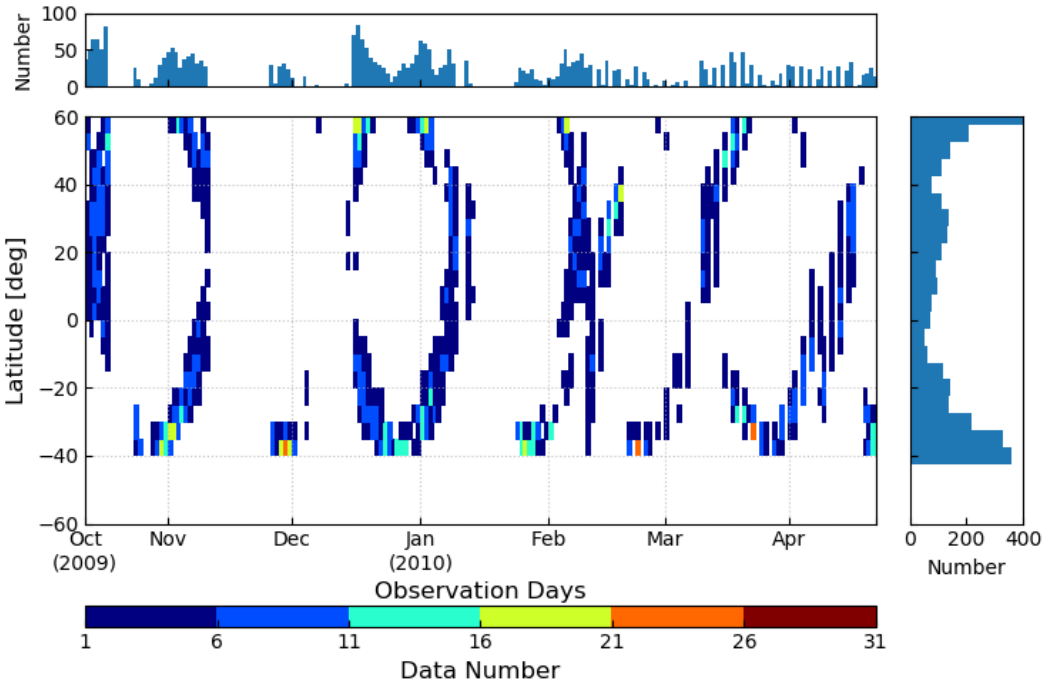

FIGURE 3.7: Distribution of the data number satisfied criteria in the time period between 12 October 2009 and 21 April 2010 in the measurement latitude range at 8.6 hPa. Observation date and latitude bins are 1 day and 3°.

Aura/MLS v4.2

The microwave Limb Sounder (MLS) instrument onboard the Aura satellite which has been operated since 2004 observed CH_3CN from lower to upper stratosphere. This satellite was launched sun-synchronous orbit with an equator-crossing time 13:45 (ascending) and 01:45 (descending). The daily MLS measurement gives 82° S to 82° N latitude coverage. MLS instrument measures temperature and trace gases (O_3, CO, H_2O, HNO_3, CH_3CN etc.) using thermal emission data from atmosphere. The CH_3CN VMR was retrieved from the MLS observation data using the optimal estimation method. Details on the retrieval algorithm was described in Livesey et al. (2006). The MLS uses spectral bands of 118, 190, 240 and 640 GHz and 2.5 THz, observing CH_3CN from 640 GHz spectral regions (Waters et al., 2006). MLS Level-2 CH_3CN profile was observed in 640 GHz spectral regions. Although the pressure range of a retrieved MLS CH_3CN is 147 to 0.001 hPa, scientific using pressure range of version 4.2.0 CH_3CN product is 46–1.0 hPa (Livesey et al., 2006).

Result of comparisons

Fig. 3.8 shows the vertical profile, the absolute differences and the relative differences between SMILES and MLS CH_3CN. Left panel in Fig. 3.8 indicates good agreement from 15.7 hPa to 2.8 hPa between the two observations. In the range of pressure levels, the absolute difference and the relative difference between SMILES and MLS observation were -20–5 ppt and 20–100 %, respectively. The difference between SMILES and MLS becomes larger with altitude from a pressure level of 8.6 hPa. Overall, the variance of SMILES is smaller than MLS because SMILES T_{sys} was much smaller than that of MLS, indicating that SMILES has an advantage in upper

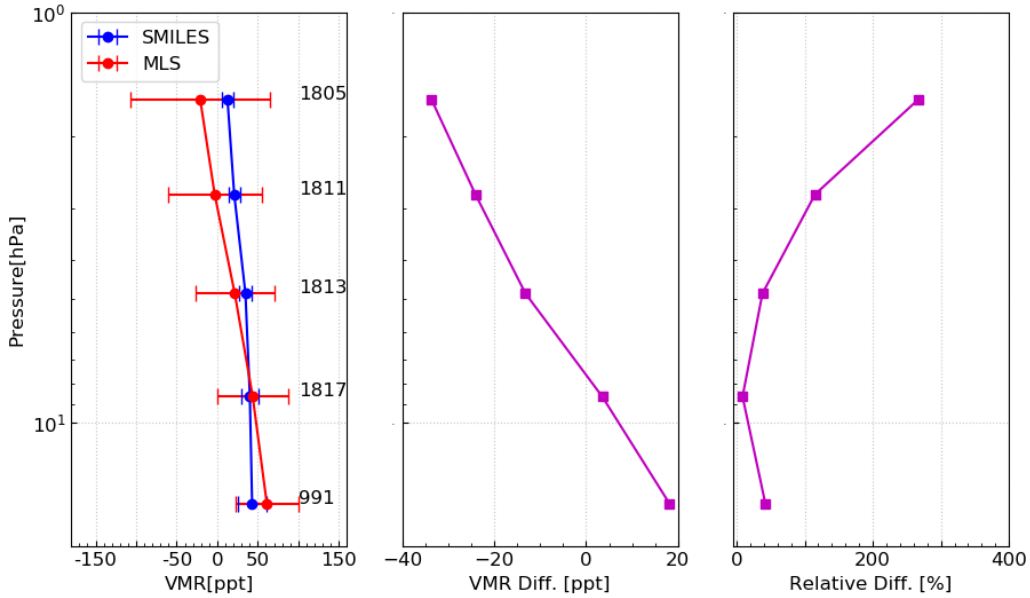

FIGURE 3.8: Left panel: Mean CH_3CN VMR values for SMILES and MLS measurement (blue line is SMILES and red line is MLS). Error bar indicates 1σ standard deviation for each dataset. Number of coincident data are displayed at each point. Middle panel: mean absolute difference for observed CH_3CN between SMILES and MLS calculated by Eq.3.10. Right panel: relative difference for observed CH_3CN between SMILES and MLS calculated by Eq.3.11

stratosphere and first observed CH_3CN VMR in the altitude with much lower uncertainty of $\sim$20 ppt.

I investigated more detail of relationships between SMILES and MLS observation for latitudinal and seasonal variation. Figure 3.9 shows the seasonal variations of SMILES and MLS CH_3CN observations and the absolute differences for each pressure level at coincident points as a function of latitudes. Left column represents SMILES CH_3CN VMR in units of ppt which were separated into two AOSs observations. Middle column represents MLS CH_3CN VMR and right column represents the absolute differences between SMILES and MLS, that is $SMILES - MLS$. In the lower altitudes of 15.7 hPa and 8.6 hPa, SMILES observation was overestimated by MLS observation while in upper one (4.8 hPa$\sim$) it was underestimated up to 40 ppt. This result was consistent with a result of VMR comparison (see Figure 3.8). At higher altitudes, the number of coincident points for MLS observation was significantly decreased, indicating that at upper stratosphere the uncertainty of MLS observation was large.

3.4 Traceability of CH_3CN for biomass burning

To validate a traceability of SMILES CH_3CN for biomass burning, I compared SMILES data with Aura/MLS HCN data and GFED version 4 (Global Fire Emissions Database) data (Randerson et al., 2017). As mentioned before, HCN is used as a tracer for biomass burning (Li et al., 2009). Pumphrey et al. (2011) reported the enhancement of biomass burning product including HCN observed by Aura/MLS in February 2009 when the large Australian bush fires occurred. Therefore, it should be expected that the good correlation between SMILES CH_3CN and Aura/MLS HCN data is obtained as CH_3CN is also a tracer for biomass burning.

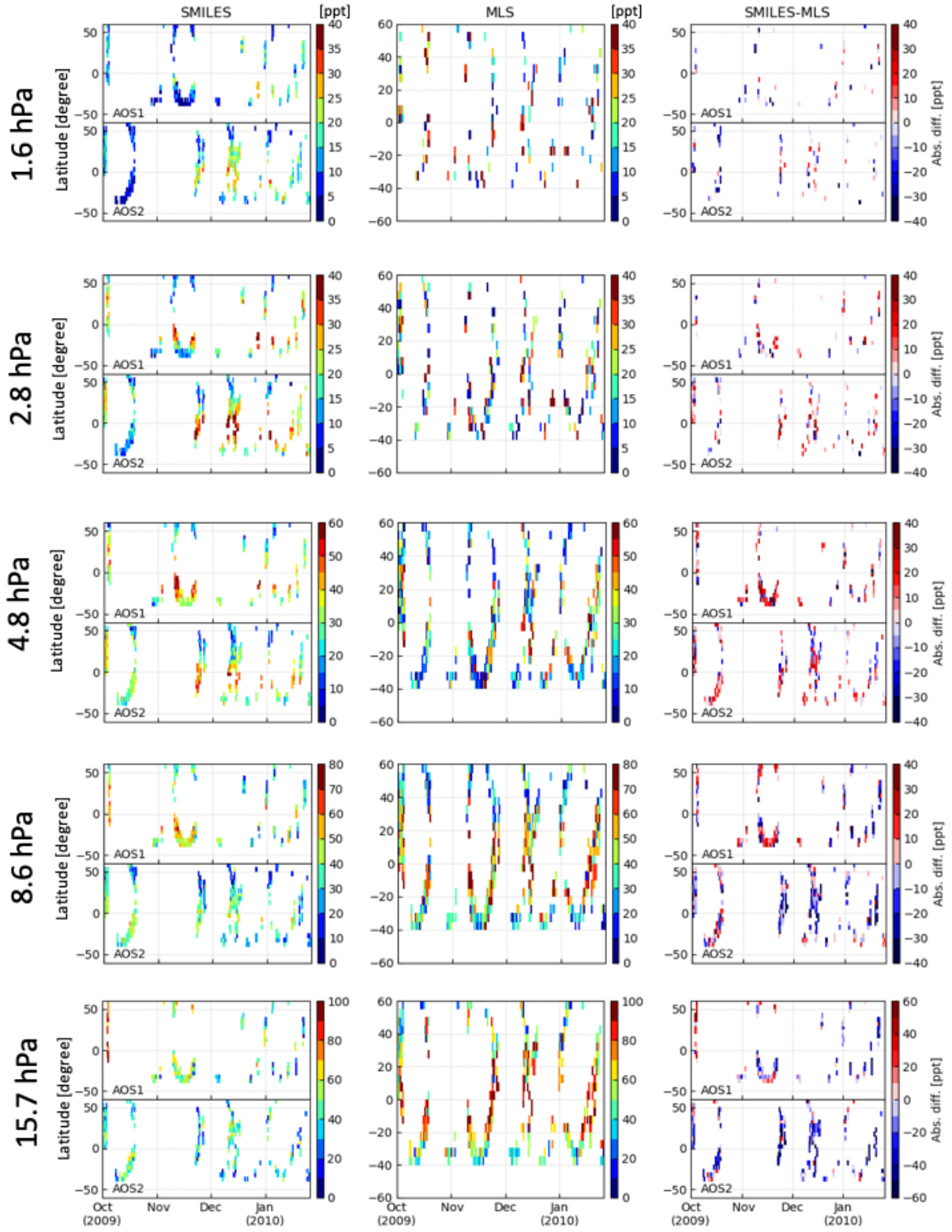

FIGURE 3.9: Seasonal variations of SMILES and MLS CH_3CN observations and the absolute differences for each pressure level as a function of latitudes. The data were binned to 1-day and 5° grid.

TABLE 3.4: Summary of correlation coefficient between SMILES CH_3CN and MLS HCN.

Altitude [km]	Correlation coefficient
28 (15.7 hPa)	0.26
32 (8.6 hPa)	0.66
36 (4.8 hPa)	0.89
40 (2.8 hPa)	0.92
44 (1.6 hPa)	0.89
48 (0.97 hPa)	0.83
52 (0.58 hPa)	0.73
57 (0.30 hPa)	0.46

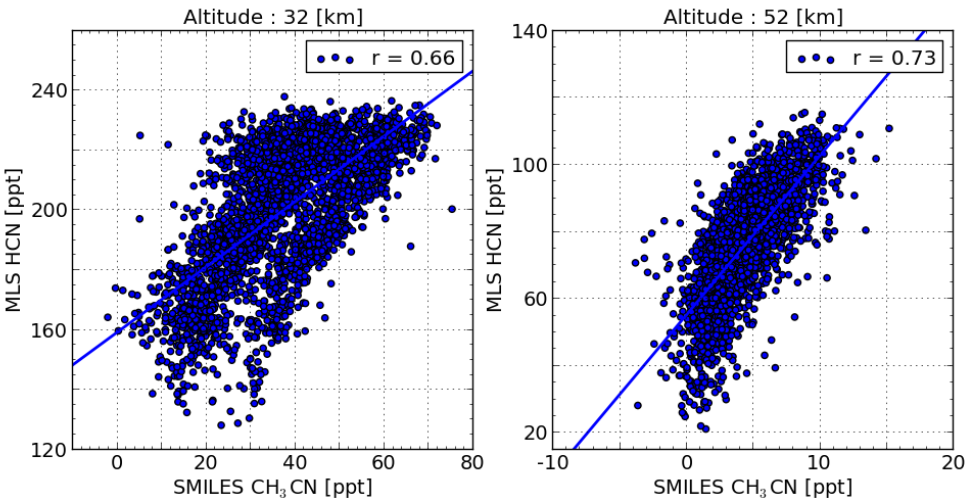

FIGURE 3.10: Scatterplot of CH_3CN profile from SMILES and HCN profile from MLS. Time and latitude bins are one day and 5° -wide latitude range. (a): altitude is 32km. (b): altitude is 52 km

I calculated correlation using MLS version 4.2.0 HCN data satisfied data quality condition . Figure 3.10 shows SMILES CH_3CN vs. HCN scatterplots; the data are binned into 5 ° latitude bins as well as one day bins There are positive correlation between SMILES CH_3CN and MLS HCN from lower stratosphere to upper stratosphere, each correlation coefficient are 0.66 and 0.73 although at lowermost and uppermost pressure height they decreased to 0.26 and 0.46, respectively, as summarized in Table 3.4. This finding suggests that the relationship between CH_3CN and HCN shows a good linearity and that CH_3CN should be traceable for biomass burning.

Next, I investigate the relationship between SMILES CH_3CN and GFED data to demonstrate that CH_3CN emission is associated with a biomass burning event. Figure 3.11 shows (*left*) the basis regions defined in GFED v4 to divide continents into 14 regions based on the fire sources and trace gas emissions and (*right*) the regions re-classified into large three parts in this study based on those latitudes and sources. Abbreviations for the regions were explained in the caption of Figure 3.11 and used without any annotations hereafter. The regions re-classified in this thesis is hereafter called as the Northern-hemispheric (NH) region for the blue-colored area, the equatorial (EQ) region for the red-colored area, and the Southern-hemispheric (SH) region for the green-colored area, respectively, consisting of 4–5 parts defined in GFED document in each region.

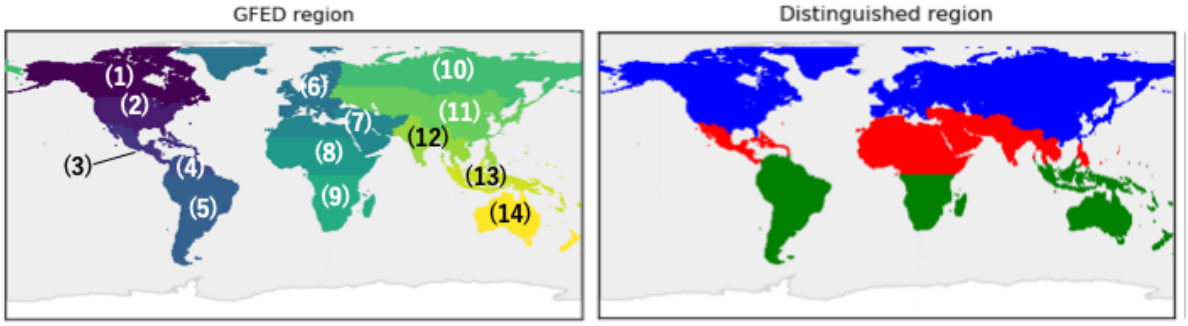

FIGURE 3.11: Left panel shows the regions defined in the GFED v4 products; (1) BONA (Boreal North America), (2) TENA (Temperate North America), (3) CEAM (Central America), (4) NHSA (Northern Hemisphere South America), (5) SHSA (Southern Hemisphere South America), (6) EURO (Europe), (7) MIDE (Middle East), (8) NHAF (Northern Hemisphere Africa), (9) SHAF (Southern Hemisphere Africa), (10) BOAS (Boreal Asia), (11) CEAS (Central Asia), (12) SEAS (Southeast Asia), (13) EQAS (Equatorial Asia), and (14) AUST (Australia and New Zealand), respectively. Right panel shows the regions distinguished in this thesis; blue color includes (1) BONA, (2) TENA, (6) EURO, (10) BOAS, and (11) CEAS; red color includes (3) CEAM, (7) MIDE, (8) NHAF, and (12) SEAS; green color includes (4) NHSA, (5) SHSA, (9) SHAF, (13) EQAS, and (14) AUST. These regions were separated based on those latitudes and the dominated emission sources.

Figure 3.12 shows vertical profiles of CH_3CN observed by SMILES in the periods of October to November (**a**), December to February (**b**), and March to April (**c**), respectively, which were identified in each basis region defined in the GFED document. The different colors and symbols represent different GFED regions displayed in Figure 3.11. Overall, CH_3CN VMR values were highest at lowermost altitude (= about 24 km) in most cases and reduce with altitudes in all regions except the SH region in Dec–Feb and Mar–Apr, resulting from vertical convection and no CH_3CN sources in the stratosphere although in mid-latitude vertical convection generally is less than that in the tropics and CH_3CN source is dominant in the troposphere. In Figure 3.12 (**a**), EQ and SH regions were comparable and CH_3CN VMR in some parts of NH

regions were relatively higher at middle altitudes from 4.8 hPa to 2.8 hPa. As shown in Figure 3.12 (**b** and **c**), the classification in three parts is consistent showing the obvious differences of vertical distribution pattern. It should be notable that there are maximum values at around 6 hPa in SH region except Oct–Nov although VMRs at lowermost altitude were comparable between EQ and SH regions. Figure 3.13 shows that carbon emission and burned fraction in each period derived from GFED v4 products. As can be seen, burned fraction and carbon emission in the tropic region ($< \pm 30\,^{\circ}$) including CEAM, SEAS, NHAF, AUST, EQAS, and NHSA were dominant in all periods, which are consistent with the CH_3CN VMRs distribution shown in Figure 3.12. Although large emission and burned fraction in mid-latitude northern hemisphere can be seen in the periods of Oct–Nov and Mar–Apr in BOAS and CEAS region, CH_3CN VMR in BOAS (blue triangle) and CEAS (blue plus) region in the periods were comparable to those in Dec–Feb with 30–40 ppt of CH_3CN at the lowermost altitude. This indicates that the source of stratospheric CH_3CN in mid-latitude area should be a transport from the tropic region rather than vertical convection from the local biomass burning. On the other hand, VMR at lowermost altitude in the NH region sometimes was comparable to those in the other two regions and thus vertical convection of biomass burning plume can be considerable with the horizontal transport.

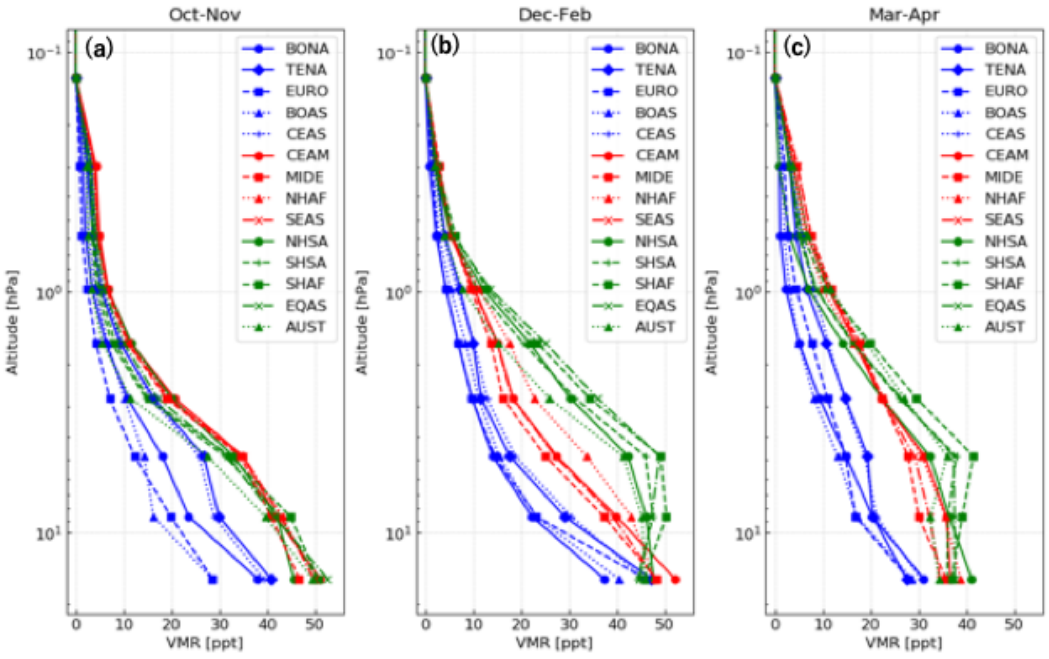

FIGURE 3.12: Vertical profiles of CH_3CN observed from SMILES in the periods of (**a**) October to November, (**b**) December to February, and (**c**) March to April, respectively, which coincide with each basis region defined in the GFED document. The differences of the colors and symbols indicate different GFED regions displayed in Figure 3.11.

3.5 Conclusions of this chapter

I performed data validation of SMILES and derived the vertical profile and seasonal variation in the upper atmosphere using SMILES data. The CH_3CN data quality of SMILES is investigated by error analysis and comparison with Aura/MLS. Error analysis shows systematic error is dominant uncertainty spectral parameters in the measurement altitude range. In the lower stratosphere, the uncertainty of air pressure broadening effects approximately 7.0 %. The

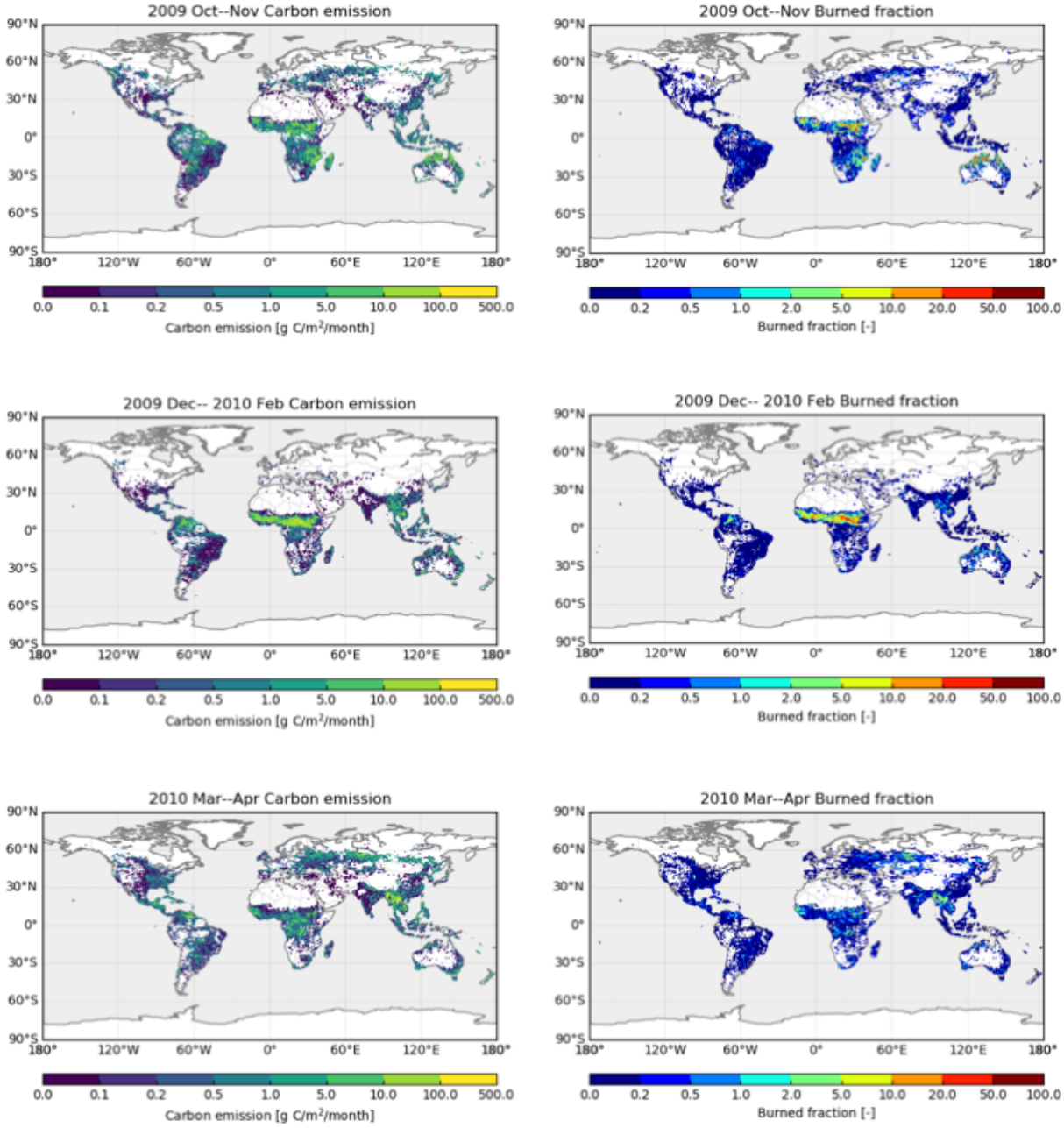

FIGURE 3.13: Left column shows biomass burning carbon emissions and right column shows the burned fraction of each grid cell in each period; October to November 2009, December 2009 to February 2010, and March to April 2010. Units of carbon emissions in g C/m^2/month.

random error from single scan spectra is larger than systematic error, but the random error decreases with the profile number.

Comparison with Aura/MLS shows there are good agreement lower stratosphere and also no specific latitudinal and seasonal dependence between SMILES an MLS. The difference between SMILES and MLS increase with altitude.

The systematic error and the relative difference to MLS are 3.78–5.09 % and 24.7–35.5 % in the altitude range between 8.6 and 4.8 hPa (32–36km). Therefore, SMILES CH_3CN profile has the reliability in the altitude range between 8.6 and 4.8 hPa (32–36km). Above 36 km, SMILES CH_3CN precision is good value but relative difference to MLS is over 100 %.

I derived correlation coefficient between SMILES CH_3CN and Aura/MLS HCN both of which are known as a biomass burning tracer. There is a strong correlation coefficient (0.66–0.92 at pressure level of 8.6 hPa–0.58 hPa) between lower stratosphere and upper stratosphere.

4 Conclusions and future perspectives

Although NO_2 has various natural and antoropogenic emission sources, remote sensing of NO_2 from space using satellite instruments has an advantage for global observation. My focuses are to detect NO_2 hotspots and to identify NO_2 sources in the region where several emission sources exist. In order to achieve these two concepts, I performed error analyses for NO_2 observation with 1 km spatial resolution and for SMILES CH_3CN observation as a biomass burning tracer to distinguish natural and anthropogenic contribution. Based on the simulation analysis for NO_2 and the validation analysis for SMILES CH_3CN, I understood how NO_2 observation with km-order resolution can be achieved in the future and whether CH_3CN is valid as an indicator for biomass burning using SMILES satellite measurement.

The lower satellite altitude of 300 km was determined to be optimum to meet the scientific requirement of 5% for the tropospheric NO_2 SCD because measurement error in the polluted region (Beijing) met the scientific requirement of 5% at an SNR of around 1000 with a precision of 2%–4% for all the fit windows in the case of a satellite altitude of 300 km, while a satellite altitude of 600 km did not meet the requirements in the same situation. In the moderately polluted case, however, use of the 405–465 nm window may be suitable because lower measurement errors are achieved compared to use of the 425–497 nm window, although it still did not satisfy the requirements. Therefore, a combination of a fit window of 425–497 nm and a satellite altitude of 300 km is likely to be the optimal combination for the satellite instrument considered in this study. The error estimation analysis considering the error propagation, including the AMF uncertainty, implied that the overall error for the tropospheric NO_2 retrieval was expected to be 0.88×10^{15} molec cm^{-2}, which is consistent with the scientific requirements. As shown in Table 2.5, the satellite instrument proposed in this study showed lower uncertainties of the retrieved total and tropospheric NO_2 SCDs without deterioration of the spectral resolution, compared with those of the other satellite instruments. This can be achieved using an extremely low satellite altitude of 300 km.

Comparison with Aura/MLS shows there are in good agreement in lower stratosphere and also no specific latitudinal and seasonal dependence between SMILES an MLS. The difference between SMILES and MLS increase with altitude. The systematic error and the relative difference to MLS are 3.78–5.09 % and 24.7–35.5 % in the altitude range between 8.6 and 4.8 hPa (32–36km). Therefore, SMILES CH_3CN profile has the reliability in the altitude range between 8.6 and 4.8 hPa (32–36km). I derived correlation coefficient between SMILES CH_3CN and Aura/MLS HCN both of which are known as a biomass burning tracer. There is a strong correlation coefficient (0.66–0.92 at pressure level of 8.6 hPa–0.58 hPa) between lower stratosphere and upper stratosphere except lowermost and uppermost pressure altitudes. Based on comparison analysis with GFED v4 data, NO_2 emissions in SHSA, NHAF, a part of AUST and most part of SHAF regions were estimated to originate from biomass burning, can be seen in the periods of Oct–Nov and Dec–Feb and this fact is consistent with SMILES CH_3CN VMR distinguished in each region.

In this thesis, I determined the optimum setup for NO_2 observation with 1 km spatial resolution, which could be a breakthrough in terms of spatial resolution. Small satellite and super low altitude of 300 km are key concepts supporting such high spatial resolution. Such super low satellite altitude is also needed to improve the sensitivity to atmospheric trace gases although it is obvious that technical advance of the detector improve the spatial resolution of previous satellite instruments. Based on test results of the SLATS, super low altitude less than

300 km would be focused and utilized for air quality observation because this altitude is state-of-the-art. I believe that this thesis could be helpful for the situation as a pioneer and a foothold to switch to $\sim$1 km.

For CH_3CN, its relatively long lifetime and near exclusive emission from biomass burning suggest the great potential as a biomass burning tracer (Akagi et al., 2011). This thesis quantitatively demonstrated a reliability of CH_3CN VMR data in stratosphere derived from SMILES measurement. Also, the availability of SMILES CH_3CN data as a biomass burning tracer was shown though it is qualitative. To evaluate its traceability quantitatively using satellite measurements, simulations for vertical convection and horizontal transport would be considered for further steps.

A Differences between AOS1 and AOS2

Figure A.1 shows histgrams of SMILES CH_3CN VMRs observed by AOS1 and AOS2 at 15.7, 8.6, 4.8, 2.8, 1.6, 0.97, 0.58, and 0.30 hPa, respectively, using data displayed in Figure 3.4. As can be seen, differences of mean value between AOS1 and AOS2 decreased with altitudes although even at 15.7 hPa, where the difference between AOS1 and AOS2 was largest, mean values for AOS1 and AOS2 were in 1σ standard deviation of each other, implying that the difference between AOS1 and AOS2 (about 10 ppt) was not significant.

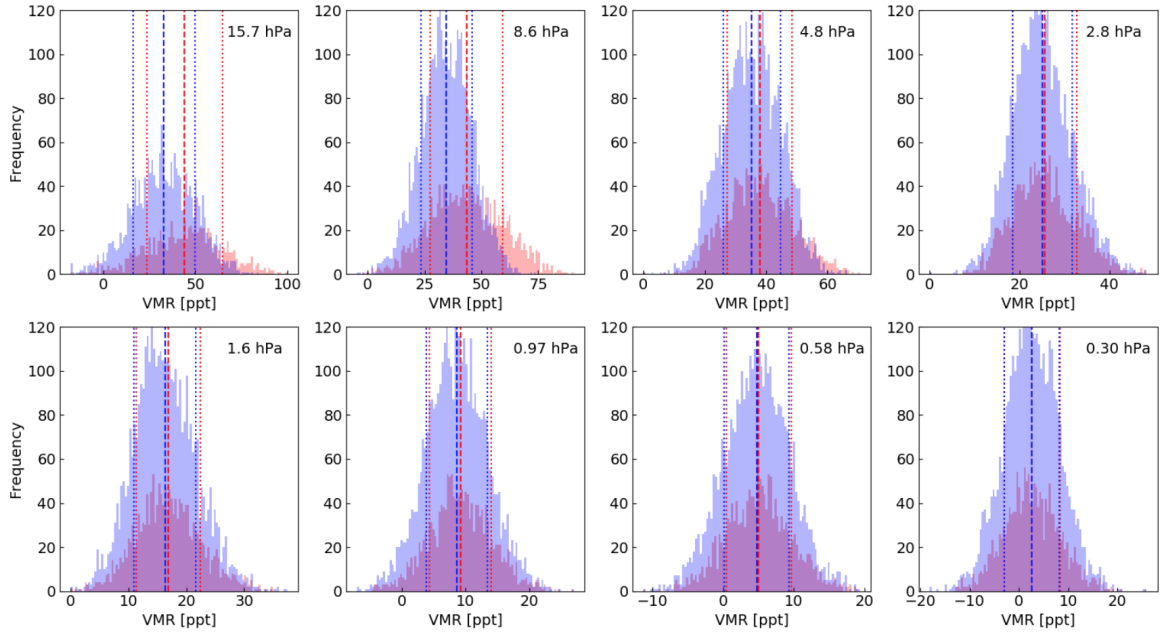

FIGURE A.1: Histgrams of SMILES CH_3CN VMRs observed by AOS1 (red) and AOS2 (blue) at 15.7, 8.6, 4.8, 2.8, 1.6, 0.97, 0.58, and 0.30 hPa, respectively. Vertical broken lines and dotted lines indicate each mean value and 1σ standard deviation for each histgram, respectively.

B Consideration for seasonal variation

I derived a daily scatter and average plots for SMILES CH_3CN VMR at altitudes of 28–52 km (corresponding to 15.7–0.58 hPa) to investigate the seasonality because of sparse observation dates of SMILES measurements. Only the date when more than one hundred data were obtained in one day was considered. As can be seen in Figure B.1, at pressure levels of 32–44 km, the 1σ standard deviation of SMILES CH_3CN VMRs in the period of Dec–Feb were slightly larger than those in the other periods even if comparing with the periods when the same AOS were observing. I believe this would be due to differences of the vegetation from which CH_3CN emitted in this period. Even if this effect and the uncertainties of CH_3CN are considered, seasonality of CH_3CN which CH_3CN is slightly high in February can be seen at pressure levels of 40–44 km, which is due to seasonality of biomass burning.

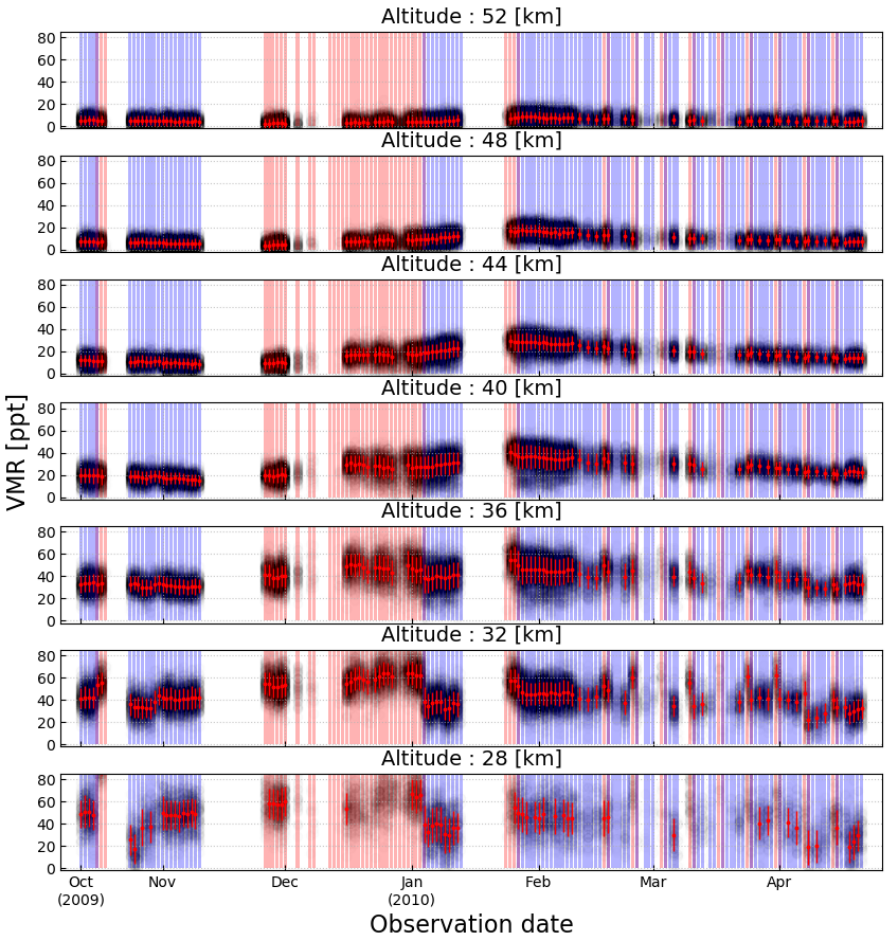

FIGURE B.1: Daily scatter and average plots for retrieved CH_3CN at each altitude (28–52 km) in the Equatorial region (20°S–20°N). Solid red lines indicate filtered mean values. Error bar indicates 1σ standard deviation of moving average. Red (blue) shaded areas represent the date observed by AOS1 (AOS2).

C Monthly scattering plots of SMILES CH_3CN vs. Aura/MLS HCN

I derived seasonal (Oct–Nov, Dec–Feb and Mar–Apr) and monthly (December, January and February) scattering plot of SMILES CH_3CN vs. Aura/MLS HCN at 32 km. The distribution derived in Dec–Feb (red) were obviously different from those derived in the other two periods (green and blue) (see upper left panel in Figure C.1), which showed the distribution taking the other two trends. The VMRs of SMILES CH_3CN in December were relatively higher (about 20 ppt) than those in January and February when comparing with the same VMR value of Aura/MLS HCN, i.e., at 160 ppt of Aura/MLS HCN SMILES CH_3CN VMRs were 30–40 ppt in December but 15–20 ppt in February. Also, scattering derived in January showed the intermediate of these two different trends. The enhancements of carbon emission and burned fraction derived from GFED data also implied the enhancement of biomass burning event in December, especially in Sahel. At this altitude (32 km = 15.7 hPa), differences between AOS1 and AOS2 is relatively large (see Figure B.1 and Figure A.1). Additionally, the spectrometer observing in December was only the AOS1. Therefore, the distribution derived in Dec–Feb was likely to have two trends.

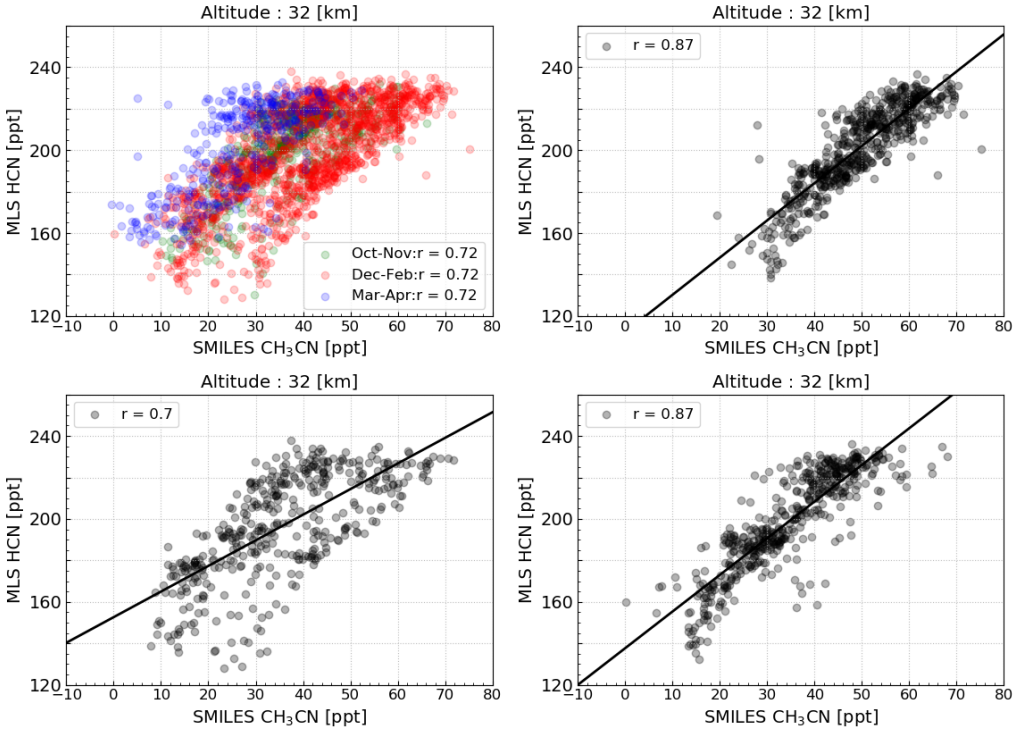

FIGURE C.1: (*upper left*) Seasonal scattering plot of SMILES CH_3CN vs. Aura/MLS HCN at 32 km. Red, blue and green color represent data from the periods of Dec–Feb, Mar–Apr and Oct–Nov, respectively. Solid line represents the regression curve derived in all periods. (*lower left and right column*) Monthly scattering plots in the period of Dec–Feb at 32 km. solid lines in each panel show the regression curves derived in each month.

D Comparison of OMNO2 data with GFED data

Figure D.1 shows the distribution map of retrieved NO_2 VCDs in troposphere (VCD_{trop}) ((**a**), (**d**), and (**g**)), stratosphere (VCD_{strat}) ((**b**), (**e**), and (**h**)), and total (= VCD_{trop} + VCD_{strat}) ((**c**), (**f**), and (**j**)), respectively. These VCDs were averaged in each period using 0.25° gridded OMI standard products (OMNO2G) (Krotkov, 2012, Accessed: 8 April 2019) in the period of SMILES observation. As mentioned in introduction, one of natural source of NO_2 is biomass burning. Therefore biomass burning emission can be estimated from the NO_2 VCD observed by satellite instruments although it is slightly hard to identify the NO_2 source due to mixing NO_2 from the various sources in an urbanized area. van der A. et al. (2008) reported the map of dominant NO_x (=NO_2) sources based on analyses of the time series of satellite NO_2 observations such as GOME and SCIAMACHY at 10 a.m. (Figure 1.3). Based on this analysis, NO_2 emissions in SHSA, NHAF, a part of AUST and most part of SHAF regions were estimated to originate from biomass burning, can be seen in the periods of Oct–Nov and Dec–Feb in Figure 3.13. This results showed a good consistency between OMNO2G data and GFED data. As can be seen in Figure D.1, tropospheric NO_2 (VCD_{trop}) was enhanced in the regions above, where biomass burning event is concentrated.

The stratospheric NO_2 (VCD_{strat}) in near equatorial region is as relatively high as 2.5–3.0 $\times$ 10^{15} molec cm^{-2} with slight enhancements of NO_2 emissions from biomass burning. On the other hand, in case of Mar–Apr the distribution was totally different from the other two periods, which shows high NO_2 VCDs of about 3.0 $\times$ 10^{15} molec cm^{-2} or more in mid-latitude northern hemisphere due to the daytime hours.

According to van der A. et al. (2008), the distinction between NO_2 from anthropogenic sources and from biomass burning is determined by the month of maximum NO_2 and biomass burning mainly contributes to NO_2 emission from the winter to spring (January–April in Northern hemisphere). Also, they reported that in the undefined area in India and Southeast Asia a month of maximum NO_2 is March which is in good agreement with GFED data because of enhancement of carbon emission and burned fraction (see Figure 3.13) although NO_2 VCD_{trop} shows almost same value in all periods in Figure D.1. In the regions of SHSA, NHAF, a part of AUST and most part of SHAF, where are mostly in Southern hemisphere, Month of maximum should be July–October. Therefore, NO_2 VCD_{trop} in Oct–Nov is slightly higher in the regions above and this result seems to be consistent with SMILES CH_3CN VMR distinguished in each region.

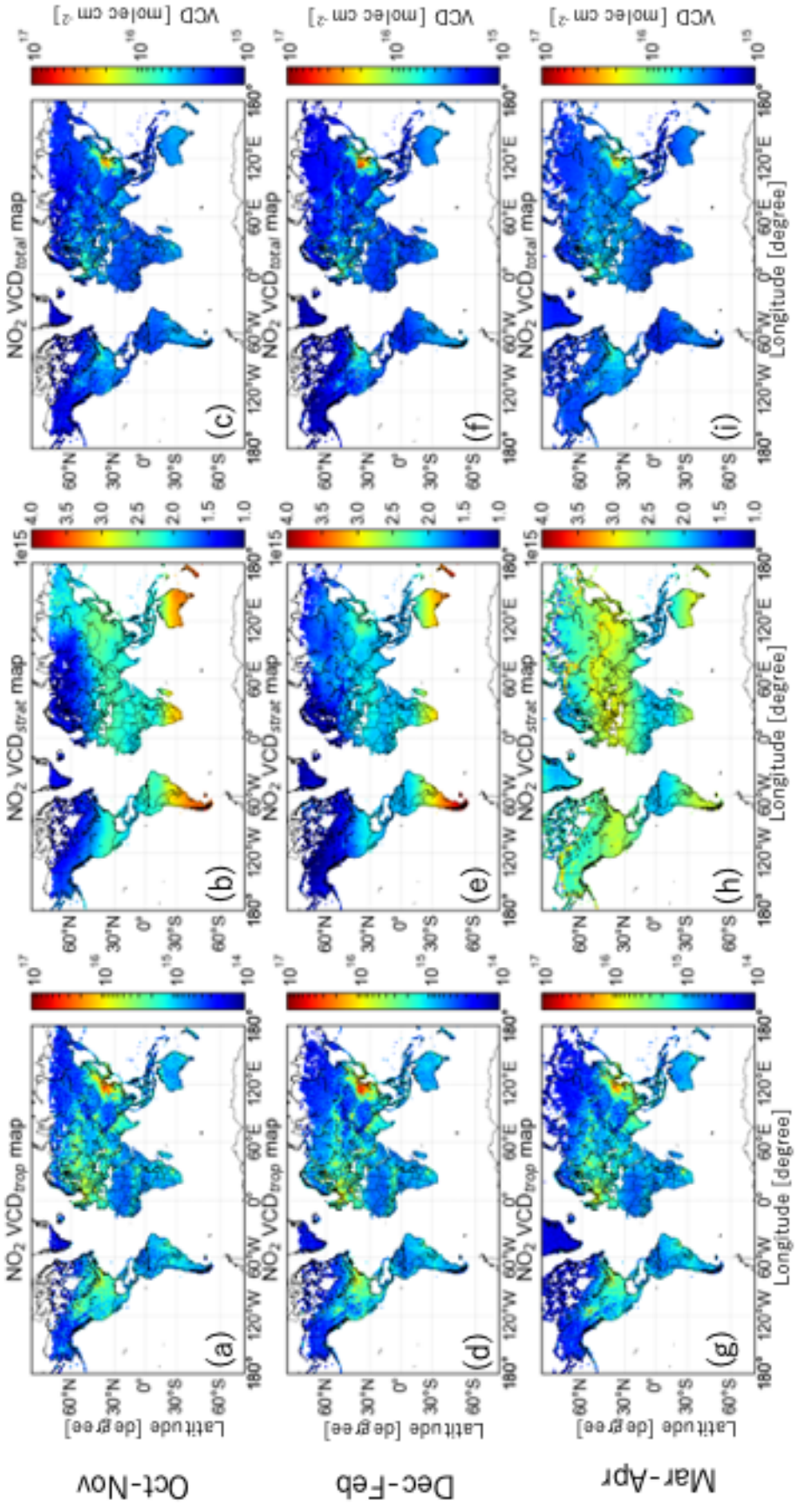

FIGURE D.1: Colormap of OMI NO_2 standard gridded products ($OMNO_2G$) for the tropospheric VCDs (left column), stratospheric VCDs (middle column), and total VCDs (right column) in the periods of October to November 2009 (upper row), December 2009 to February 2010 (middle row), and March to Aprile 2010 (lowest row), respectively. Please note that colorbar scales and ranges for each column are different. See the text for the details.

References

Akagi, S. K., Yokelson, R. J., Wiedinmyer, C., Alvarado, M. J., Reid, J. S., Karl, T., Crounse, J. D., and Wennberg, P. O.: Emission factors for open and domestic biomass burning for use in atmospheric models, Atmos. Chem. Phys., 11, 4039–4072, doi:10.5194/acp-11-4039-2011, 2011.

Akimoto, H., Kasai, Y., Kita, K., Irie, H., Sagi, K., and Hayashida, S.: Geostationary Atmospheric Observation Satellite Plan in Japan, in: AGU Fall Meet. Abstr., 2009.

Andreae, M. O.: Soot Carbon and Excess Fine Potassium: Long-Range Transport of Combustion-Derived Aerosols, Science (80-.)., 220, 1148–1151, doi:10.1126/science.220.4602.1148, 1983.

Arnold, F., Böhringer, H., and Henschen, G.: Composition measurements of stratospheric positive ions, Geophys. Res. Lett., 5, 653–656, doi:10.1029/GL005i008p00653, 1978.

Barath, F. T., Chavez, M. C., Cofield, R. E., Flower, D. A., Frerking, M. A., Gram, M. B., Harris, W. M., Holden, J. R., Jarnot, R. F., Kloezeman, W. G., Klose, G. J., Lau, G. K., Loo, M. S., Maddison, B. J., Mattauch, R. J., McKinney, R. P., Peckham, G. E., Pickett, H. M., Siebes, G., Soltis, F. S., Suttie, R. A., Tarsala, J. A., Waters, J. W., and Wilson, W. J.: The Upper Atmosphere Research Satellite microwave limb sounder instrument, J. Geophys. Res., 98, 10 751, doi:10.1029/93JD00798, 1993.

Baron, P., Mendrok, J., Kasai, Y., Ochiai, S., Seta, T., Sagi, K., Suzuki, K., Sagawa, H., and Urban, J.: AMATERASU: Model for atmospheric TeraHertz Radiation analysis and simulation, J. Natl. Inst. Inf. Commun. Technol., 55, 109–121, 2008.

Baron, P., Urban, J., Sagawa, H., Möller, J., Murtagh, D. P., Mendrok, J., Dupuy, E., Sato, T. O., Ochiai, S., Suzuki, K., Manabe, T., Nishibori, T., Kikuchi, K., Sato, R., Takayanagi, M., Murayama, Y., Shiotani, M., and Kasai, Y.: The level 2 research product algorithms for the Superconducting Submillimeter-Wave Limb-Emission Sounder (SMILES), Atmos. Meas. Tech., 4, 2105–2124, doi:10.5194/amt-4-2105-2011, 2011.

Beirle, S., Platt, U., Wenig, M., and Wagner, T.: Atmospheric Chemistry and Physics Weekly cycle of NO_2 by GOME measurements: a signature of anthropogenic sources, Atmos. Chem. Phys, 3, 2225–2232, 2003.

Beirle, S., Boersma, K. F., Platt, U., Lawrence, M. G., and Wagner, T.: Megacity emissions and lifetimes of nitrogen oxides probed from space, Science, 333, 1737–1739, doi:10.1126/science.1207824, 2011.

Bernath, P.: Atmospheric Chemistry Experiment (ACE): An Overview, pp. 147–161, Springer Netherlands, doi:10.1007/978-94-010-0832-7_9, 2001.

Boersma, K. F., Eskes, H. J., and Brinksma, E. J.: Error analysis for tropospheric NO_2 retrieval from space, J. Geophys. Res. Atmos., 109, D04 311, doi:10.1029/2003JD003962, 2004.

Boersma, K. F., Eskes, H. J., Veefkind, J. P., Brinksma, E. J., A, R. J. V. D., Sneep, M., den Oord, G. H. J. V., Levelt, P. F., Stammes, P., Gleason, J. F., and Bucsela, E. J.: Near-real time retrieval of tropospheric NO_2 from OMI, Atmos. Chem. Phys., 7, 2103–2118, 2007.

Boersma, K. F., Eskes, H. J., Dirksen, R. J., Van Der A, R. J., Veefkind, J. P., Stammes, P., Huijnen, V., Kleipool, Q. L., Sneep, M., Claas, J., Leitão, J., Richter, A., Zhou, Y., and Brunner, D.: An improved tropospheric NO_2 column retrieval algorithm for the Ozone Monitoring Instrument, Atmos. Meas. Tech., 4, 1905–1928, doi:10.5194/amt-4-1905-2011, 2011.

Bovensmann, H., Burrows, J. P., Buchwitz, M., Frerick, J., Noël, S., Rozanov, V. V., Chance, K. V., and Goede, A. P. H.: SCIAMACHY: Mission Objectives and Measurement Modes, J. Atmos. Sci., 56, 127–150, doi:10.1175/1520-0469(1999)056<0127:SMOAMM>2.0.CO;2, 1999.

Brasseur, G., Walters, S., Hitchman, M. H., Dymek, M., and Falise, E.: An interactive chemical dynamical radiative two-dimensional model of the middle atmosphere, J. Geophys. Res., 95, 5639–5655, doi:10.1029/JD095iD05p05639, 1990.

Bucsela, E., Celarier, E., Wenig, M., Gleason, J., Veefkind, J., Boersma, K., and Brinksma, E.: Algorithm for NO_2 vertical column retrieval from the ozone monitoring instrument, IEEE Trans. Geosci. Remote Sens., 44, 1245–1258, doi:10.1109/TGRS.2005.863715, 2006.

Burrows, J. P., Weber, M., Buchwitz, M., Rozanov, V., Ladstätter-Weißenmayer, A., Richter, A., DeBeek, R., Hoogen, R., Bramstedt, K., Eichmann, K.-U., Eisinger, M., Perner, D., Burrows, J. P., Weber, M., Buchwitz, M., Rozanov, V., Ladstätter-Weißenmayer, A., Richter, A., DeBeek, R., Hoogen, R., Bramstedt, K., Eichmann, K.-U., Eisinger, M., and Perner, D.: The Global Ozone Monitoring Experiment (GOME): Mission Concept and First Scientific Results, J. Atmos. Sci., 56, 151–175, doi:10.1175/1520-0469(1999)056<0151:TGOMEG>2.0.CO;2, 1999.

Callies, J., Corpaccioli, E., Eisinger, M., Hahne, A., and Lefebvre, A.: GOME-2 - Metop's second-generation sensor for operational ozone monitoring, ESA Bull. Sp. Agency, 102, 28–36, 2000.

Chance, K. and Kurucz, R. L.: An improved high-resolution solar reference spectrum for earth's atmosphere measurements in the ultraviolet, visible, and near infrared, J. Quant. Spectrosc. Radiat. Transf., 111, 1289–1295, doi:10.1016/j.jqsrt.2010.01.036, 2010.

Chapman, S.: A theory of upper atmosphere ozone, in: Mem. R. Meteorol. Soc., pp. 103–125, 3 edn., 1930.

Crutzen, P. J. and Andreae, M. O.: Biomass Burning in the Tropics: Impact on Atmospheric Chemistry and Biogeochemical Cycles, Science (80-.)., 250, 1669–1678, doi:10.1126/science.250.4988.1669, 1990.

Crutzen, P. J., Heidt, L. E., Krasnec, J. P., Pollock, W. H., and Seiler, W.: Biomass burning as a source of atmospheric gases CO, H2, N2O, NO, CH3Cl and COS, Nature, 282, 253–256, doi:10.1038/282253a0, 1979.

de Goeij, B. T. G., van Wakeren, J. M. O., Veefkind, J. P., Vlemmix, T., Ge, X., Dirks, B. P. F., Toet, P. M., van der Wal, L. F., Jansen, R., Otter, G. C. J., and Levelt, P. F.: First aircraft test results of a compact, low cost hyperspectral imager for earth observation from space, in: Int. Conf. Sp. Opt. — ICSO 2016, edited by Karafolas, N., Cugny, B., and Sodnik, Z., vol. 10562, p. 41, SPIE, doi:10.1117/12.2296068, 2017.

de Gouw, J. A.: Emission sources and ocean uptake of acetonitrile (CH 3 CN) in the atmosphere, J. Geophys. Res., 108, 4329, doi:10.1029/2002JD002897, 2003.

Dentener, F., Stevenson, D., Cofala, J., Mechler, R., Amann, M., Bergamaschi, P., Raes, F., and Derwent, R.: The impact of air pollutant and methane emission controls on tropospheric ozone and radiative forcing: CTM calculations for the period 1990–2030, Atmos. Chem. Phys., 5, 1731–1755, doi:10.5194/acp-5-1731-2005, 2005.

Dirksen, R. J., Boersma, K. F., Eskes, H. J., Ionov, D. V., Bucsela, E. J., Levelt, P. F., and Kelder, H. M.: Evaluation of stratospheric NO_2 retrieved from the Ozone Monitoring Instrument: Intercomparison, diurnal cycle, and trending, J. Geophys. Res. Atmos., 116, 1–22, doi:10.1029/2010JD014943, 2011.

Duncan, B. N., Lamsal, L. N., Thompson, A. M., Yoshida, Y., Lu, Z., Streets, D. G., Hurwitz, M. M., and Pickering, K. E.: A space-based, high-resolution view of notable changes in urban NO_x pollution around the world (2005–2014), J. Geophys. Res., 121, 976–996, doi:10.1002/2015JD024121, 2016.

Eagan, R. C., Hobbs, P. V., and Radke, L. F.: Measurements of Cloud Condensation Nuclei and Cloud Droplet Size Distributions in the Vicinity of Forest Fires, J. Appl. Meteorol., 13, 553–557, doi:10.1175/1520-0450(1974)013<0553:MOCCNA>2.0.CO;2, 1974.

Flynn, L., Hornstein, J., and Hilsenrath, E.: The ozone mapping and profiler suite (OMPS). The next generation of US ozone monitoring instruments, Geosci. Remote Sens. Symp. 2004. IGARSS '04. Proceedings. 2004 IEEE Int., 1, 152–155, doi:10.1109/IGARSS.2004.1368968, 2004.

Forster, P. M. d. F. and Shine, K. P.: Radiative forcing and temperature trends from stratospheric ozone changes, J. Geophys. Res. Atmos., 102, 10 841–10 855, doi:10.1029/96JD03510, 1997.

Fry, M. M., Schwarzkopf, M. D., Adelman, Z., and West, J. J.: Air quality and radiative forcing impacts of anthropogenic volatile organic compound emissions from ten world regions, Atmos. Chem. Phys., 14, 523–535, doi:10.5194/acp-14-523-2014, 2014.

Harrison, J. J. and Bernath, P. F.: ACE-FTS observations of acetonitrile in the lower stratosphere, Atmos. Chem. Phys., 13, 7405–7413, doi:10.5194/acp-13-7405-2013, 2013.

Hendrick, F., Clémer, K., Wang, P., De Mazière, M., Fayt, C., Gielen, C., Hermans, C., Ma, J. Z., Pinardi, G., Stavrakou, T., Vlemmix, T., and Van Roozendael, M.: Four years of ground-based MAX-DOAS observations of HONO and NO_2 in the Beijing area, Atmos. Chem. Phys., 14, 765–781, doi:10.5194/acp-14-765-2014, 2014.

Hess, M., Koepke, P., and Schult, I.: Optical properties of aerosols and clouds, Bull. Amer. Meteor. Soc., 79, 831–844, doi:10.1175/1520-0477(1998)079<0831:OPOAAC>2.0.CO;2, 1998.

Hilboll, A., Richter, A., and Burrows, J. P.: Long-term changes of tropospheric NO_2 over megacities derived from multiple satellite instruments, Atmos. Chem. Phys., 13, 4145–4169, doi:10.5194/acp-13-4145-2013, 2013.

Hong, Q., Liu, C., Chan, K. L., Hu, Q., Xie, Z., Liu, H., Si, F., and Liu, J.: Ship-based MAX-DOAS measurements of tropospheric NO_2, SO_2, and HCHO distribution along the Yangtze River, Atmos. Chem. Phys., 18, 5931–5951, doi:10.5194/acp-18-5931-2018, 2018.

Ingmann, P., Veihelmann, B., Langen, J., Lamarre, D., Stark, H., and Courrèges-Lacoste, G. B.: Requirements for the GMES Atmosphere Service and ESA's implementation concept: Sentinels-4/-5 and -5p, Remote Sens. Environ., 120, 58–69, doi:10.1016/j.rse.2012.01.023, 2012.

Irie, H., Iwabuchi, H., Kasai, Y., Kita, K., and Akimoto, H.: A simulation for UV-VIS observations of tropospheric composition from a GEO satellite over Asia, in: AGU Fall Meet. Abstr., 2009.

Irie, H., Iwabuchi, H., Noguchi, K., Kasai, Y., Kita, K., and Akimoto, H.: Quantifying the relationship between the measurement precision and specifications of a UV/visible sensor on a geostationary satellite, Adv. Sp. Res., 49, 1743–1749, doi:10.1016/j.asr.2012.03.012, URL http://dx.doi.org/10.1016/j.asr.2012.03.012, 2012.

Itahashi, S., Uno, I., Irie, H., Kurokawa, J. I., and Ohara, T.: Regional modeling of tropospheric NO_2 vertical column density over East Asia during the period 2000–2010: Comparison with multisatellite observations, Atmos. Chem. Phys., 14, 3623–3635, doi:10.5194/acp-14-3623-2014, 2014.

Kanaya, Y., Irie, H., Takashima, H., Iwabuchi, H., Akimoto, H., Sudo, K., Gu, M., Chong, J., Kim, Y. J., Lee, H., Li, A., Si, F., Xu, J., Xie, P.-H., Liu, W.-Q., Dzhola, A., Postylyakov, O., Ivanov, V., Grechko, E., Terpugova, S., and Panchenko, M.: Long-term MAX-DOAS network observations of NO_2 in Russia and Asia (MADRAS) during the period 2007–2012: instrumentation, elucidation of climatology, and comparisons with OMI satellite observations and global model simulations, Atmos. Chem. Phys, 14, 7909–7927, doi:10.5194/acp-14-7909-2014, 2014.

Kasai, Y., Kita, K., Kanaya, Y., Team, A. M., and Others: The Japanese Air Pollusion Observation Missions, GMAP-Asia and APOLLO., in: AGU Fall Meet. Abstr., 2011.

Kawasaki, H., Konoue, K., Hoshino, H., Kaneko, Y., and Sasaki, M.: Interim Report of Super Low Altitude Satellite Operation, in: IGARSS 2018 - 2018 IEEE Int. Geosci. Remote Sens. Symp., pp. 4066–4069, IEEE, doi:10.1109/IGARSS.2018.8517529, 2018.

Kikuchi, K. I., Nishibori, T., Ochiai, S., Ozeki, H., Irimajiri, Y., Kasai, Y., Koike, M., Manabe, T., Mizukoshi, K., Murayama, Y., Nagahama, T., Sano, T., Sato, R., Seta, M., Takahashi, C., Takayanagi, M., Masuko, H., Inatani, J., Suzuki, M., and Shiotani, M.: Overview and early results of the Superconducting Submillimeter-Wave Limb-Emission Sounder (SMILES), J. Geophys. Res. Atmos., 115, 1–12, doi:10.1029/2010JD014379, 2010.

Kim, J.: GEMS (Geostationary Environment Monitoring Spectrometer) onboard the GeoKOMPSAT to Monitor Air Quality in high Temporal and Spatial Resolution over Asia-Pacific Region, EGU Gen. Assem. 2012, held 22-27 April. 2012 Vienna, Austria., p.4051, 14, 4051, 2012.

Kim, S.-W., Heckel, A., McKeen, S. A., Frost, G. J., Hsie, E.-Y., Trainer, M. K., Richter, A., Burrows, J. P., Peckham, S. E., and Grell, G. A.: Satellite-observed U.S. power plant NO_x emission reductions and their impact on air quality, Geophys. Res. Lett., 33, L22 812, doi:10.1029/2006GL027749, 2006.

Kleipool, Q. L., Dobber, M. R., de Haan, J. F., and Levelt, P. F.: Earth surface reflectance climatology from 3 years of OMI data, J. Geophys. Res. Atmos., 113, D18 308, doi:10.1029/2008JD010290, URL http://doi.wiley.com/10.1029/2008JD010290, 2008.

Knop, G. and Arnold, F.: Stratospheric trace gas detection using a new balloon-borne ACIMS method: Acetonitrile, acetone, and nitric acid, Geophys. Res. Lett., 14, 1262–1265, doi:10.1029/GL014i012p01262, 1987.

Krotkov, N. A.: OMI/Aura NO_2 Total and Tropospheric Column Daily L2 Global Gridded 0.25 degree x 0.25 degree V3, Tech. rep., doi:10.5067/Aura/OMI/DATA2018, 2012, Accessed: 8 April 2019.

Kuze, A., Imai, T., and Suto, H.: 1-km resolution mapping from space with a sub-nanometer spectral resolution imaging spectrometer, in: Hyperspectral Imaging Sound. Environ. HISE 2015, p. HM4B.2, OSA, Washington, D.C., doi:10.1364/HISE.2015.HM4B.2, 2015.

Kuze, A., FOR, H. S. T. O. T. J. S., and 2018, U.: Imaging Spectrometer with an Agile Pointing System to Quantify Global and Regional Greenhouse Gas Fluxes and Monitor Localized Emission Sources, jstage.jst.go.jp, 16, 147–151, doi:10.2322/tastj.16.147, 2018.

Lamsal, L. N., Martin, R. V., Padmanabhan, A., van Donkelaar, A., Zhang, Q., Sioris, C. E., Chance, K., Kurosu, T. P., and Newchurch, M. J.: Application of satellite observations for timely updates to global anthropogenic NO_x emission inventories, Geophys. Res. Lett., 38, L05 810, doi:10.1029/2010GL046476, 2011.

Levelt, P. F., van den Oord, G. H. J., Dobber, M. R., Malkki, A., Visser, H., de Vries, J., Stammes, P., Lundell, J. O. V., and Saari, H.: The ozone monitoring instrument, IEEE Trans. Geosci. Remote Sens., 44, 1093–1101, doi:10.1109/TGRS.2006.872333, 2006.

Li, Q., Jacob, D. J., Bey, I., Yantosca, R. M., Zhao, Y., Kondo, Y., and Notholt, J.: Atmospheric hydrogen cyanide (HCN): Biomass burning source, ocean sink?, Geophys. Res. Lett., 27, 357–360, doi:10.1029/1999GL010935, 2000.

Li, Q., Jacob, D. J., Yantosca, R. M., Heald, C. L., Singh, H. B., Koike, M., Zhao, Y., Sachse, G. W., and Streets, D. G.: A global three-dimensional model analysis of the atmospheric budgets of HCN and CH 3 CN: Constraints from aircraft and ground measurements, J. Geophys. Res., 108, 8827, doi:10.1029/2002JD003075, 2003.

Li, Q., Palmer, P. I., Pumphrey, H. C., Bernath, P., and Mahieu, E.: What drives the observed variability of HCN in the troposphere and lower stratosphere?, Atmos. Chem. Phys., 9, 8531–8543, doi:10.5194/acp-9-8531-2009, 2009.

Lin, J. T., Martin, R. V., Boersma, K. F., Sneep, M., Stammes, P., Spurr, R., Wang, P., Van Roozendael, M., Clémer, K., and Irie, H.: Retrieving tropospheric nitrogen dioxide from the Ozone Monitoring Instrument: Effects of aerosols, surface reflectance anisotropy, and vertical profile of nitrogen dioxide, Atmos. Chem. Phys., 14, 1441–1461, doi:10.5194/acp-14-1441-2014, 2014.

Livesey, N., Van Snyder, W., Read, W., and Wagner, P.: Retrieval algorithms for the EOS Microwave limb sounder (MLS), IEEE Trans. Geosci. Remote Sens., 44, 1144–1155, doi:10.1109/TGRS.2006.872327, 2006.

Livesey, N. J., Waters, J. W., Khosravi, R., Brasseur, G. P., Tyndall, G. S., and Read, W. G.: Stratospheric CH 3 CN from the UARS Microwave Limb Sounder, Geophys. Res. Lett., 28, 779–782, doi:10.1029/2000GL012144, 2001.

Livesey, N. J., Fromm, M. D., Waters, J. W., Manney, G. L., Santee, M. L., and Read, W. G.: Enhancements in lower stratospheric CH 3 CN observed by the Upper Atmosphere Research Satellite Microwave Limb Sounder following boreal forest fires, J. Geophys. Res. Atmos., 109, n/a–n/a, doi:10.1029/2003JD004055, 2004.

Ma, J. Z., Beirle, S., Jin, J. L., Shaiganfar, R., Yan, P., and Wagner, T.: Tropospheric NO_2 vertical column densities over Beijing: Results of the first three years of ground-based MAX-DOAS measurements (2008-2011) and satellite validation, Atmos. Chem. Phys., 13, 1547–1567, doi:10.5194/acp-13-1547-2013, 2013.

Martin, R. V., Chance, K., Jacob, D. J., Kurosu, T. P., Spurr, R. J., Bucsela, E., Gleason, J. F., Palmer, P. I., Bey, I., Fiore, A. M., Li, Q., Yantosca, R. M., and Koelemeijer, R. B.: An improved retrieval of tropospheric nitrogen dioxide from GOME, J. Geophys. Res. D Atmos., 107, doi:10.1029/2001JD001027, 2002.

Meier, A. C., Schönhardt, A., Bösch, T., Richter, A., Seyler, A., Ruhtz, T., Constantin, D. E., Shaiganfar, R., Wagner, T., Merlaud, A., Roozendael, M. V., Belegante, L., Nicolae, D., Georgescu, L., and Burrows, J. P.: High-resolution airborne imaging DOAS measurements of NO_2 above Bucharest during AROMAT, Atmos. Meas. Tech., 10, 1831–1857, doi:10.5194/amt-10-1831-2017, 2017.

Merlaud, A., Tack, F., Constantin, D.-E., Georgescu, L., Maes, J., Fayt, C., Mingireanu, F., Schuettemeyer, D., Meier, A. C., Schönardt, A., Ruhtz, T., Bellegante, L., Nicolae, D., Den Hoed, M., Allaart, M., and Van Roozendael, M.: The Small Whiskbroom Imager for atmospheric compositioN monitorinG (SWING) and its operations from an unmanned aerial vehicle (UAV) during the AROMAT campaign, Atmos. Meas. Tech., 11, 551–567, doi:10.5194/amt-11-551-2018, URL https://www.atmos-meas-tech.net/11/551/2018/, 2018.

Nagano, H., Kajiwara, K., Osuga, H., Ozaki, T., and Nakagawa, T.: Research and Development of a New Power Processing Control Unit of Ion Engine System for the Super Low Altitude Test Satellite, Trans. Japan Soc. Aeronaut. Sp. Sci. Aerosp. Technol. Japan, 8, Tb_17–Tb_22, doi:10.2322/tastj.8.Tb_17, 2010.

Noguchi, K., Richter, A., Bovensmann, H., Hilboll, A., Burrows, J. P., Irie, H., Hayashida, S., and Morino, Y.: A feasibility study for the detection of the diurnal variation of tropospheric NO_2 over Tokyo from a geostationary orbit, Adv. Sp. Res., 48, 1551–1564, doi:10.1016/j.asr.2011.06.029, 2011.

Noguchi, K., Richter, A., Rozanov, V., Rozanov, A., Burrows, J. P., Irie, H., and Kita, K.: Effect of surface BRDF of various land cover types on geostationary observations of tropospheric NO_2, Atmos. Meas. Tech., 7, 3497–3508, doi:10.5194/amt-7-3497-2014, 2014.

Ochiai, S., Kikuchi, K., Nishibori, T., Manabe, T., Ozeki, H., Mizukoshi, K., Ohtsubo, F., Tsubosaka, K., Irimajiri, Y., Sato, R., and Shiotani, M.: Performance of JEM / SMILES in orbit, in: Twenty-First Int. Symp. Sp. Terahertz Technol., pp. 179–184, 2011.

Pan, L. L., Bowman, K. P., Atlas, E. L., Wofsy, S. C., Zhang, F., Bresch, J. F., Ridley, B. A., Pittman, J. V., Homeyer, C. R., Romashkin, P., and Cooper, W. A.: The Stratosphere–Troposphere Analyses of Regional Transport 2008 Experiment, Bull. Am. Meteorol. Soc., 91, 327–342, doi:10.1175/2009BAMS2865.1, 2010.

Phillips, G. J., Pouvesle, N., Thieser, J., Schuster, G., Axinte, R., Fischer, H., Williams, J., Lelieveld, J., and Crowley, J. N.: Peroxyacetyl nitrate (PAN) and peroxyacetic acid (PAA) measurements by iodide chemical ionisation mass spectrometry: first analysis of results in the boreal forest and implications for the measurement of PAN fluxes, Atmos. Chem. Phys., 13, 1129–1139, doi:10.5194/acp-13-1129-2013, 2013.

Platt, U.: Differential optical absorption spectroscopy (DOAS), in: Air monitoring by spectroscopic techniques, edited by: Sigrist, M.W., Chem. Anal. Ser., 127, 27–84, 1994.

Pumphrey, H. C., Santee, M. L., Livesey, N. J., Schwartz, M. J., and Read, W. G.: Microwave Limb Sounder observations of biomass-burning products from the Australian bush fires of February 2009, Atmos. Chem. Phys., 11, 6285–6296, doi:10.5194/acp-11-6285-2011, 2011.

Randerson, J. T., van der Werf, G. R., Giglio, L., Collatz, G. J., and Kasibhatla, P. S.: Global Fire Emissions Database, Version 4.1 (GFEDv4), doi:10.3334/ornldaac/1293, 2017.

Richter, A. and Burrows, J.: Tropospheric NO_2 from GOME measurements, Adv. Sp. Res., 29, 1673–1683, doi:10.1016/S0273-1177(02)00100-X, 2002.

Richter, A., Burrows, J. P., Nüß, H., Granier, C., and Niemeier, U.: Increase in tropospheric nitrogen dioxide over China observed from space, Nature, 437, 129–132, doi:10.1038/nature04092, 2005.

Richter, A., Begoin, M., Hilboll, A., and Burrows, J. P.: An improved NO_2 retrieval for the GOME-2 satellite instrument, Atmos. Meas. Tech., 4, 1147–1159, doi:10.5194/amt-4-1147-2011, 2011.

Rienecker, M., Suarez, M., Todling, R., Bacmeister, J., Takacs, L., Liu, H.-C., Gu, W., Sienkiewicz, M., Koster, R., Gelaro, R., Stajner, I., and Nielsen, J.: The GEOS-5 Data Assimilation System—Documentation of Versions 5.0.1, 5.1.0, and 5.2.0, Tech. Rep. December, 2008.

Rodgers, C. D.: Inverse Methods for Atmospheric Sounding: Theory and Practice, World Scientific, London, vol. 2 edn., 2000.

Rothman, L. S., Gordon, I. E., Barbe, A., Benner, D. C., Bernath, P. F., Birk, M., Boudon, V., Brown, L. R., Campargue, A., Champion, J. P., Chance, K., Coudert, L. H., Dana, V., Devi, V. M., Fally, S., Flaud, J. M., Gamache, R. R., Goldman, A., Jacquemart, D., Kleiner, I., Lacome, N., Lafferty, W. J., Mandin, J. Y., Massie, S. T., Mikhailenko, S. N., Miller, C. E., Moazzen-Ahmadi, N., Naumenko, O. V., Nikitin, A. V., Orphal, J., Perevalov, V. I., Perrin, A., Predoi-Cross, A., Rinsland, C. P., Rotger, M., Šimečková, M., Smith, M. A., Sung, K., Tashkun, S. A., Tennyson, J., Toth, R. A., Vandaele, A. C., and Vander Auwera, J.: The HITRAN 2008 molecular spectroscopic database, J. Quant. Spectrosc. Radiat. Transf., 110, 533–572, doi:10.1016/j.jqsrt.2009.02.013, 2009.

Rozanov, A., Rozanov, V., Buchwitz, M., Kokhanovsky, A., and Burrows, J. P.: SCIATRAN 2.0 - A new radiative transfer model for geophysical applications in the 175-2400 nm spectral region, Adv. Sp. Res., 36, 1015–1019, doi:10.1016/j.asr.2005.03.012, 2005.

Schneider, J., Bürger, V., and Arnold, F.: Methyl cyanide and hydrogen cyanide measurements in the lower stratosphere: Implications for methyl cyanide sources and sinks, J. Geophys. Res. Atmos., 102, 25 501–25 506, doi:10.1029/97JD02364, 1997.

Schönhardt, A., Altube, P., Gerilowski, K., Krautwurst, S., Hartmann, J., Meier, A. C., Richter, A., and Burrows, J. P.: A wide field-of-view imaging DOAS instrument for two-dimensional trace gas mapping from aircraft, Atmos. Meas. Tech., 8, 5113–5131, doi:10.5194/amt-8-5113-2015, 2015.

Seiler, W. and Crutzen, P. J.: Estimates of gross and net fluxes of carbon between the biosphere and the atmosphere from biomass burning, Clim. Change, 2, 207–247, doi:10.1007/BF00137988, 1980.

Serdyuchenko, A., Gorshelev, V., Weber, M., Chehade, W., and Burrows, J. P.: High spectral resolution ozone absorption cross-sections – Part 2: Temperature dependence, Atmos. Meas. Tech, 7, 625–636, doi:10.5194/amt-7-625-2014, URL www.atmos-meas-tech.net/7/625/2014/, 2014.

Seyler, A., Meier, A. C., Wittrock, F., Kattner, L., Mathieu-Üffing, B., Peters, E., Richter, A., Ruhtz, T., Schönhardt, A., Schmolke, S., and Burrows, J. P.: Studies of the horizontal inhomogeneities in NO2 concentrations above a shipping lane using ground-based MAX-DOAS and airborne imaging DOAS measurements, Atmos. Meas. Tech. Discuss., pp. 1–26, doi:10.5194/amt-2018-348, URL https://www.atmos-meas-tech-discuss.net/amt-2018-348/, 2018.

Shepherd, T. G.: Transport in the Middle Atmosphere, J. Meteorol. Soc. Japan. Ser. II, 85B, 165–191, doi:10.2151/jmsj.85B.165, 2007.

Singh, H. B., Salas, L., Herlth, D., Kolyer, R., Czech, E., Viezee, W., Li, Q., Jacob, D. J., Blake, D., Sachse, G., Harward, C. N., Fuelberg, H., Kiley, C. M., Zhao, Y., and Kondo, Y.: In situ measurements of HCN and CH 3 CN over the Pacific Ocean: Sources, sinks, and budgets, J. Geophys. Res., 108, 8795, doi:10.1029/2002JD003006, 2003.

Stavrakou, T., Müller, J.-F., Boersma, K. F., De Smedt, I., and van der A, R. J.: Assessing the distribution and growth rates of NO_x emission sources by inverting a 10-year record of NO_2 satellite columns, Geophys. Res. Lett., 35, L10 801, doi:10.1029/2008GL033521, 2008.

Stohl, A., Bonasoni, P., Cristofanelli, P., Collins, W., Feichter, J., Frank, A., Forster, C., Gerasopoulos, E., Gäggeler, H., James, P., Kentarchos, T., Kromp-Kolb, H., Krüger, B., Land, C., Meloen, J., Papayannis, A., Priller, A., Seibert, P., Sprenger, M., Roelofs, G. J., Scheel, H. E., Schnabel, C., Siegmund, P., Tobler, L., Trickl, T., Wernli, H., Wirth, V., Zanis, P., and Zerefos, C.: Stratosphere-troposphere exchange: A review, and what we have learned from STACCATO, J. Geophys. Res., 108, doi:10.1029/2002jd002490, 2003.

Sudo, K., Takahashi, M., Kurokawa, J. I., and Akimoto, H.: CHASER: A global chemical model of the troposphere 1. Model description, J. Geophys. Res. Atmos., 107, doi:10.1029/2001JD001113, 2002.

Suzuki, M., Mitsuda, C., Kikuchi, K., Nishibori, T., Ochiai, S., Ozeki, H., Sano, T., Mizobuchi, S., Takahashi, C., Manago, N., Imai, K., Naito, Y., Hayashi, H., Nishimoto, E., and Shiotani, M.: Overview of the Superconducting Submillimeter-Wave Limb-Emission Sounder (SMILES) and Sensitivity to Chlorine Monoxide, ClO, The transactions of the Institute of Electrical Engineers of Japan. A, A publication of Fundamentals and Materials Society, 132, 609–615, doi:10.1541/ieejfms.132.609, 2012.

Tack, F., Merlaud, A., Meier, A. C., Vlemmix, T., Ruhtz, T., Iordache, M.-D., Ge, X., van der Wal, L., Schuettemeyer, D., Ardelean, M., Calcan, A., Schönhardt, A., Meuleman, K., Richter, A., and Van Roozendael, M.: Intercomparison of four airborne imaging DOAS systems for tropospheric NO_2; The AROMAPEX campaign, Atmos. Meas. Tech. Discuss., pp. 1–48, doi:10.5194/amt-2017-478, 2018.

Thalman, R. and Volkamer, R.: Temperature dependent absorption cross-sections of O2–O2 collision pairs between 340 and 630 nm and at atmospherically relevant pressure, Phys. Chem. Chem. Phys., 15, 15 371, doi:10.1039/c3cp50968k, URL https://www.colorado.edu/chemistry/volkamer/publications/articles/T-and-V-2013-O4-PCCPaccepted.pdfhttp://xlink.rsc.org/?DOI=c3cp50968k, 2013.

Unger, N., Shindell, D. T., Koch, D. M., and Streets, D. G.: Air pollution radiative forcing from specific emissions sectors at 2030, J. Geophys. Res., 113, D02 306, doi:10.1029/2007JD008683, 2008.

Urban, J., Baron, P., Lautié, N., Schneider, N., Dassas, K., Ricaud, P., and De La Noë, J.: Moliere (v5): A versatile forward- and inversion model for the millimeter and sub-millimeter wavelength range, J. Quant. Spectrosc. Radiat. Transf., 83, 529–554, doi:10.1016/S0022-4073(03)00104-3, 2004.

Valks, P., Pinardi, G., Richter, A., Lambert, J. C., Hao, N., Loyola, D., Van Roozendael, M., and Emmadi, S.: Operational total and tropospheric NO_2 column retrieval for GOME-2, Atmos. Meas. Tech., 4, 1491–1514, doi:10.5194/amt-4-1491-2011, 2011.

van der A, R. J., Peters, D. H., Eskes, H., Boersma, K. F., Van Roozendael, M., De Smedt, I., and Kelder, H. M.: Detection of the trend and seasonal variation in tropospheric NO_2 over China, J. Geophys. Res. Atmos., 111, 1–10, doi:10.1029/2005JD006594, 2006.

van der A., R. J., Eskes, H. J., Boersma, K. F., van Noije, T. P., Van Roozendael, M., De Smedt, I., Peters, D. H., and Meijer, E. W.: Trends, seasonal variability and dominant NO_x source derived from a ten year record of NO_2 measured from space, J. Geophys. Res. Atmos., 113, D04 302, doi:10.1029/2007JD009021, 2008.

van Geffen, J. H. G. M., Eskes, H. J., Boersma, K. F., Maasakkers, J. D., and Veefkind, J. P.: TROPOMI ATBD of the total and tropospheric NO_2 data products, Tech. rep., URL http://www.tropomi.eu/documents/atbd, (accessed 30 October 2018).

Vandaele, A. C., Hermans, C., Fally, S., Carleer, M., Colin, R., Merienne, M., Jenouvrier, A., and Coquart, B.: High-resolution Fourier transform measurement of the NO 2 visible and near-infrared absorption cross sections: Temperature and pressure effects, J. Geophys. Res., 107, 4348, doi:10.1029/2001JD000971, URL https://agupubs.onlinelibrary.wiley.com/doi/full/10.1029/2001JD000971http://doi.wiley.com/10.1029/2001JD000971, 2002.

Velders, G. J. M., Granier, C., Portmann, R. W., Pfeilsticker, K., Wenig, M., Wagner, T., Platt, U., Richter, A., and Burrows, J. P.: Global tropospheric NO_2 column distributions: Comparing three-dimensional model calculations with GOME measurements, J. Geophys. Res. Atmos., 106, 12 643–12 660, doi:10.1029/2000JD900762, 2001.

Vountas, M., Rozanov, V. V., and Burrows, J. P.: Ring effect: Impact of rotational Raman scattering on radiative transfer in earth's atmosphere, J. Quant. Spectrosc. Radiat. Transf., 60, 943–961, doi:10.1016/S0022-4073(97)00186-6, 1998.

Wang, Y., Lampel, J., Xie, P., Beirle, S., Li, A., Wu, D., and Wagner, T.: Ground-based MAX-DOAS observations of tropospheric aerosols, NO_2 , SO_2 and HCHO in Wuxi, China, from 2011 to 2014, Atmos. Chem. Phys, 17, 2189–2215, doi:10.5194/acp-17-2189-2017, 2017.

Wang, Y. X., McElroy, M. B., Jacob, D. J., and Yantosca, R. M.: A nested grid formulation for chemical transport over Asia: Applications to CO, J. Geophys. Res. D Atmos., 109, 1–20, doi:10.1029/2004JD005237, 2004.

Waters, J. W., Froidevaux, L., Harwood, R. S., Jarnot, R. F., Pickett, H. M., Read, W. G., Siegel, P. H., Cofield, R. E., Filipiak, M. J., Flower, D. A., Holden, J. R., Lau, G. K., Livesey, N. J., Manney, G. L., Pumphrey, H. C., Santee, M. L., Wu, D. L., Cuddy, D. T., Lay, R. R., Loo, M. S., Perun, V. S., Schwartz, M. J., Stek, P. C., Thurstans, R. P., Boyles, M. A., Chandra, K. M., Chavez, M. C., Chen, G. S., Chudasama, B. V., Dodge, R., Fuller, R. A., Girard, M. A., Jiang, J. H., Jiang, Y., Knosp, B. W., Labelle, R. C., Lam, J. C., Lee, K. A., Miller, D., Oswald, J. E., Patel, N. C., Pukala, D. M., Quintero, O., Scaff, D. M., Van Snyder, W., Tope, M. C., Wagner, P. A., and Walch, M. J.: The Earth Observing System Microwave Limb Sounder (EOS MLS) on the aura satellite, IEEE Trans. Geosci. Remote Sens., 44, 1075–1092, doi:10.1109/TGRS.2006.873771, 2006.

World Health Organization: Ambient (outdoor) air quality and health, URL http://www.who.int/mediacentre/factsheets/fs313/en/, 2016.

Zhao, Y., Nielsen, C. P., Lei, Y., McElroy, M. B., and Hao, J.: Quantifying the uncertainties of a bottom-up emission inventory of anthropogenic atmospheric pollutants in China, Atmos. Chem. Phys., 11, 2295–2308, doi:10.5194/acp-11-2295-2011, 2011.

Zoogman, P., Liu, X., Suleiman, R. M., Pennington, W. F., Flittner, D. E., Al-Saadi, J. A., Hilton, B. B., Nicks, D. K., Newchurch, M. J., Carr, J. L., Janz, S. J., Andraschko, M. R., Arola, A., Baker, B. D., Canova, B. P., Chan Miller, C., Cohen, R. C., Davis, J. E., Dussault, M. E., Edwards, D. P., Fishman, J., Ghulam, A., González Abad, G., Grutter, M., Herman, J. R., Houck, J., Jacob, D. J., Joiner, J., Kerridge, B. J., Kim, J., Krotkov, N. A., Lamsal, L., Li, C., Lindfors, A., Martin, R. V., McElroy, C. T., McLinden, C., Natraj, V., Neil, D. O., Nowlan, C. R., O'Sullivan, E. J., Palmer, P. I., Pierce, R. B., Pippin, M. R., Saiz-Lopez, A., Spurr, R. J., Szykman, J. J., Torres, O., Veefkind, J. P., Veihelmann, B., Wang, H., Wang, J., and Chance, K.: Tropospheric emissions: Monitoring of pollution (TEMPO), J. Quant. Spectrosc. Radiat. Transf., 186, 17–39, doi:10.1016/j.jqsrt.2016.05.008, 2017.